A STUDY OF PROMPT NEUTRON EMISSION IN THERMAL-NEUTRON-INDUCED FISSION OF ^{235}U

by

CHRISTOPHER BARRY FRANKLYN

Submitted in partial fulfilment of the requirements for the degree of

Doctor

in the Faculty of Science,

University of Pretoria,

PRETORIA

August 1986

SAMEVATTING

'n Oorspronklike eksperiment is uitgevoer om hoekkorrelasies tussen klowings-neutrone en die ligte klowingsfragment as 'n funksie van massaverdeling en neutronenergie in die klowing van ^{235}U met termiese neutrone te meet. 'n Monte Carlo-model met 'n realistiese beskrywing van die verval van die klowingsfragmente is ontwikkel om die waargenome hoekkorrelasies te simuleer. Met dié model kon verskillende moontlikhede gesimuleer word wat geklassifiseer kan word as neutronemissie voor, tydens en na versnelling van die fragmente en wat respektiewelik as skeidings-, versnellings- en prontneutrone bekend staan. Daar kon aangetoon word dat verskillende vorms van neutronemissie wat in kombinasie identiese gesimuleerde hoekverdelings tot gevolg het, verskille vertoon as die data as 'n funksie van fragmentmassa of neutronenergie ondersoek word. Dit bevestig die sinvolheid van die eksperiment om verskillende vorms van neutronemissie tydens klowing deur middel van simulasie te identifiseer. Die hoofgevolgtrekking van die ondersoek is dat die aanname van neutronemissie alleenlik vanaf volversnelde fragmente - hetsy isotroop of anisotroop in die massamiddelpuntsisteem - nie voldoende vir die beskrywing van die gemete hoekkorrelasies is nie. 'n Beter resultaat is verkry met gedeeltelike neutronemissie voor en tydens versnelling van die fragmente. Die simulasie met die beste algehele beskrywing van die eksperiment neem aan dat 20% van die neutrone isotroop in die laboratoriumsisteem as skeidingsneutrone met 'n Maxwell energieverdeling, temperatuur 1 MeV, uitgestraal word. Die orige neutrone word isotroop met betrekking tot die massamiddelpunte van die fragmente uitgestraal, behalwe die n-de ($n > 1$) neutrone vanaf die ligte fragment, wat anisotroop volgens $(1+b\ \cos^2\theta)$ uitgestraal word, waar $\theta=0^o$ langs die klowingsas lê. Die parameter b lê tussen 0.02 en 0.1 en verteenwoordig die invloed van hoekmomentum op die vervalproses van die klowingsfragmente.

ABSTRACT

An original experiment was performed to measure the angular correlation of fission neutrons from thermal-neutron-induced fission of ^{235}U, with respect to the light fission fragment direction, as a function of fragment mass division and neutron energy. A Monte Carlo model, with a realistic description of the fission fragment de-excitation process, was developed to simulate the observed neutron-fragment angular correlation data. The model was capable of investigating various possible forms of neutron emission which were classified into emission before, during and after full fragment acceleration, and correspondingly named scission acceleration and prompt neutron emission. Simulated neutron-fragment angular correlations displaying similar distributions with respect to the light fragment direction for different forms of neutron emission are shown to exhibit differing distributions when examined as a function of fragment mass division or neutron energy, thus illustrating the sensitivity of the experiment to the forms of neutron emission occurring in fission. A primary conclusion of the investigation was that neutron emission solely from fully accelerated fragments, whether isotropically or anisotropically emitted in the fragment centre of mass system, was unable to adequately describe the observed neutron-fragment angular correlations. Simulation of the fission process with some neutron emission before or during fragment acceleration exhibited a closer correspondence with observed phenomena. Within the scope of this work the form of neutron emission that produced the closest overall correspondence with experimental data was a simulation in which 20% of the emitted neutrons were isotropically emitted scission neutrons with a Maxwellian energy distribution of temperature 1.0 MeV. The remaining neutrons were emitted from fully accelerated fragments, being isotropic in the fragment centre of mass frame, except for the n-th($n > 1$) neutrons from the light fragment, which were emitted anisotropically. The form of the anisotropy is described by $(1+b\cos^2\theta)$, where $\theta = 0$ lies along the fission axis, and b has any value between 0.02 and 0.1 and represents the influence of fission fragment angular momentum on the fragment de-excitation process.

ACKNOWLEDGEMENTS

I would like to express my appreciation and thanks to:

Prof. E Friedland for supporting me in pursuing this work.

Dr C Hofmeyr for guidance and advice unstintingly provided over many years of working together.

Dr D W Mingay for encouraging and motivating me to undertake this work.

Emmie Henning for typing this manuscript and seeing it through its many drafts.

The AEC Van de Graaff Group for their help in making the PIXE measurements.

The Atomic Energy Corporation for allowing me the opportunity to undertake this work and providing the facilities used.

The many participants of the International Conference on Nuclear Data for Basic and Applied Science held in May 1985 in Santa Fe, USA, for many useful discussions and suggestions, in particular to John Boldeman, Friedrich Gönnenwein, Normal Holden, Carl Budtz-Jorgensen, Modesto Montoya and J Rayford Nix.

I am also especially grateful to my wife Trudi, whose continuous encouragement and support enabled me to persevere and complete this work, and to my children Paul and Claire who patiently waited for my few free moments during this work.

C O N T E N T S

C O N T E N T S

C O N T E N T S

1 INTRODUCTION AND REVIEW

1.1 Field of Study

An outline of the fission process is presented with emphasis on the properties of prompt neutron emission. It is shown that, apart from experimental ambiguities, considerable obstacles remain in developing a theoretical model of the fission process that adequately describes the characteristics of neutron emission observed experimentally, as typified by the debate around the characteristics of scission neutrons, and their effect on the angular distribution of neutrons emitted in fission. Knowledge of the neutron-fragment angular correlation as a function of fragment mass division and neutron energy are important to restrict further the uncertainties in the model parameters used in simulating the fission process.

1.2 Development of fission models

In 1938 nuclear fission had been experimentally and theoretically appreciated, and since then many theories have been developed in an attempt to explain the whole concept of fission and post-fission phenomena but no theory exists, as yet, which is capable of explaining all of the observed phenomena. These models do, however, go a long way toward helping to understand many of the processes seen in fission.

The first qualitative theoretical discussion of the fission process in terms of competition between the disrupting effect of Coulombic repulsion and the stabilizing influence of surface tension, which was analogous to the description of a liquid drop, was proposed by Meitner and Frisch (Me39) in 1939. This simple liquid drop model (LDM) could not, however, explain the observed mass asymmetry seen in fission, and it was not until the shell model was formulated in 1949 by Haxel et al (Ha 49) and Mayer (Ma49), leading to the development of more complex models of deformed nuclei (collective and unified models), that the fission models began to approximate some of the observed phenomena.

Further progress came in 1966 when Strutinsky (St66, St67, St68), and Myers and Swiatecki (My66) related the small level density of closed shell nuclei to increased binding energy leading to the shell correction term of the LDM. Finally a Hartree-Fock treatment of nuclear deformations gave a microscopic basis to the Strutinsky procedure, from which the observed mass asymmetry in fission could, on the basis of a deformed shell structure, be qualitatively understood.

Present experimental and theoretical studies of the fission process investigate not only the break-up of a heavy nucleus (fission) (Ni84), but also the quasi-fission process evolving from fusion and quasi-fusion reactions in heavy-ion collisions at high energies (Hi86). The study of quasi-fission reactions is a reflection of the ongoing attempts to understand the dynamic processes involved at the point of scission of a compound nucleus.

There are two basic modes of fission, namely induced and spontaneous fission. The process of spontaneous fission can be described as a form of tunneling through the nuclear potential energy barrier. In the case of induced fission a particle is captured or a photon absorbed by the nucleus, providing it with an excitation energy consisting of the particle binding energy plus its kinetic energy in the centre-of-mass system. The excited nucleus subsequently relaxes into a collectively excited compound state oscillating between states of high deformation energy and high internal temperature. Among the many deformation states are a few configurations which allow the nucleus to pass over a potential energy barrier (saddle point) and fission. The actual shape of the potential energy as a function of nuclear deformation is dependent on the model used, as illustrated in Figure 1.1. For the simple LDM a single-hump barrier is formed (dasned line in the figure). With the addition of shell energy corrections to the LDM this single hump barrier splits into two humps, which provides a relatively good agreement between experimental and theoretical results. The presence of a valley provides an explanation of isomeric

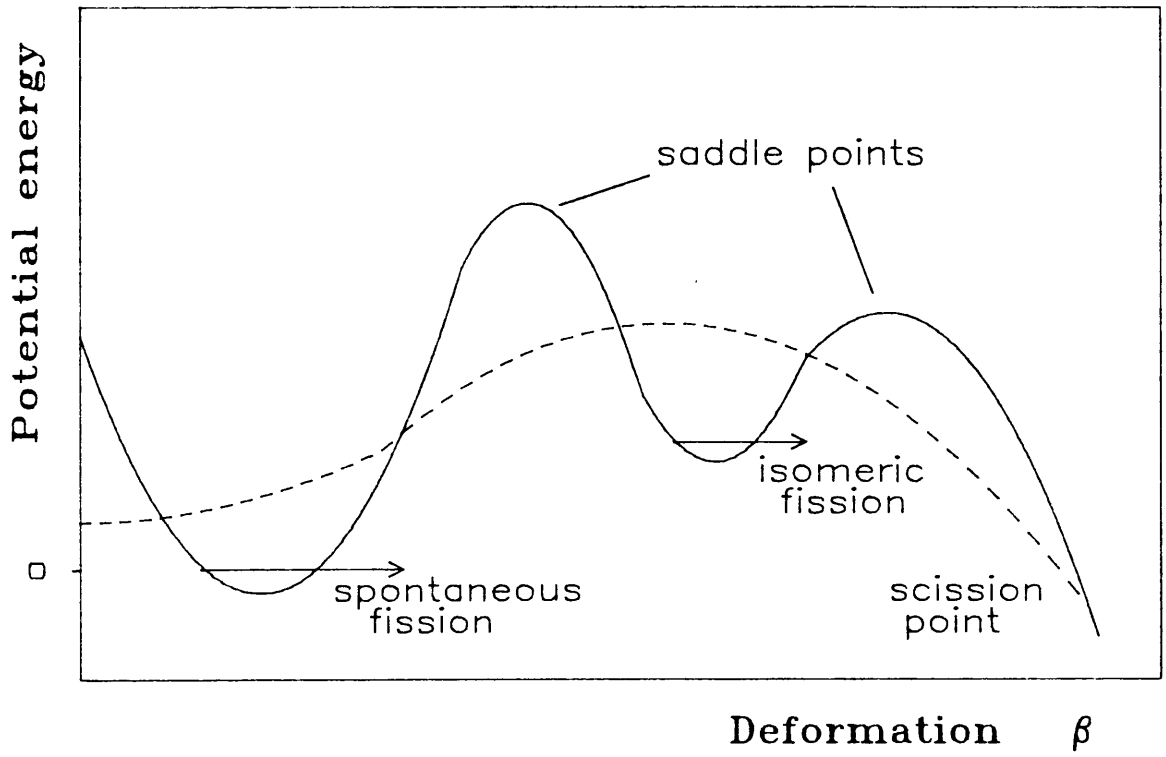

FIGURE 1.1 Model dependence of the shape of the nuclear potential energy as a function of nuclear deformation. Dashed line: simple liquid drop model. Solid line: liquid drop model with shell corrections.

fission, in which, after particle capture, the nucleus does not rapidly fission, but can remain in an excited state for lifetimes of 10^{-9} to 10^{-6} s. It should be noted that the barrier does not necessarily split into one valley, but may in fact have two or more valleys.

1.3 Fragment mass and charge distributions

In general the fission process involves the formation of two fragments close to each other, in the mutually repulsive Coulombic field of their nuclear charges, and is termed binary fission. Ternary fission, which occurs when a light charged particle (mass 1 to 22) is emitted along with two heavier fragments, is observed in less than 2% of fission events. The heavier the tertiary particle, the lower the probability of occurrence.

Since many states are passed through as the nucleus passes over the saddle point and on to the scission point, there is a considerable reorganization of the residual nuclei, which is observed in the form of fine structure in the prompt mass yield distributions. Although a large amount of experimental data on the prompt mass distribution in fission for various nuclei under a variety of conditions have been available for many years, no one suitable theory yet exists which explains all of the observations.

Two types of mass distribution can be observed, 1) primary mass yields, which are the masses of the fragments formed at scission and prior to particle emission, and 2) product mass yields, that is, after prompt particle emission and before β-decay takes place, which is of the order of $\cong 10^{-6}$s. The methods involved to measure primary and product mass yield differ in technique due to the time scales involved. Since typical prompt particle emission takes place within time scales of the order of 10^{-20} to 10^{-18} s, indirect methods of determining the prompt mass yield must be used.

In the 1940s radiochemical methods were predominantly used to determine the product mass yield distributions. As the reproducibility of the results was generally no better than 10%, it was considered reasonable to draw a smooth curve of best fit through the experimental data consisting of, in the case of $^{235}U(n_{th},f)$, two humps centred around masses 96 and 138. This asymmetric distribution of mass is one of the most striking features of almost all spontaneous and low energy particle-induced fission reactions.

Improvements in fragment detection and identification techniques can now provide information concerning both charge Z and mass A of the fission products. From such improved measurements a fine structure has been observed (La80) in the yield distribution as a function of fragment mass, corresponding to shell effects in the fragment nuclei (see Figure 1.2). This fine structure becomes more pronounced at higher fragment kinetic energies (lower fragment excitation energy), the peaking in the mass yield tending towards A = 102-103 due to closed spherical shell configuration (N = 82) for the heavy fragment, and a deformed shell (N = 62) for the light fragment. This shape is consistent with a very compact scission shape (two nuclear centres close together), resulting in the observed high fragment kinetic energy.

At higher initial excitation energies the mass distributions tend towards symmetric mass division due to the fact that there is sufficient excitation energy to overcome the shell effects that are observed in most cases of low-energy fission.

The division of nuclear charge between the fragments is an important parameter associated with the mass distribution in describing the fission process. One of the most striking features of the charge (Z) distributions for fragments of evenly charged fissioning nuclei (La80)

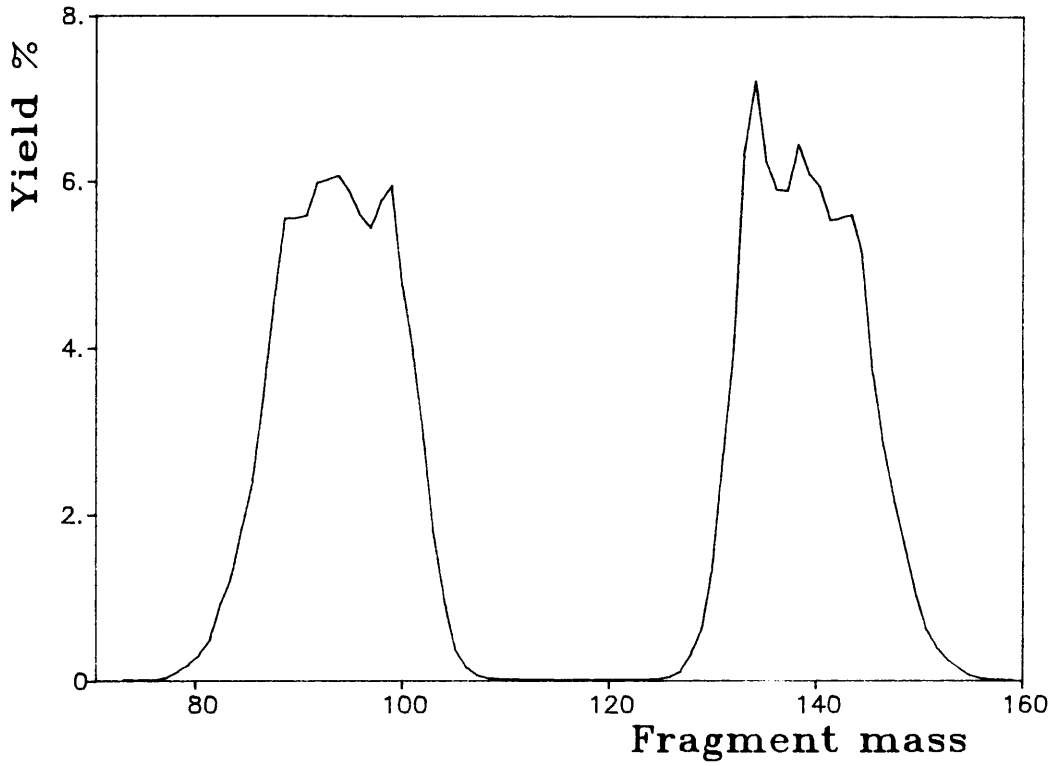

FIGURE 1.2 Average mass yield as a function of fission fragment product mass for $^{235}U(n_{th},f)$. Ref. La80.

is a relatively strong hindrance of odd-charge fragment formation (see Figure 1.3). This is termed the odd-even pairing effect in fission. Fission into two evenly charged fragments liberates, on average, 2.7 MeV more energy than fission into two oddly charged fragments. Experimentally the odd-even fluctuation amounts to about 20% relative to a smoothed Z-yield curve. Knowledge of the charge distributions as a function of fragment mass enables one to consider the shape of fission fragments at scission, since these charges are responsible for almost all of the kinetic energy attained by the fragments in low energy fission..

Knowledge of charge distributions is at present only well known as a function of product mass, since certain assumptions and extrapolations are required to express the charge distribution as a function of primary fragment mass. Figure 1.4 is a plot of the average charge as a function of light product mass determined experimentally (La80).

1.4 Fragment kinetic energy distribution

After scission the separated fragments accelerate away from each other under the action of their mutual Coulombic repulsion, representing a stored energy V_c. For two touching spherical fragments the Coulomb energy is given by:

$$V_c = \frac{Z_1 Z_2 e^2}{r_o (A_1^{1/3} + A_2^{1/3})} \qquad (1.4.1)$$

where Z_1, Z_2 and A_1, A_2 refer to the charge and mass of the respective fragments. Assuming spherical nuclei of radius r_o = 1.3 fm one gets:

$$V_c = \frac{1.2\ Z_1 Z_2}{(A_1^{1/3} + A_2^{1/3})} \quad \text{MeV} \qquad (1.4.2)$$

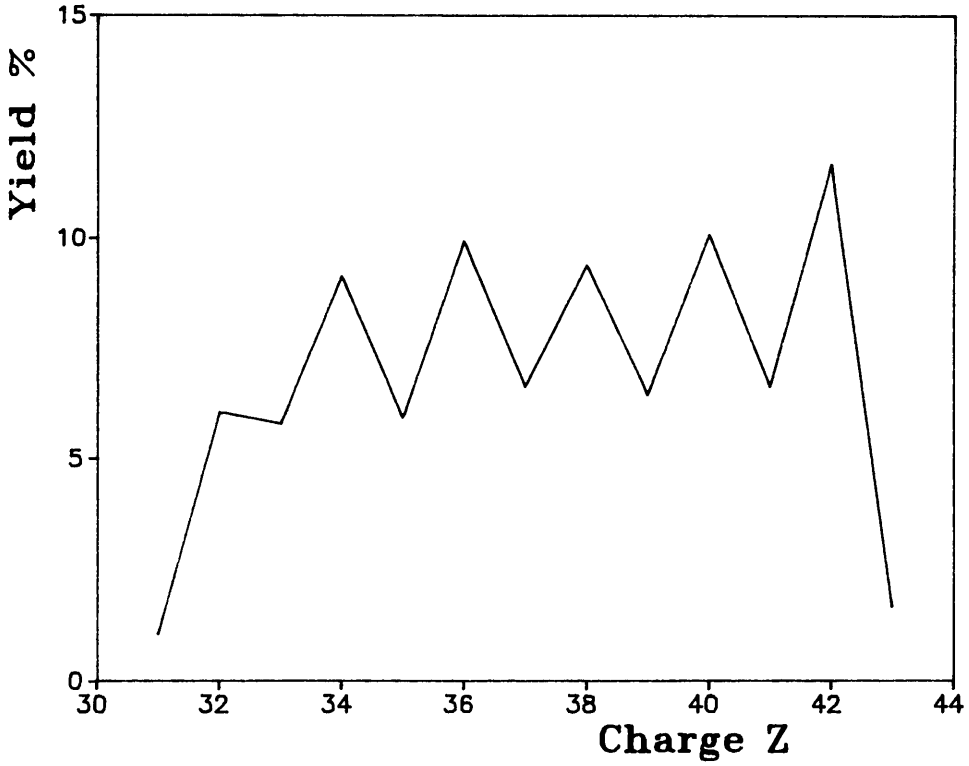

FIGURE 1.3 Average light fragment nuclear charge yield for $^{235}U(n_{th}f)$ demonstrating the odd-even effect. Ref. La80.

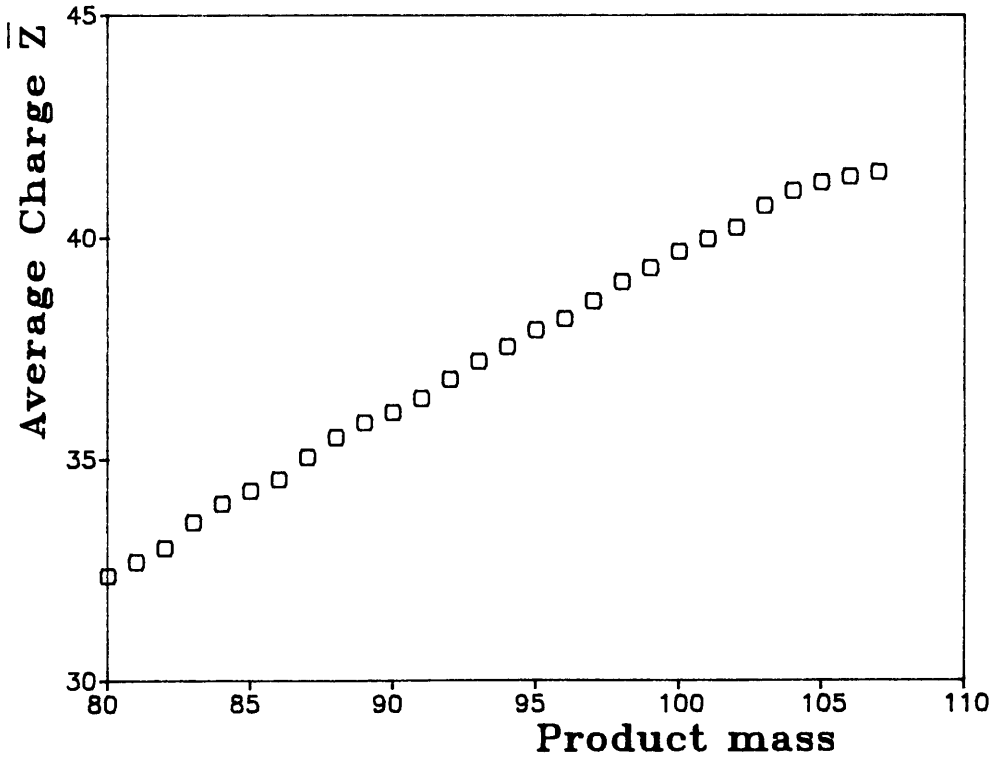

FIGURE 1.4 Average nuclear charge as a function of light product mass for $^{235}U(n_{th},f)$. Ref. La80.

Within the LDM the fissioning nucleus is assumed to consist of a uniformly charged incompressible fluid. There is a surface energy proportional to the surface area of the nucleus, analogous to the surface tension of an ordinary liquid. Distortion to the volume of the drop affects the balance between the attractive surface energy and repulsive Coulomb forces. By expressing the surface in terms of a Legendre polynomial of the form

$$R = R_o(1 + \sum_n P_n(\cos\theta)) \qquad (1.4.3)$$

where R_o is the spherical radius of the nucleus, one can begin to understand the non-spherical shape of the fission fragments at the scission point.

To illustrate the highly non-spherical configuration of the fragments at scission, consider the case of symmetric fission in $^{235}U(n_{th},f)$ where, if one assumes spherical nuclei, from equation 1.4.2 V_c = 259 MeV compared with the experimentally determined value of 167 MeV, which would be equivalent to a spherical nuclear radius r_o = 2.0 fm, which is far from accepted values.

The most prominent structure in the experimental data on total kinetic energy as a function of fragment mass (Ag78, Be83) is the appearance of a dip at symmetry (see Figure 1.5). This can be understood in terms of the shell structure of the fragments in this mass region (A = 116-130), that is, a non-spherical shape which corresponds to a greater separation between the fragment centres and thus lower kinetic energy.

1.5 Fragment de-excitation

Fission fragments are rarely in their ground states at formation, but have internal energy in the form of intrinsic excitations, deformation, rotation and vibration, thus the total energy release at scission can be expressed as:

$$E=V_c+E_{pre}+E_{def}+E_{int} \qquad (1.5.1)$$

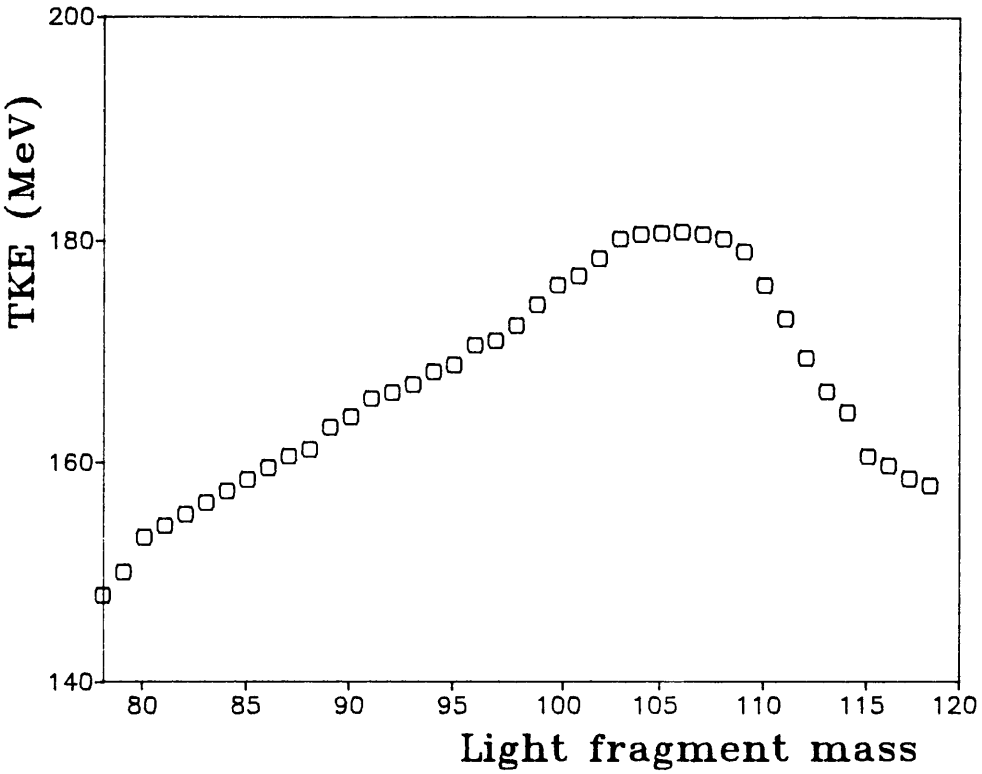

FIGURE 1.5 Average total kinetic energy of the fragments as a function of prompt light fragment mass for $^{235}U(n_{th},f)$. Ref. Ag78.

where V_c is the Coulombic repulsive energy at the scission point, E_{pre} is the pre-scission kinetic energy (that is, relative motion of the nascent fission fragments in the fission direction developed along the path between the saddle and scission point), and E_{def}, E_{int} are the sums of the energies contained in deformation and intrinsic excitation of the two fragments at the scission point. Fragment excitation energy is predominantly tied up in deformation, the remainder being represented by intrinsic excitations of the deformed fragments.

The internal energy at scission is free energy which may be distributed in different ways between the two fragments. The variances of the excitation energies of each fragment, for a constant total kinetic energy, are therefore a measure of this free energy. These variances cannot, however, be directly measured, but must be derived from measurements of the distribution in total energy of particles emitted in the fission fragment de-excitation process.

The highly excited fission fragments lose their excitation energy by the emission of particles and γ-rays. Initially the most favoured form of fragment de-excitation is by neutron emission. The number of neutrons emitted is thus an indicator of the initial fragment excitation energy. The way de-excitation takes place - through neutron and photon emission - together with the mass, charge and kinetic energy distribution, provides the data which give hints about the dynamic processes involved in fission.

Measurements of the multiplicities of γ-rays emitted from fission fragments indicate that the fragments are formed with high angular momentum (Ar71). Neutron emission can only take place unhindered for states which are so high above the neutron emission threshold that high-lying levels, with spin 7-9 $\hbar$, in the daughter nucleus begin to appear. Such states are very rare below an excitation energy of 2 MeV. Gamma-ray emission is therefore able to successfully compete

with neutron emission in an energy interval of about 2 MeV above the neutron emission threshold. This explains the fact that the energy observed in the form of prompt γ-rays is much more than expected on the basis of calculations on the statistical de-excitation of fission fragments.

A total of about 8 photons are emitted in fission, with an average of 1 MeV per photon. This puts an upper limit of about 8 $\hbar$ on the angular momentum of each fragment. The angular momentum is aligned perpendicular to the fission axis, as deduced from observation of a preponderence of E2 radiation along the fission axis (Ar71) - since all torques producing this spin must be perpendicular to the fission axis. Furthermore, measurement of the angular distribution of the prompt γ-rays emitted in fission (Wi72) show an anisotropy with preferential emission of 10-15 % more γ-rays in the fission fragment direction relative to the direction normal to the fragments.

1.6 Neutron emission

The probability of neutron emission from fission fragments, with excitation energy well in excess of the neutron binding energy, is dependent not only on the fragment excitation energy but also on the total angular momentum, J. As has been mentioned earlier, if J is large neutron emission is not necessarily inevitable, but may instead be strongly inhibited with respect to γ-ray emission.

The probability of forming a fragment N(J) with a particular angular momentum J is given by:

$$N(J) = (2J+1)\exp(-J(J+1)/2b^2) \qquad (1.6.1)$$

the parameter b is taken to be 6 on the basis of isomer ratio results (Th67), leading to a most probable angular momentum of 11/2 $\hbar$.

One of the most striking features of the average neutron multiplicity distribution $\bar{\nu}$ as a function of fragment mass A is the characteristic

saw-tooth curve, illustrated in Figure 1.6 for $^{235}U(n_{th},f)$ (Bo71). The shape of the neutron multiplicity distribution, for low energy fission, basically remains the same regardless of the initial fissioning nuclear mass due to shell effects. The deep minimum in the neutron multiplicity distribution for low energy fission occurs close to the mass of the doubly magic nucleus Z = 50, N = 82, where little binding energy is released in the form of fragment excitation energy. Similarly, for very light fragments with neutron number close to the closed shell N = 50, Z ≈ 40 the neutron multiplicity yield is low, again illustrating the strong influence of shell effects in fragment de-excitation.

Measurement of the neutron multiplicity distribution for various fissioning nuclei yield similar curves which, to a first approximation, can be described by a Gaussian distribution, with a width σ = 1.08, about the average total neutron multiplicity (Te65). The average total neutron multiplicity is very dependent on the fissioning nucleus. Table 1.1 is a list of measured average total neutron multiplicity for various fissioning nuclei (Ho85). The uncertainty in the absolute accuracy with which the total neutron multiplicity is determined is demonstrated in Table 1.2 by values published between 1965 and 1985 for $^{235}U(n_{th},f)$ and ^{252}Cf (s.f). When simulating the fission process for $^{235}U(n_{th},f)$ it is therefore important to ensure that the average total neutron multiplicity is reproduced within 1% uncertainty of the experimentally determined value.

When considering the time scale of neutron emission in fission it is necessary to define a time zero, T = 0. Such a definition is complex within the scenario of the fission process. Defining T = 0 at the saddle point prior to scission (as opposed to a saddle point prior to an isomeric state) is not applicable within the concept of tunneling of the potential barrier in spontaneous fission. To define T = 0 at the scission point may also not be realistic with regard to neutron emission during fragment acceleration. The fragment centres (pre-scission) are undergoing considerable changes in velocity due to deformation and vibrational effects and the influence of the Coulombic

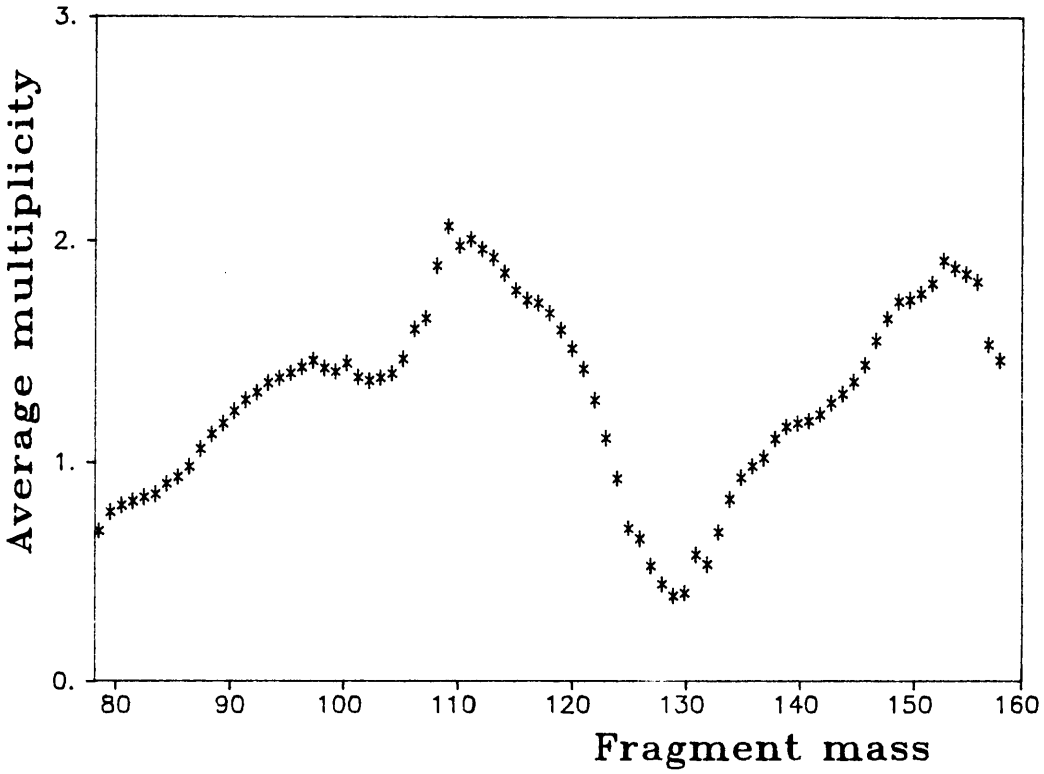

FIGURE 1.6 Average neutron multiplicity distribution as a function of fragment mass for $^{235}U(n_{th},f)$. Ref. Bo71.

NUCLIDE	$\bar{\nu}$ (n_{th},f)	$\bar{\nu}$ (s.f.)
^{230}Th	2.08	
^{233}Th	2.492 ± .008	
^{235}U	2.416 ± .008	
^{238}U		2.00 ± .08
^{239}Pu	2.876 ± .007	
^{241}Pu	2.937 ± .007	
^{242}Pu	2.91 ± .02	2.15 ± .02
^{241}Am	3.219 ± .021	
^{242}Am	3.264 ± .024	
^{243}Am	3.26 ± .020	
^{242}Cm		2.572 ± .02
^{243}Cm	3.40 ± .04	
^{244}Cm		2.74 ± .02
^{250}Cm		3.30 ± .08
^{249}Bk		3.40 ± .03
^{246}Cf		3.18 ± .09
^{249}Cf	4.08 ± .04	3.4 ± .4
^{250}Cf		3.51 ± .04
^{252}Cf		3.764 ± .004
^{253}Es		4.7
^{254}Es		4.2
^{254}Fm		3.99 ± .28
^{255}Fm	4.0 ± .5	
^{256}Fm		3.61 ± .06
^{257}Fm		3.87 ± .05
^{252}No		4.15 ± .3

TABLE 1.1 Average neutron multiplicities for a range of nuclides (ref. Ho 85)

$^{235}U(n_{th},f)$

$\bar{\nu}$	Reference & Year
2.416 ± .008	Bo 67
2.378 ± .014	Ne 70
2.382 ± .008	Bo 70
2.416 ± .005	Le 75
2.4205 ± .012	Le 76
2.436	Bh 80
2.416 ± .008	Bo 80
2.425 ± .003	St 83

^{252}Cf (s.f.)

$\bar{\nu}$	Year
3.713 ± .015	1965
3.796 ± .031	1968
3.725 ± .015	1970
3.766 ± .002	1973
3.725 ± .019	1974
3.747 ± .015	1974
3.744 ± 0.23	1977
3.752 ± .018	1979
3.758 ± .015	1980
3.761 ± .029	1982
3.782 ± .008	1982
3.767 ± .007	1983

Reference: Ho 85

Table 1.2 Typical values of average neutron multiplicity for ^{235}U (n_{th},f) and ^{252}Cf reported between 1965 and 1985.

repulsion between the forming fragments. Such time scales are all extremely short, $\leq 10^{-22}$s, therefore an arbitrarily defined T = 0 will be taken as the scission point.

Neutron emission can be classified into four categories with respect to the arbitrarily defined time zero:

1) Emission from a source stationary in the laboratory frame, that is, before scission, and including the early acceleration period (10^{-21} s) when the forming fragment velocities are low compared with the final fragment velocities. During the period that the nucleus is descending from saddle point to scission point it is energetically possible for neutron emission to occur, as these neutrons would be emitted from a source that is effectively stationary in the laboratory frame of reference. Although their existence is ambiguous such neutrons are termed scission neutrons, and represent not more than 30% of the observed neutrons emitted in fission.

2) During fragment acceleration (10^{-21} to 10^{-20}s). It is generally accepted that 99% of the final fragment velocity is attained in about $4*10^{-20}$s. For neutron emission lifetimes to be of this order requires high excitation energy and/or low neutron binding energy, which is rarely the case in thermal neutron induced and spontaneous fission. These neutrons will be referred to as acceleration neutrons and constitute less than 10% of the observed neutrons emitted in fission.

3) After full fragment acceleration (10^{-20} to 10^{-14}s). It is generally accepted that the most probable neutron emission times occur around 10^{-18} to 10^{-16}s after scission. These neutrons are referred to as prompt fission neutrons and may constitute up to 100% of the neutrons observed in fission.

4) Delayed emission ($>10^{-3}$s), which often occurs after initial β-decay of the fragment. These neutrons are referred to as delayed neutrons and represent less than 1 % of the neutrons observed in total neutron multiplicity measurements.

Information concerning the time of neutron emission relative to scission can be obtained from the directional correlation between fragments and neutrons. The neutrons are most strongly correlated with the fragments if emitted after full acceleration of the fragments, and less so if emitted during acceleration. Such measurements, to date, have been very difficult to conduct as very precise simultaneous information regarding the neutron kinetic energy and fragment mass and kinetic energy is required.

The neutron emission component during fragment acceleration cannot be appreciable due to a combination of factors. From statistical model calculations (Ei65) neutron emission lifetimes for excitation energies of 12 MeV are 10^{-18} s, which corresponds to more than 99% of fragment acceleration. When the excitation energy reaches 50 MeV a lifetime of $\cong 10^{-21}$ s is obtained, corresponding to 50% of fragment acceleration. Experimentally deduced (Sc73) excitation energy release in fission indicates, see Figure 1.7, that only in the mass regions A = 106 to 115 and $A \geq 150$ does the average excitation energy exceed 20 MeV (corresponding to approximately 95 % of fragment acceleration) and reach 30 MeV only around A = 110. These mass regions correspond to a low fragment mass yield region which, when compounded with the average neutron multiplicity, results in a reduced relative neutron yield as is also illustrated in Figure 1.7. Thus less than 10 % of emitted neutrons would be expected to be observed from accelerating fragments with velocities between 10 % and 90 % of final fragment velocity.

An added complication to the analysis of the form of neutron emission is whether the assumption of isotropic emission in the centre of mass frame of the fragments is tenable. As has already been mentioned the fragments have a high angular momentum which tends to promote anisotropic emission in the centre of mass frame of the fragments, and therefore should not be neglected.

Although total neutron emission characteristics have been well measured, knowledge of the fraction of scission neutrons originating in fission, their angular distribution and energy spectra has progressed very little in the 20 years since they were first postulated (Bo62, Fu62), and their existence, both theoretically and experimentally, has

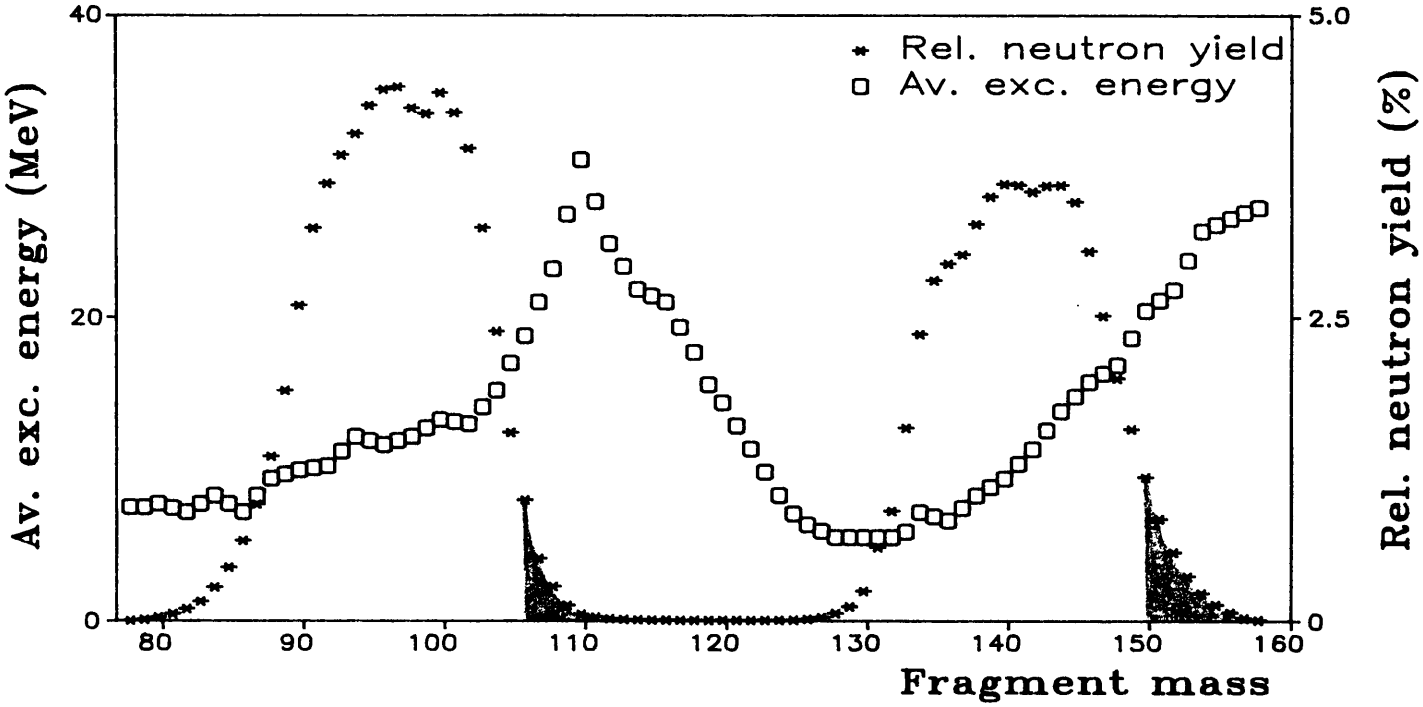

FIGURE 1.7 Experimentally deduced fragment excitation energy compared with the neutron yield weighted by the prompt fragment mass yield. Shaded area corresponds to neutrons which could be emitted during fragment acceleration and for excitation energy in excess of 20 MeV.

not yet been unambiguously demonstrated. To demonstrate their existence requires a full understanding of the neutron energy distribution in fission, and this knowledge can be supplemented by investigation of neutron-fragment angular correlations.

1.7 Energy distribution of fission neutrons

1.7.1 Experimental data

Experimentally it is found that the neutron energy distribution, N(E), in the fragment centre of mass frame can be fairly well represented by a Maxwellian distribution of the form:

$$N(E) = E*\exp(-E/T) \qquad (1.7.1)$$

where T is the nuclear temperature. In the laboratory frame of reference a Maxwellian form may also be used:

$$N(E) = (E)^{\frac{1}{2}} * \exp(-E/T_m) \qquad (1.7.2)$$

where T_m is now the Maxwellian nuclear temperature and for a mean neutron energy, E_{mean}, is derived as $T_m=2/3 * E_{mean}$. In the case of $^{235}U(n_{th},f)$ T_m is 1.28 to 1.33 MeV (St77). A more precise representation in the laboratory frame is the Watt spectrum which is derived from a directionally isotropic Maxwellian distribution, in the centre of mass frame, that has been transformed into the laboratory frame of reference and has the form:

$$N(E) = \exp(-bE) * \sinh \sqrt{(cE)} \qquad (1.7.3)$$

with b=1.0193 and c=2.3075 determined empirically (St77).

Figure 1.8 illustrates the comparison of Maxwellian (T_m = 1.33 MeV) and Watt distributions with experimental data, for $^{235}U(n_{th},f)$, using proton recoil techniques (We72). The divergence of these distributions is particularly marked for neutron energies above 7 MeV and below 0.5 MeV, where it reaches 30%, as is more clearly illustrated

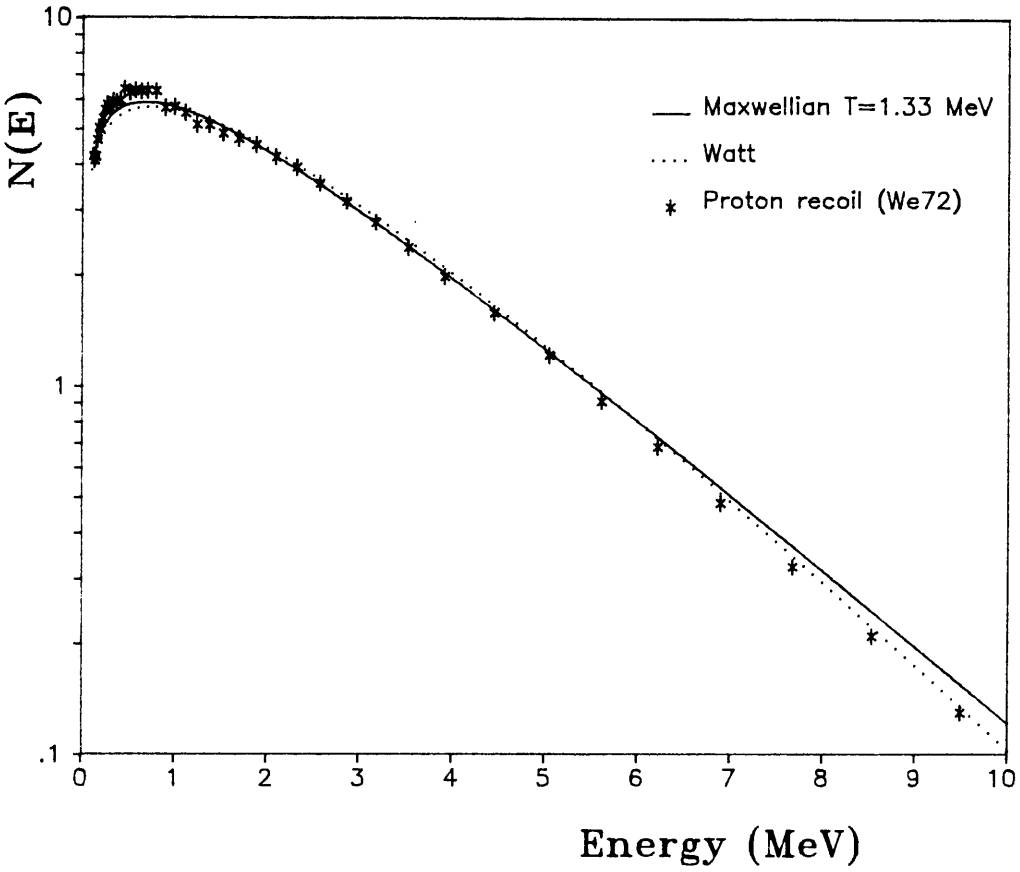

FIGURE 1.8 Neutron energy distribution determined by proton recoil technique compared with calculated distributions.

in Figure 1.9 by the difference plot of the distributions with respect to a Maxwellian distribution. Also shown are results, using a ^{3}He detector, which illustrates the large discrepancies that exist in experimental data dependent on detection technique used.

Lajtai et al (La77) and Starostov et al (St78) have reported measurements of the neutron energy spectrum in $^{235}U(n_{th},f)$ in the low energy region from 30 keV up to 1 MeV, and the results of these measurements are illustrated in Figure 1.10 along with a Maxwellian distribution.

Measurements of high energy neutron emission in fission (^{252}Cf s.f.) indicate (Bo85) a neutron energy distribution with energies up to 20 MeV, and even beyond. Such high energies are difficult to explain with present models of the fission process and do not properly fit within models using a Maxwellian distribution.

Reliable results on neutron emission are only to be expected if the velocity and energy calibrations are consistent with one another. Analysis by Henschel et al (He81) found that in all experiments combining velocity and energy data it was not possible to obtain a satisfactory correlation of the data without adjustments to the calibration. The improper results for fission neutron energy spectra can be due to the neglect in the spread in initial fragment excitation energies. At the same time, partly just for this reason, the centre of mass spectrum of a Maxwellian type invariably seems to give the most reliable fit.

1.7.2 Theoretical models

The picture that emerges from the analysis of neutrons emitted in fission is a mixture of simplicity and complexity. The simple hypothesis of isotropic evaporation from moving fragments, although not quite accurate within the precision of experiments, describes the overall features of the neutrons quite well, even when specific mass groups are selected.

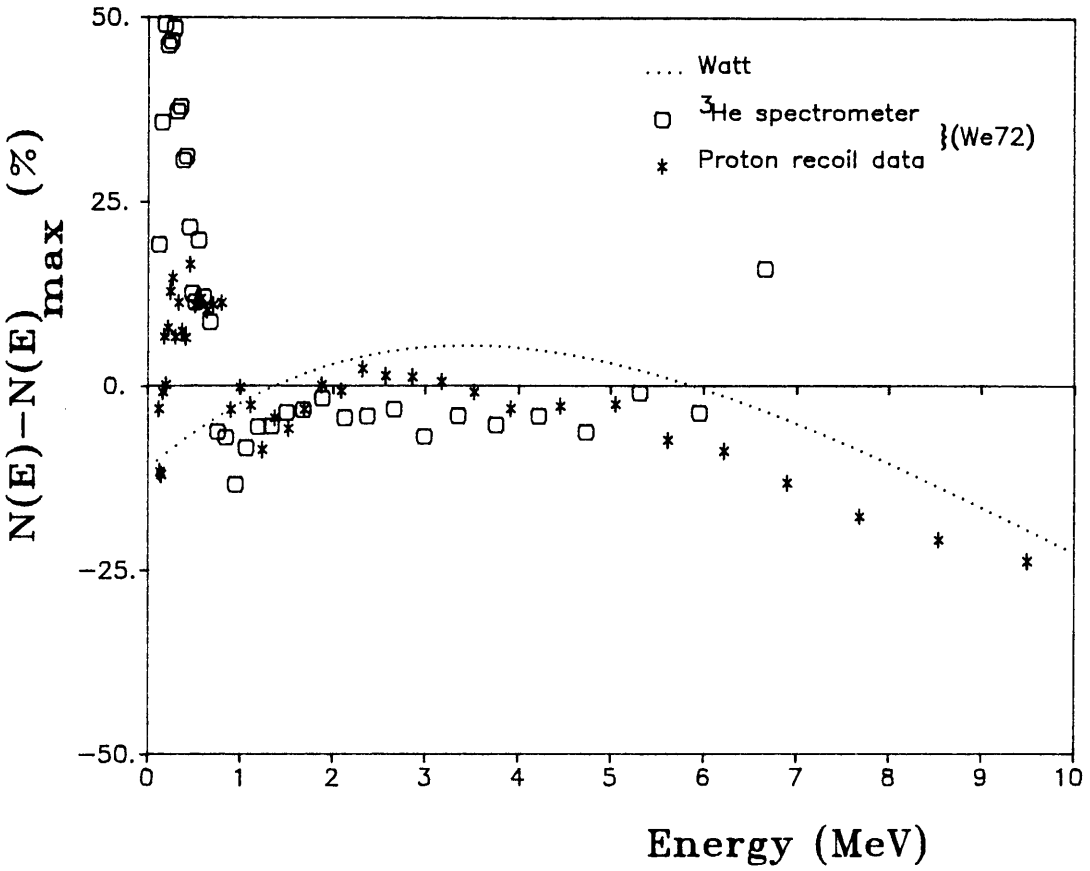

FIGURE 1.9 Difference plot between a Maxwellian distribution and that determined by proton recoil technique, ^{3}He spectrometer and a Watt distribution.

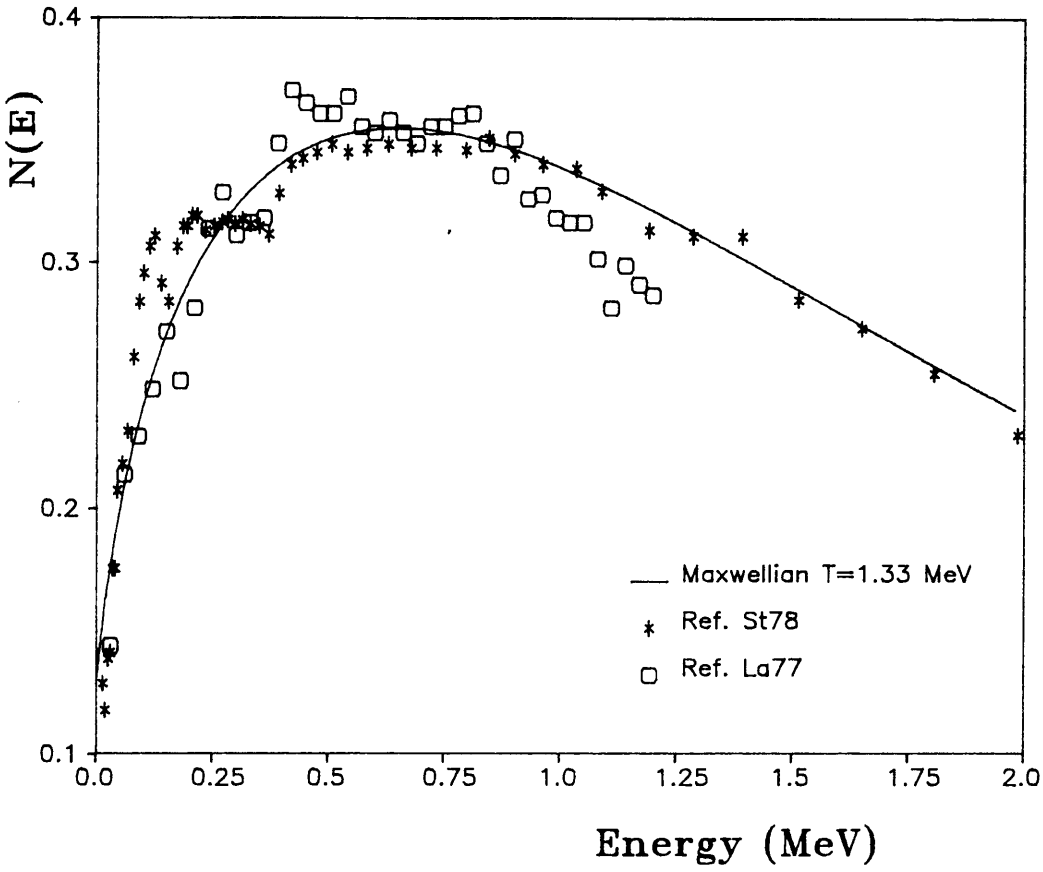

FIGURE 1.10 Low energy neutron energy distribution for $^{235}U(n,_{th},f)$ compared with a Maxwellian distribution.

Various theoretical calculations have been made to describe the shape of the measured neutron energy spectrum. Early descriptions (Te59, La64, Kl71) used a centre of mass energy distribution for neutrons predicted by Weisskopf's evaporation model (We54). Between 1.0 and 5.0 MeV the models gave good agreement with experimental observations. Deviations were seen beyond these limits, the magnitude of the deviation being dependent on the model assumptions.

Green et al (Gr73) developed a model in which there are considered to be three neutron sources, namely from the light and heavy fragments and from a stationary source (scission). The following assumptions were used in the development of the model:

1) The fragments are fully accelerated at the time of neutron emission, except in the case of scission neutrons.

2) In the neutron fragment coordinate system the emission spectrum for each fragment can be characterized by a weighted sum of evaporation spectra, which may be anisotropic, the form of the anisotropy being consistent with the fragment rotating about an axis normal to the direction of motion.

3) The emission spectrum of the stationary source may be characterized by a single evaporation spectrum which may be anisotropic, with the anisotropy symmetric about 90^{o} to the direction of motion of the two fragments. The scission neutrons represented approximately 25 % of the total number of neutrons emitted per fission.

4) The distribution of the kinetic energy per nucleon of a fragment about a mean value may be ignored and the mean value used.

The conclusions of this model were that systematic variations from a Maxwellian fit were observed, particularly below 0.7 MeV and above 8 MeV. The 25 % scission neutron component was emitted preferentially at 90^{o} to the fission axis, and prompt neutrons preferentially along the fission axis.

Analysis of prompt neutrons from fission for $^{235}U(n_{th},f)$ and ^{252}Cf (s.f.) (Sk73) in which emission during fragment acceleration was considered, appeared to remove the requirement of a scission component. However, as has already been mentioned (section 1.6), emission during acceleration requires very high excitation energies which are rarely available in spontaneous and thermal neutron induced fission.

In a study of fusion-fission reactions (Hi84) to describe the neutron emission distribution the possibility of scission neutrons was considered. No convincing evidence was found after considering neutron emission during and after full acceleration.

If the transit time from saddle point to scission point is longer than that normally presumed (as proposed by Nix et al (Ni84, Ni85) and Hinde et al (Hi86)), then there is an increased probability of neutron emission during fragment acceleration, thus reducing the stringent requirement of very high excitation energy. Those neutrons emitted during the saddle-to-scission transit time would, to a first approximation, resemble emission from a source stationary in the laboratory frame of reference, that is, classed as scission neutrons.

Most calculations of neutron energy distribution, are for practical applications, still based on either a Watt or a Maxwellian spectrum, with parameters that are adjusted to optimally reproduce experimental data for a given fissioning nucleus at a given excitation energy. Such an approach cannot be used to predict N(E) for a different fissioning nucleus, or a different excitation energy from what has been measured experimentally, without drastic changes to the input parameters. Furthermore, the assumption of Watt or Maxwellian spectra neglects two important physical effects:

1) The distribution of fission fragment residual nuclear temperature that results from the initial distribution of fission fragment excitation energy and the subsequent cooling of the fragments as neutrons are emitted

2) The energy dependence for the probability for neutron emission seen as the cross-section for the inverse process of compound nuclear formation

A Hauser-Feshbach calculation approach (Br74) removed both of the deficiencies outlined above, but it is sufficiently complicated that it is difficult to apply the model coherently to a variety of fissioning nuclei and initial excitation energies.

A theoretical calculation that is not as complex as the Hauser-Feshbach approach and yet more realistic than a simple evaporation model utilizes the Statistical Model of the nucleus (Ma82). In this model a centre of mass neutron energy distribution, $N(E_{cm})$, for emitted neutrons is assumed to be of the form:

$$N(E_{cm}) = E_{cm} * \sigma(E_{cm}) * \rho\ (E_i - E_b - E_{cm}) \qquad (1.7.4)$$

in which σ is the cross-section for the inverse process, ρ is the density of nuclear energy levels in the final nucleus, E_i is the initial fragment excitation energy, and E_b is the binding energy of a neutron.

In a model still being developed by Nix et al (Ni85), a unified macroscopic-microscopic description of large amplitude collective nuclear dynamics is involved. The model yields results for the total neutron multiplicity, neutron energy, and total fragment kinetic energy distributions in good agreement with experimental data for different nuclei and different initial excitation energies, but still leaves open the question of a scission neutron component. The main disadvantage of the method is the massive amount of computational time required.

1.8 Neutron-fragment angular correlations

1.8.1 Discussion

With the presence of large fragment angular momentum, anisotropy of neutron emission in the fragment centre of mass frame is to be expected, if the angular momentum orientation has a preferred axis. The distribution of states in the residual nucleus is such that the number of available states decreases with increasing spin of the residual nucleus at a given excitation energy. Thus emission of neutrons with orbital angular momentum parallel to the fragment angular momentum direction is favoured, so as to leave the nucleus in a lower spin state leading to a distribution, N(E), in the fragment centre of mass frame, symmetric about 90^{o} to the fission axis and having forward-backward peaking since these directions are contained in all equitorial planes, and can be expressed (Ga76) as:

$$N(E,\theta) = N(E)\ (1+b\ \cos^2\ \theta) \qquad (1.8.1)$$

where θ is the angle of neutron emission with respect to the light fragment direction and b is the anisotropy component. This illustrates that determination of the neutron emission energy spectrum plays a vital role in the estimation of neutron-fragment (n-f) angular correlations. A scission neutron component (emission in a frame at rest in the laboratory frame of reference) will distort the n-f angular correlations since these neutrons will be unaffected by the fragment velocity.

If one considers the effect on the n-f angular correlation for neutrons discernably emitted from accelerating fragments then one is able to reduce the magnitude of the scission component, but not appreciably since, as has been pointed out in section 1.6, the relative number of such neutrons must be small (probably less than 5 %).

1.8.2 Experimental observations

The experimental observations discussed here concern only $^{235}U(n_{th},f)$ n-f angular correlations.

One of the earliest measurements of n-f angular correlations was by Fraser (Fr52) in which the angular distribution of neutrons with respect to the direction of the light fragment was measured for laboratory neutron energies between 0.38 and 8.0 MeV. The results are illustrated in Figure 1.11. A ratio between the neutron intensities $N(0^o):N(90^o):N(180^o)$ of 6.0:1.0:3.25 was obtained. A best fit to the data could be made assuming an isotropic Maxwellian neutron emission distribution in the centre of mass frame of the fragments and with a ratio between the average neutron multiplicities of the light and heavy fragment ($\bar{\nu}_l/\bar{\nu}_h$) of 1.3.

Nefedov (Ne60) reported on measurements of the neutron energy spectra for neutrons emitted at $0^o/180^o$, $40^o/120^o$, and 90^o to the fragment direction (light and heavy) over a neutron energy range 0.23 to 5.0 MeV. Reasonable fits to the data were obtained assuming a Maxwellian neutron emission spectrum in the fragment centre of mass frame, with temperature T = 1.14 MeV for the light fragments and 1.0 MeV for the heavy fragment, and with the assumption that $\bar{\nu}_l/\bar{\nu}_h=1.3$.

Ramanna et al (Ra61) reported angular correlation measurements at three mean neutron energies (0.58, 1.48, 3.0 MeV) for angles with respect to the fragment direction of between 12^o and 58^o. Fits to the data were made assuming a centre of mass Maxwellian neutron emission spectrum with temperature T = 0.98 MeV. Altnough a best fit to the angular correlations was found with the ratio $\bar{\nu}_l/\bar{\nu}_h=1.3$ over all neutron energies, when the fits were compared for separate mean neutron energies the agreement with experiment became poorer with decreasing average neutron energy. To explain this observation it was concluded that an anisotropy in the centre of mass prompt neutron emission of the form $(a + b\cos^2\theta)$ was present for neutron energies of >1 MeV, with a best fit obtained with a = 8.08, b = 9.14.

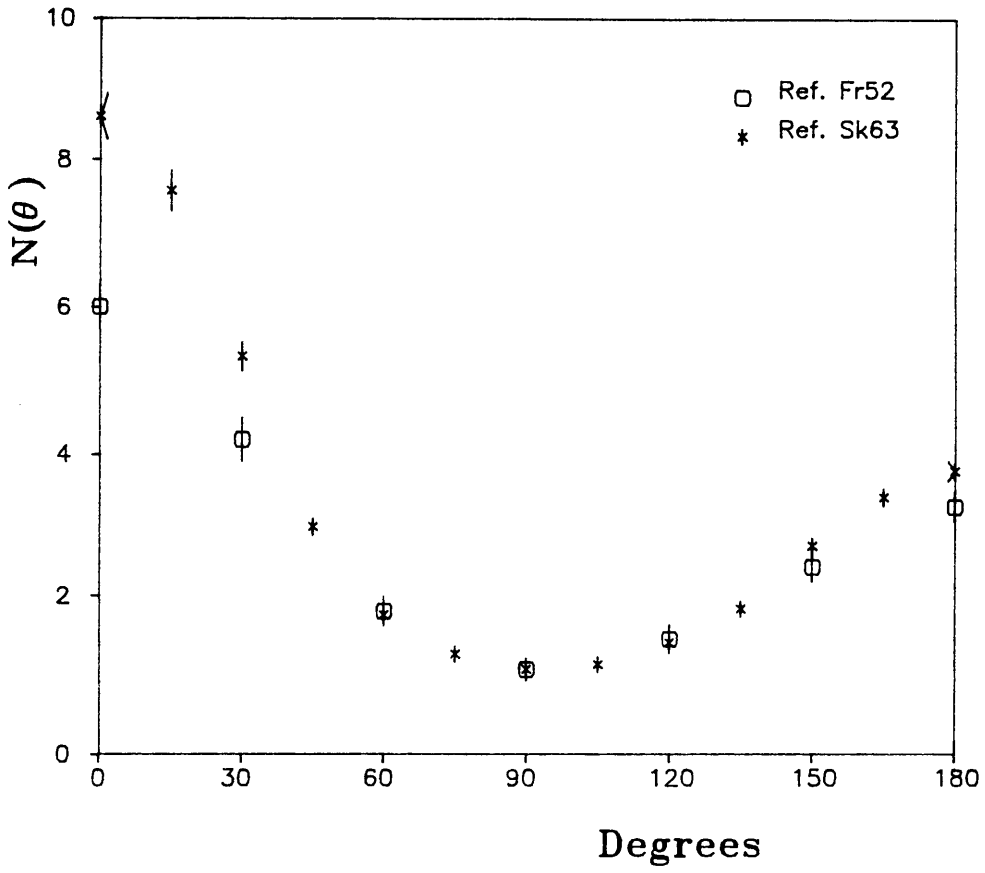

FIGURE 1.11 Neutron-fragment angular correlation with respect to the light fragment direction. Data is normalized to $N(90^{o})$ equal to unity.

Blinov et al (Bl62) reported measurements of the neutron energy distribution emitted at 0^{o}, 45^{o} and 90^{o} to the fragment direction over the neutron energy range 0.25 to 7.25 MeV. An isometric plot of the results is shown in Figure 1.12. Following these results new measurements were reported of the number of neutrons emitted at 0^{o} and 90^{o} to the fragment direction as a function of fragment kinetic energy (Bl71). Interpretation of the results, assuming isotropic centre of mass neutron emission, implied a scission component as great as 30%.

Kapoor et al (Ka63) reported angular correlation measurements with respect to the light fragment direction as a function of neutron energy and for neutron emission angles between 0^{o} and 80^{o} with respect to the light fragment. To obtain a theoretical best fit to the data required a double Maxwellian distribution to be assumed for the light and heavy fragments, with temperatures of 1.105 and 0.705 MeV for the light fragment and 0.885 and 0.485 for the heavy fragment. Also assumed was a $\bar{\nu}_{l}/\bar{\nu}_{n}$ ratio of 1.3 and isotropic neutron emission from fully accelerated fragments. In order to obtain a best fit to the angular distributions, it was necessary to assume that there was a scission neutron component of 10 %.

Skarsvag (Sk63) made detailed measurements of the n-f angular correlation as a function of neutron energy between 0.39 and 11.3 MeV. Figure 1.13 is an isometric plot of the n-f angular correlation data as a function of neutron energy. Integration of the spectra over the measured energy range, 0.39 to 8.0 Mev, yielded a n-f angular correlation illustrated in Figure 1.11. The ratio $N(0^{o}):N(90^{o}):N(180^{o})$ was 8.63:1:3.81 which was more anisotropic than the data of Fraser. In attempting a best fit to the data, it was necessary to assume that 85% of the neutrons were emitted isotropically in the centre of mass of the fragments with a Maxwellian energy distribution and that 15% were emitted as scission neutrons from a frame at rest in the laboratory.

In the twenty years since these measurements, very little new data has been published for $^{235}U(n_{th},f)$ angular correlations. However, from measurement of neutron energy spectra in ^{252}Cf s.f. with respect to

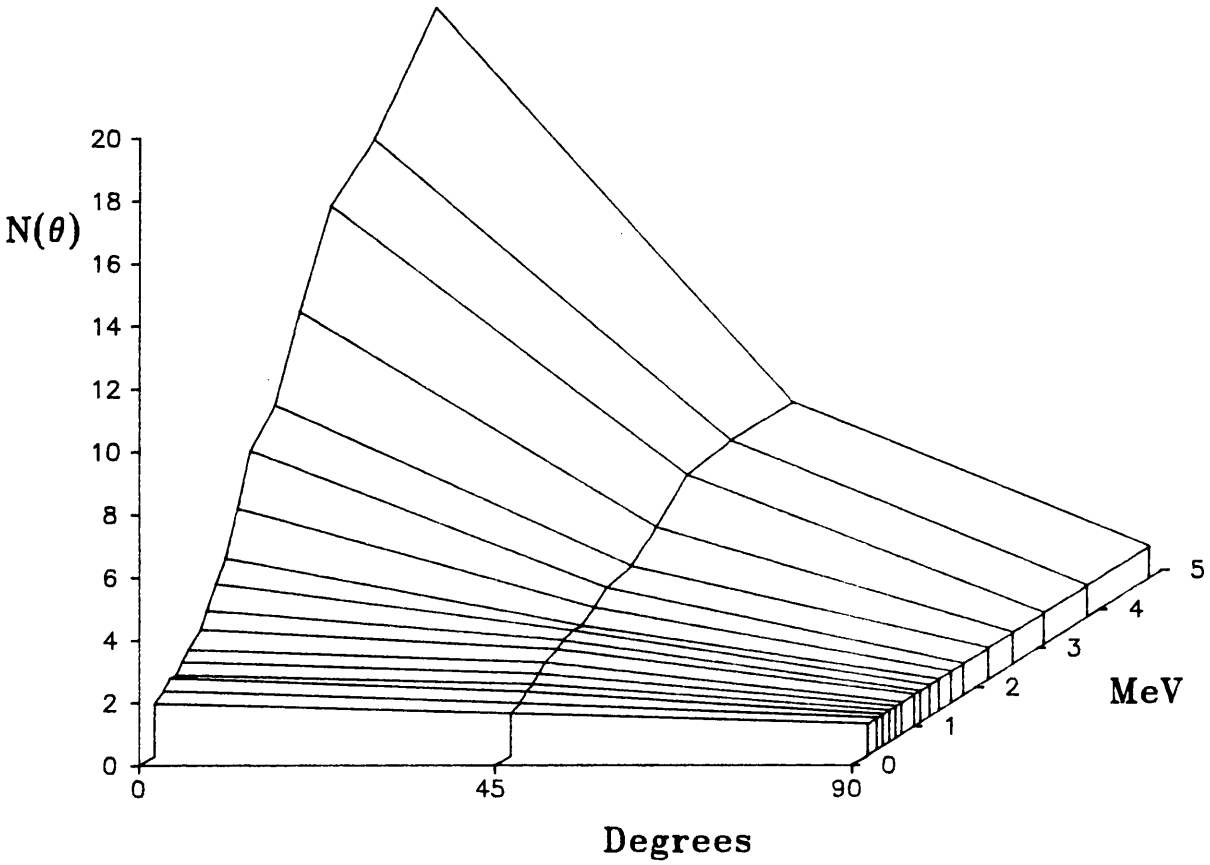

FIGURE 1.12 Neutron-fragment angular correlation as a function of neutron energy with respect to fragment direction (light and heavy) in $^{235}U(n_{th},f)$. Ref Bl 62. Data is normalized to $N(90^{o})$ equal to unity.

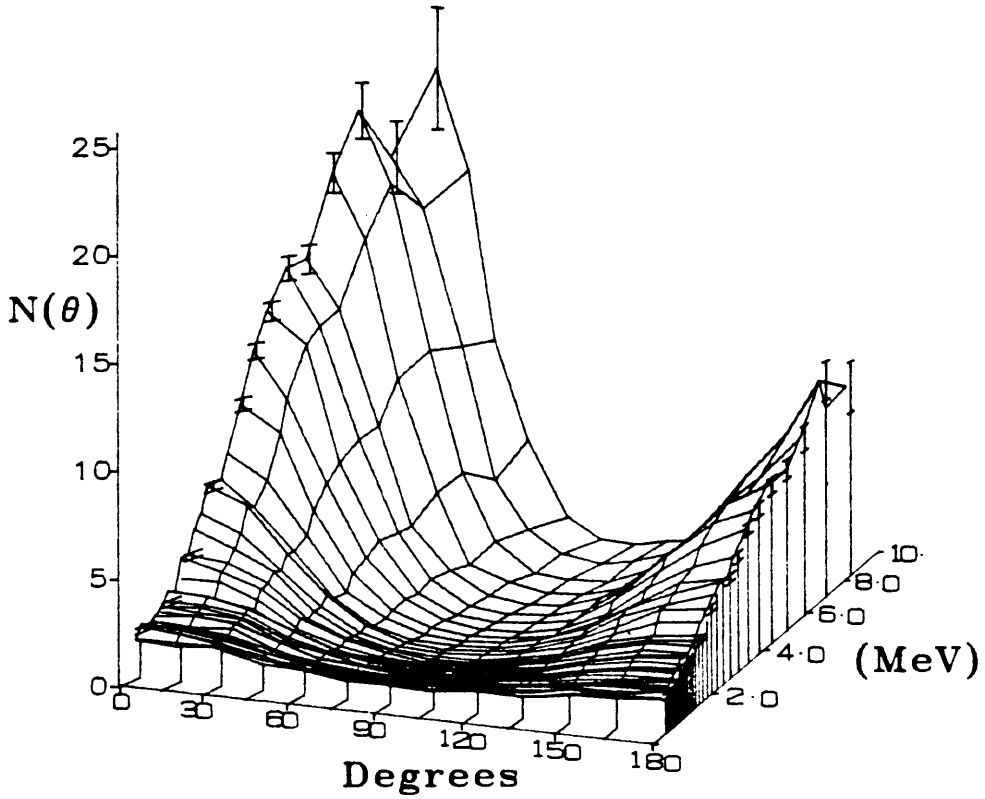

FIGURE 1.13 Neutron-fragment angular correlation with respect to light fragment direction as a function of neutron energy in $^{235}U(n_{th},f)$. Data normalized to $N(90^{o})$ equal to unity. Ref. Sk63.

the fragment direction, the following observations, which are assumed to be applicable to $^{235}U(n_{th},f)$, were made. The average number of neutrons with angular distribution isotropic in the laboratory system amounted to 20 % of the total number of neutrons emitted per fission (Pi77). Also reported (Pi78) was an increase in the neutron yield at angles less than 20^{o} to the fission axis compared with predictions assuming a 10 % isotropic emission from a stationary source in the laboratory frame, which produced a best fit overall.

1.9 Neutron-neutron angular correlations

The angular dependence of coincidences between fission neutrons was studied for $^{235}U(n_{th},f)$ by DeBenedetti et al (Be48), whose results are illustrated in Figure 1.14. From the results it was concluded that there were twice as many neutron pairs emitted by opposite fragments than by the same fragment. This result was to be expected from the simple consideration of approximately two neutrons originating per fission, one neutron from each fragment. The neutrons, being emitted isotropically from the centre of mass frames of the fragments would, on transformation to the laboratory frame, appear in most cases to move in the same direction as their respective source.

Measurement of neutron-neutron (n-n) angular correlations in ^{252}Cf spontaneous fission contradicted this interpretation (Pr75), as did calculations based on neutron-fragment angular distribution data. In fact, almost as many neutron pairs were found to be correlated as being emitted by opposite fragments as by the same fragment (see Figure 1.15).

Measurements of the n-n angular correlation in $^{235}U(n_{th},f)$ (Fr 78), showed a similar trend in the ^{252}Cf data (Pr77) (see Figure 1.16) and contradicted the earlier results of DeBenedetti et al. Simple Monte Carlo simulations of the fission process, comparable to those of Green et al (Gr73) (see section 1.7.2), indicated that a 20 % scission-neutron component was necessary to approximately reproduce the n-f and n-n angular correlations.

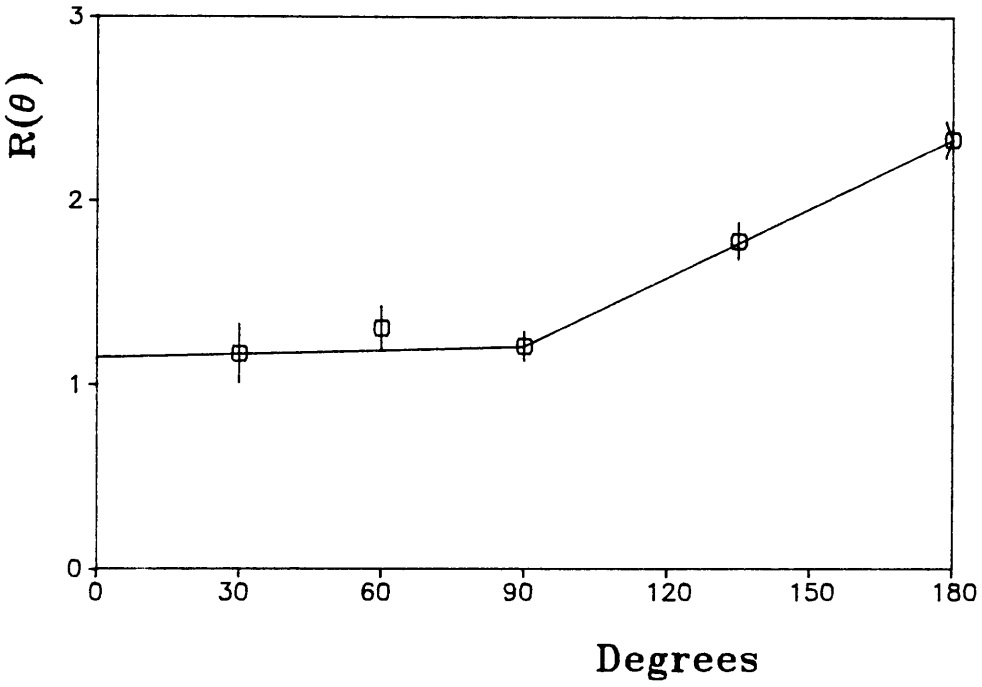

FIGURE 1.14 Neutron-neutron angular correlation in $^{235}U(n_{th},f)$. Ref Be48.

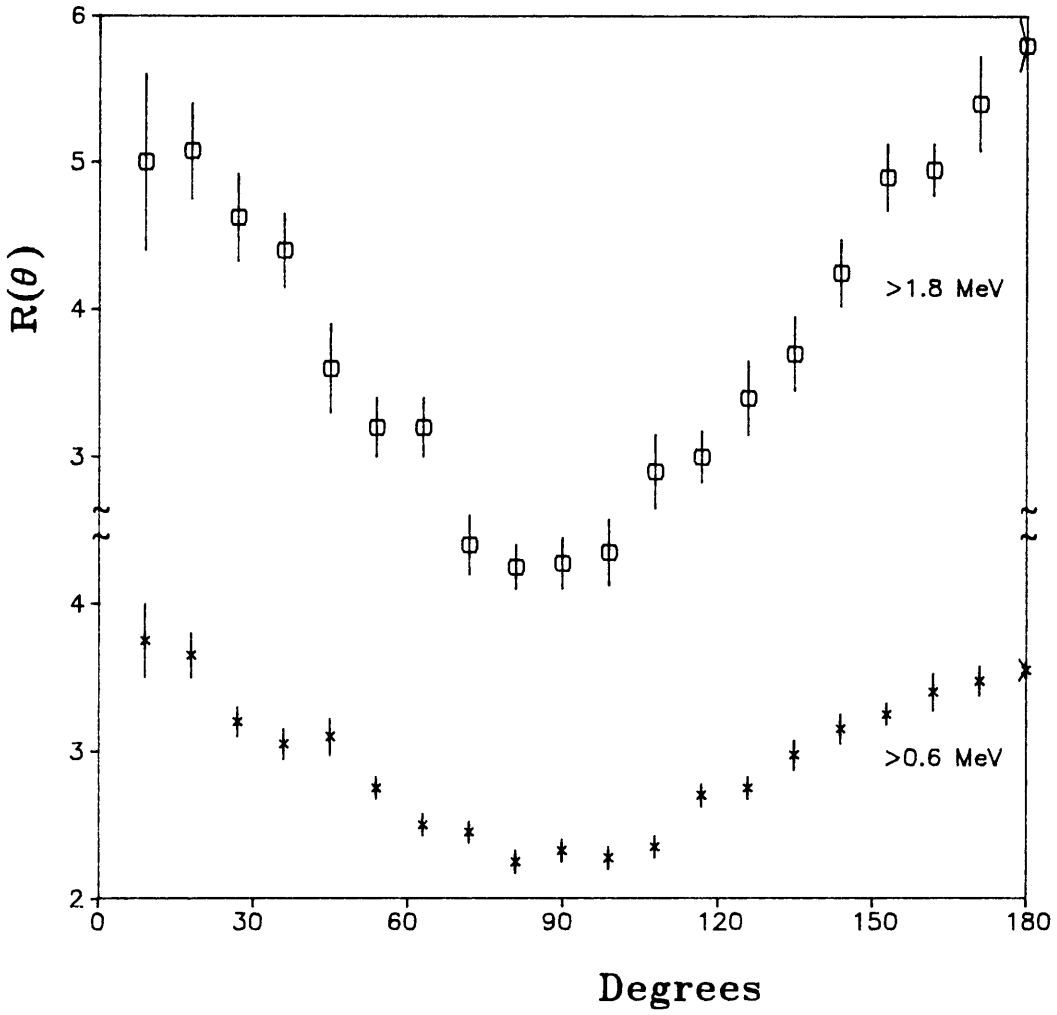

FIGURE 1.15 Neutron-neutron angular correlations for ^{252}Cf(s.f.) for selected neutron detector energy bias cut-offs. Ref. Pr75.

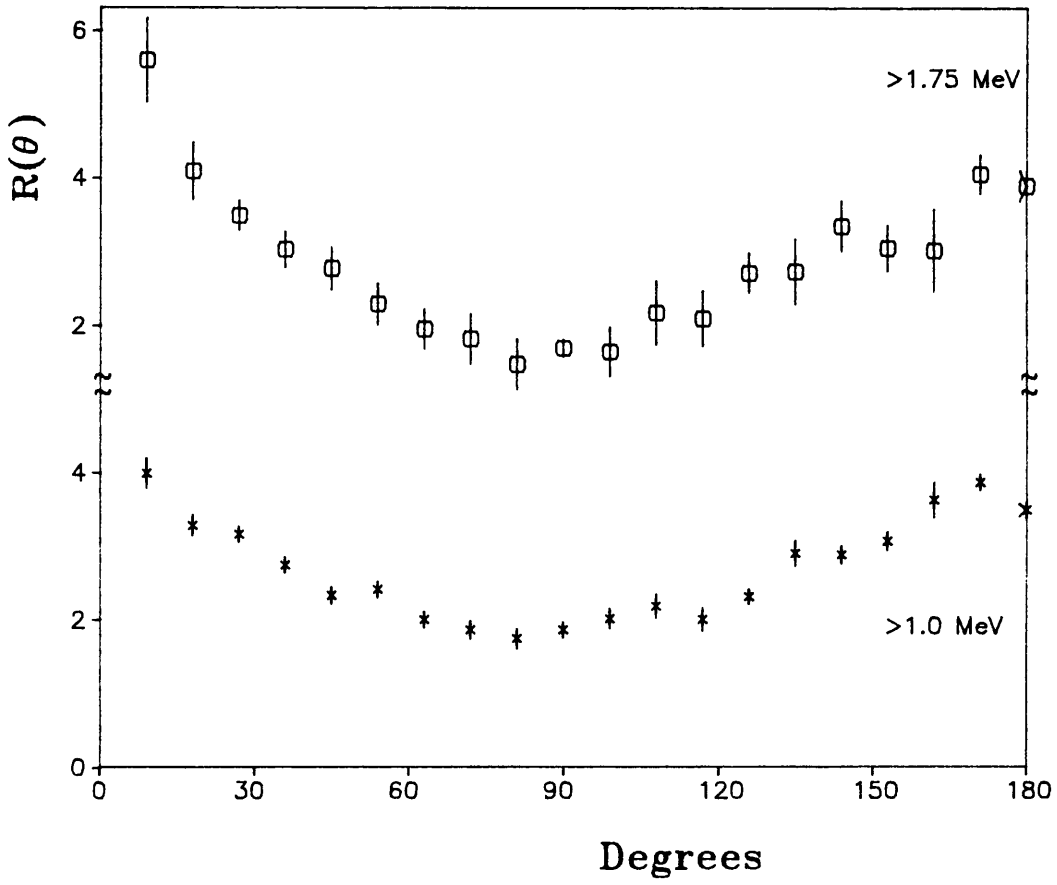

FIGURE 1.16 Neutron-neutron angular correlations for $^{235}U(n_{th},f)$ for selected neutron detector energy bias cut-offs. Ref. Fr78.

In a statistical model calculation of the angular distribution of evaporated neutrons (Ga76) it was deduced that there was an anisotropy in neutron emission of 10 % in the fragment centre of mass system. Using this model to predict the n-n angular correlation resulted in a backward peaking of the distribution in contradiction to the results of Pringle (Pr75, Pr77) and the $^{235}U(n_{th},f)$ data (Fr 78).

2 EXPERIMENT

2.1 Introduction

The experiment was developed as a system suitable for studying angular correlations between fission fragments and neutrons, as a function of fragment mass region (± 3 amu) and fission neutron energy (± 0.5 MeV), in spontaneous and particle induced fission using various types of detector. In describing the development of the system the following areas are highlighted:

1) Thermal neutron beam
2) Fission foil characteristics
3) Fission chamber design
4) Fission fragment detection technique
5) Neutron detection technique
6) Electronic instrumentation for event identification and recording
7) Data analysis

For the measurement of neutron-fragment angular correlations two fragment detectors were used to detect fission fragments emitted within a solid angle about a defined axis through the fragment detectors and source. The coincident fission neutrons, and γ-rays, were detected by an array of neutron detectors arranged in a defined plane through the fission axis.

Fragment mass identification was deduced by time-of-flight techniques and detector pulse height analysis. Neutron energy was deduced by time-of-flight techniques and pulse shape discrimination. Due to intensity and count rate considerations a compromise was reached between angular and energy resolution and count rate for coincident fission fragments and neutrons. The fragment detection system was designed to give a mass resolution of ± 3 amu, which was felt to be adequate for identifying any unusual effects in the neutron-fragment angular correlation distributions as a function of fragment mass region.

2.2 Neutron beam

A filtered neutron beam of temperature approximately 4 meV, from the SAFARI-1 reactor at Pelindaba was used to induce fission in a ^{235}U target. The equivalent thermal neutron flux was approximately $8*10^{6}$ n cm^{-2} s^{-1}, with the reactor operating at 5 MW. The neutron beam was internally collimated to a rectangular shape 4 cm by 2 cm at the aluminium exit windows of the reactor beam tube. Those neutrons that did not interact with the target (or surrounding material) positioned 10 cm from the exit window, exited the fission chamber and were absorbed in a beam stop 2 m downstream.

A separate beam monitor was not used in this experiment; instead the fission rate of the foil was monitored by one of the fragment detectors as is described in more detail in section 2.7.3.

2.3 Fission foil target

In the study of fission fragment characteristics it is essential that the target foil be sufficiently thin to allow fragments to escape with minimal energy degradation and yet thick enough to have a suitable macroscopic fission cross-section. In considering such factors as incident neutron flux, target area, fission rate and fragment energy loss characteristics, a foil thickness of 1 mg cm^{-2} ^{235}U was eventually chosen.

Thin foils of approximately 1 mg cm^{-2} thickness and 25 mm diameter of highly enriched (99.524%) ^{235}U foils were obtained from the Central Bureau for Nuclear Measurements, Geel, Belgium. The foils were produced by uranium oxide suspension spray deposition onto a thin (30 µg cm^{-2}) Polymid film onto which 20 µg cm^{-2} of gold had already been deposited to facilitate bonding of the uranium to the target foil. The Polymid film was supported on an aluminium ring of 50 mm outer diameter and 30 mm inner diameter and 1 mm thickness, and this ring was supported in an aluminium frame attached to the window of the fission chamber, through which the beam entered.

In this experiment a foil of quoted average thickness 869 μg cm^{-2} was used, but as can be seen from the optical transmission image of a second similar foil (Figure 2.1), visual inspection of the foil implied considerable non-uniformity in the spatial distribution of uranium. The deposition technique is generally considered to be capable of producing a uniform target with deviation of less than 10 % from homogeneity. Since the required thickness is obtained after repeated passes, it is normally assumed that the final homogeneity is better than 10%.

In Appendix A is a description of an experiment undertaken to estimate the actual variation in spatial distribution of uranium over the foil by a novel, non-destructive technique of proton-induced X-ray emission (PIXE) measurement. This measurement was motivated by the results for the detected fragment energy distribution, which are described in section 3.2.1, and from visual inspection mentioned earlier. The main conclusion of the measurements was that the variation in uranium thickness was on average 30 %. Deviations greater than 50 % were observed at a spatial resolution of 0.5 mm, and greater deviations were implied for finer spatial resolution.

2.4 Fission chamber

Energy degradation of the fission fragments outside the foil was minimized by the provision of a suitable vacuum. The design of a vacuum chamber took into account the following factors:

1) Easy mounting and dismounting of the fragile fission target inside the chamber

2) Minimum interference by the material constituting the vacuum chamber to the incoming thermal neutron beam, the fission fragments and outgoing fission neutrons and gamma-rays

3) Adaptability to accommodate different types of fission fragment detector

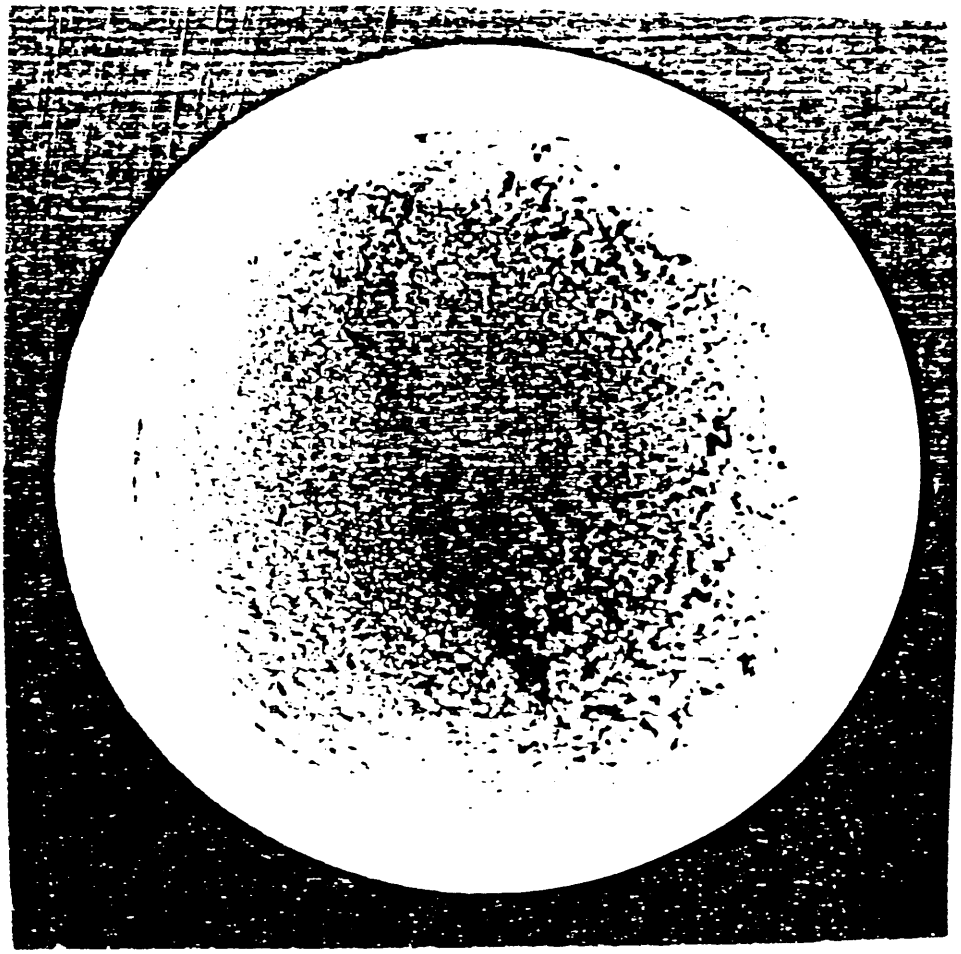

FIGURE 2.1 Optical transmission image of a uranium foil similar to the one used in the experiment.

4) Symmetric design to the plane perpendicular to the fission fragment detection axis and bisecting the fission foil, to minimise asymmetric background effects

5) Ease of creating and maintaining a suitable vacuum

6) In the case of possible serious contamination of the chamber, the ability to isolate the chamber

Figure 2.2 is a scaled diagram of the fission chamber used in this experiment, illustrating the target area, fragment detector location and vacuum pump facility. The chamber and surrounding material were made up mostly of aluminium in order to reduce neutron interaction with this medium.

The vacuum in the chamber was formed using sorption pumps, the sorption material being cooled to 77^{o} K by immersing the pump vessels in liquid nitrogen. The pressure inside the vacuum chamber was maintained at less than 10^{-4} Torr. Fission fragment energy loss at this pressure was negligible, being of the order of 0.1 MeV for a flight path of 20 cm, for a typical fragment of 100 MeV in kinetic energy.

The fragment detector position was easily adjustable (without affecting the status of the vacuum) to be anywhere between 2 cm and 30 cm from the fission foil. The positioning of the fragment detectors was decided upon by consideration of the angular and kinematic resolution to be achieved in this experiment. For flight paths d_1 and d_2 for the two fission fragments, a time of flight (TOF) difference, T, for the detection of the respective fragments is given by

$$T = \frac{d_1}{v_1} - \frac{d_2}{v_2} \qquad (2.4.1)$$

where v_1, v_2 are the actual velocities of the fragments arriving at the detectors, due to the kinetic energy loss of the fragments. The measured fragment velocity is related to the initial prompt fragment

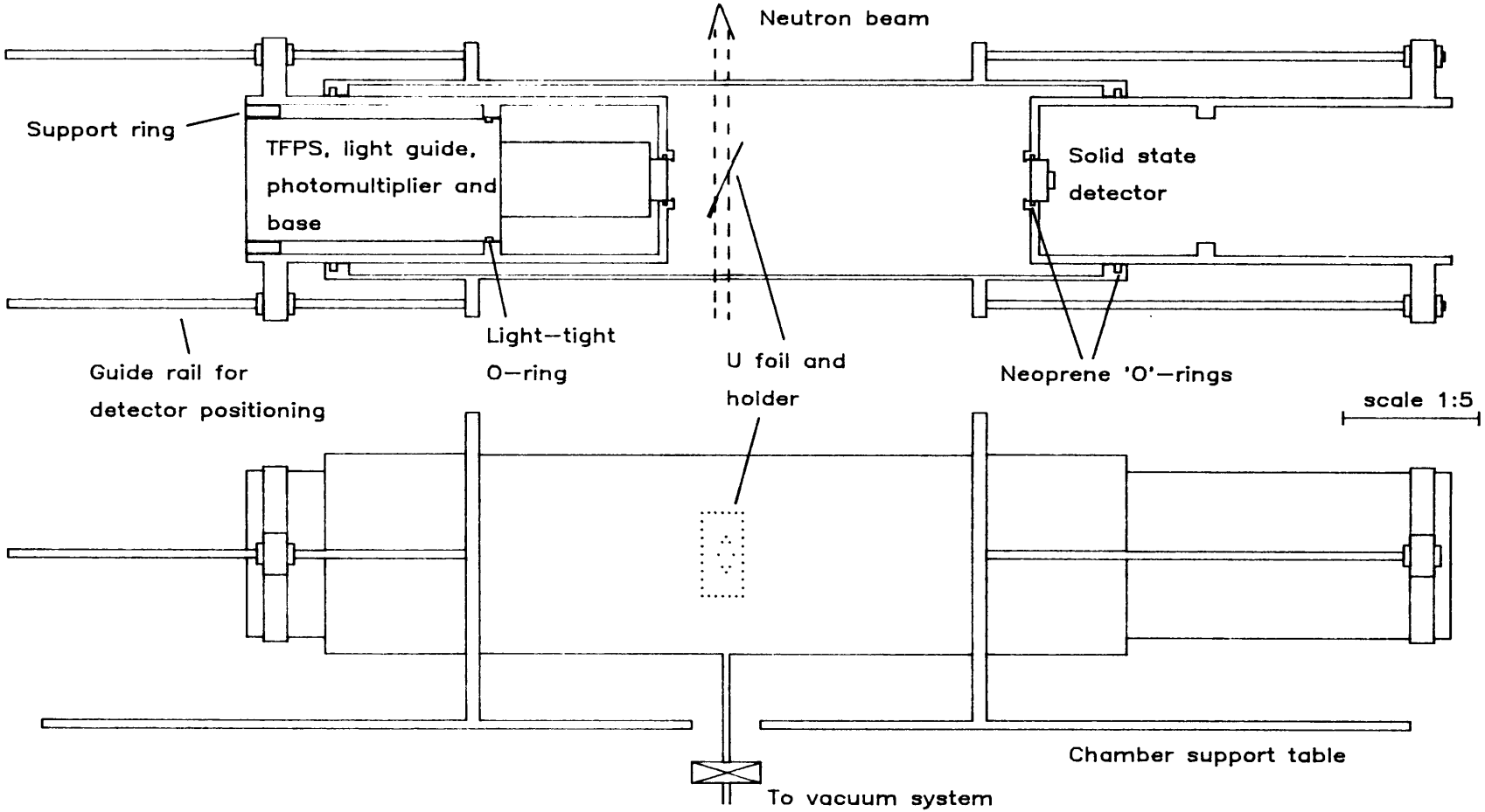

FIGURE 2.2 Schematic plan and side view of the fission chamber used in the study of $^{235}U(n_{th},f)$.

velocity by $v_1=V_1 - k_1$ and $v_2=V_2 - k_2$ respectively, where V is the initial prompt fragment velocity and k is the velocity reduction (due to energy loss) experienced by the fragment traversing the foil, the energy loss in traversing the vacuum to the detectors being negligible.

Due to the finite size of the fragment detectors there is a dispersion ΔT in the TOF difference, defined as:

$$\Delta T = \frac{(1 - \cos\alpha)}{\cos \alpha} \left[\frac{d_1}{v_1} - \frac{d_2}{v_2} \right] \qquad (2.4.2)$$

where α is the maximum angle subtended between the two detectors (see Figure 2.3).

An angular resolution for neutron detection of 10^o was arbitrarily chosen for this experiment. On this basis an angular resolution for neutron-fragment detection was also set to 10^o, thus defining $\alpha \cong 5^o$.

It can be seen in equations 2.4.1 and 2.4.2 that making d_1 (or d_2) small reduces the effect on ΔT due to energy loss (straggling) of one of the fragments. An ideal situation would be for d_1 (or d_2) equal to zero. However, for practical reasons (for example, neutron beam interference with the detector) a minimum distance for d was 5cm. On this basis the fragment detector positions were chosen to be: d_1 = 5 cm, d_2 = 20 cm to yield an $\alpha \cong 5^o$. For unstraggled fission fragments $\Delta T < 0.2$ ns.

A convention is defined here for this experiment in which the frame of reference 0^o implies a fragment travelling in the direction of the particle detector d_1 (distance = 5 cm) (see Figure 2.3). Conversely, 180^o refers to a particle travelling towards detector d_2 (distance = 20 cm).

To utilize the full neutron beam area the foil was aligned at 30^o to the beam direction. The effect of this alignment on the TOF dispersion was considerable. For fragments travelling parallel to the axis 0^o-180^o (see Figure 2.3) a maximum dispersion can be expressed as:

$$\Delta T_{max} = (d_1 + d_2) \tan \alpha \quad \tan 30 \left(\frac{1}{v_1} + \frac{1}{v_2}\right) \qquad (2.4.3.)$$

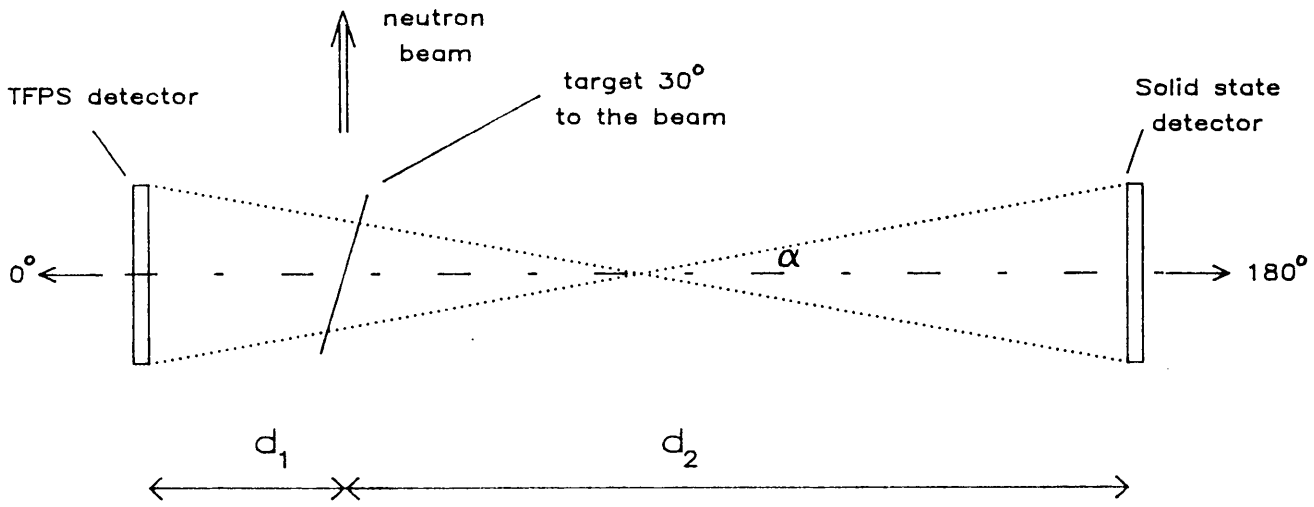

FIGURE 2.3 Illustration of maximum angular dispersion of fission fragments from the defined axis 0^{o}-180^{o}. The detector distances are relative to the centre of the target foil.

which for the defined detector positions results in a ΔT_{max} = 2.5 ns for mean fragment velocities (unstraggled). Fortunately the probability of fragment-fragment coincidence events originating from this region of the foil is negligibly small compared with events from other areas of the foil. For fragments subtending the maximum angle between the detectors ΔT is defined as:

$$\Delta T = \frac{\tan\alpha \tan 60\ (d_1 - d_2)}{\cos\alpha\ (\tan^2 60 - \tan^2\alpha)} \left[\frac{1}{v_1} + \frac{1}{v_2} \right] \qquad (2.4.4)$$

which, for mean unstraggled fragment velocities, results in a ΔT of 1.5 ns.

A Monte Carlo simulation of the fragment-fragment TOF difference distribution for a typical fission experiment, for a detection system with d_1 = 5 cm, d_2 = 20 cm, tan α = -0.1 to +0.1 and 1 mg cm^{-2} fission foil at 30^{o} to the incident neutron beam, is illustrated in Figure 2.4. Also shown in the figure are the calculated TOF differences for specific fragment masses moving towards the 0^{o} detector. It can be seen that merely from TOF difference measurements a light mass resolution of 10 amu would be clearly obtainable. To obtain similarly clear mass resolution for detection of heavy fragments, at the 0^{o} detector, requires utilizing the pulse height information from the fragment detectors.

2.5 Fragment detection

There are several methods of detecting a fission fragment, which is an energetic (40-120 MeV), highly ionized atom with charge state q between 10 and 40. As these fragments lose energy through inelastic collisions, where energy is transferred to the electronic structure of the medium surrounding the fragment flight path, they also gain electrons so that the energy loss dE over a distance dx, dE/dx, is greatest at the start of their track and least at the end, where it is mainly confined to elastic collisions in which the energy is transferred to the atom as a whole.

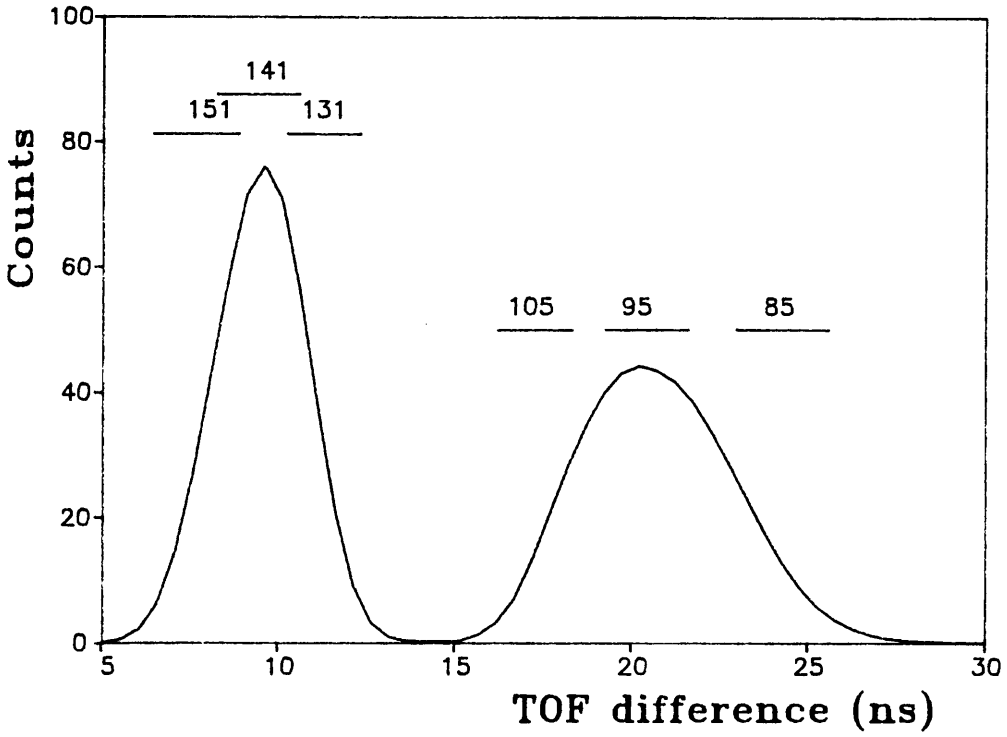

FIGURE 2.4 Predicted time-of-flight difference between correlated fragments. The calculated FWHM of the TOF distribution for specific fragment masses arriving at the 0^{o} detector are indicated. Calculations were based on a uniform 1 mg cm^{-2} uranium foil.

The function of the fragment detectors was to determine, approximately, the mass and kinetic energy of the fragments. This was to be done by simultaneous measurement of the time-of-flight difference between the fragments and energy deposited in the detector.

Three types of detector were initially considered for this experiment

1) Ionization chambers, which have in recent years become increasingly popular because of their high count rate capability without detection efficiency degradation and energy and position resolution capability. Ionization chambers operate on the principle of collecting the ionization induced by fission fragments traversing the chamber gas. To minimize fragment energy loss the target needs to be placed inside the chamber. Due to the difficulty of maintaining such a system for various fission sources and the complexity of the electronics support needed for such a chamber, ionization chambers were not used for this experiment.

2) Solid state detectors (SSD) have good energy resolution and timing characteristics in the detection of heavy ions. The pulse height response of these detectors, while linear with energy for a given ion mass, exhibits a pulse height defect which is mass dependent (Sc65). When a fission fragment enters the active region of the detector through a thin insensitive window (usually gold), the fragments lose their energy essentially by Coulomb interaction with the nuclei and electrons of the silicon atoms. The interaction with electrons results in electron-hole pair creation, and these pairs are removed by the electric field produced by the applied bias voltage. The amplitude of the resulting integrated current signal is equivalent to the energy deposited by the fragment in electronic collisions in the sensitive region of the detector. The energy spent in interactions with nuclei is not detected and is the energy (or pulse height) defect. The greatest disadvantage of using these detectors is that the radiation damage caused by the fission fragments and by the associated neutrons, alpha and beta radiation, progressively causes a deterioration in resolution

and efficiency of the detector and ultimately, after 10^8 - 10^9 particles per cm^2, detector breakdown. For a low coincidence rate experiment, such as is the case of this experiment, this was a factor which had to be considered carefully.

An Ortec F-type surface barrier SSD was used during the main part of the experiment data acquisition. The detector had a sensitive thickness of 60 μm (sufficiently thick to stop all fission fragments) and an active area of 300 mm^2, and was operated at a recommended bias voltage of 83 V. Using an ORTEC 142A pre-amplifier, signals were supplied for use in pulse height (energy) and fast timing analysis.

3) Plastic scintillation detectors are an extremely reliable means of detecting fission fragments with virtually no deterioration in performance due to intense irradiation, even over long exposure times. Specifically, one is referring to thin film plastic scintillators (TFPS), sufficiently thick to detect fission fragments and thin enough to virtually eliminate detection of gamma-rays, beta particles and neutrons. Such a thickness ranges from 0.25 μm to about 60 μm.

NE810 plastic scintillators are suitable available detectors, consisting of 25 mm diameter TFPS (38 μm thick) mounted on a light guide 3 mm long. The advantage of this detector was ease of handling and a proper optical coupling to the light guide. The light guide acted both as a connection, through a suitable optical couplant, to a photomultiplier tube, and sealant of the vacuum chamber, as can be seen from the illustration of the fission chamber in Figure 2.2. RCA8575 type photomultiplier tubes were used with all scintillation detectors and these in turn were mounted on ORTEC 270 constant fraction timing photomultiplier bases, to supply both a pulse height signal (energy) and constant fraction fast timing signal.

The time-of-flight (TOF) difference between coincident fragments was recorded for each valid fission event using the fast timing signals, along with the respective fragment detector pulse heights.

The experiment was divided into two data acquisition series. The first series, A, consisted of operating with two TFPS fragment detectors, the second series, B, with one TFPS and one SSD. The detector position d_1 and d_2 were 5 and 20 cm for both series, with the SSD at d_2. Comparison of the coincident fragment pulse heights and TOF data yielded useful information concerning the detection characteristics of TFPS and SSD. Figure 2.5 shows plots of the TOF difference versus pulse height of coincident fragments for typical data runs from the two data series. By analysis of the TOF and pulse height response in TFPS (see section 3), the resultant pulse height distribution as a function of mass (Figure 2.6), was found to be comparable with published data (P182).

Verification of some of the detection characteristics of the experiment was made at the conclusion of the data acquisition using a thin ^{252}Cf (s.f.) foil target.

Neutron detection

For neutron spectrometry covering neutron energies from around 0.5 MeV up to 10 MeV, only proton recoil scintillation counters can cover the whole energy range with satisfactory detection efficiency. A typical neutron scintillation detector is NE213, which is a liquid solution of xylene, naphthalene and a light spectrum shifter. Besides recoil protons, recoil electrons will also be present due to γ-ray interactions. In the case of electron detection above 100 keV the light output is a linear function of electron energy, hence the electron response of the scintillator can be determined from the positions of the Compton edges in the pulse height spectra for standard γ-ray sources, such as ^{137}Cs, ^{22}Na and ^{60}Co.

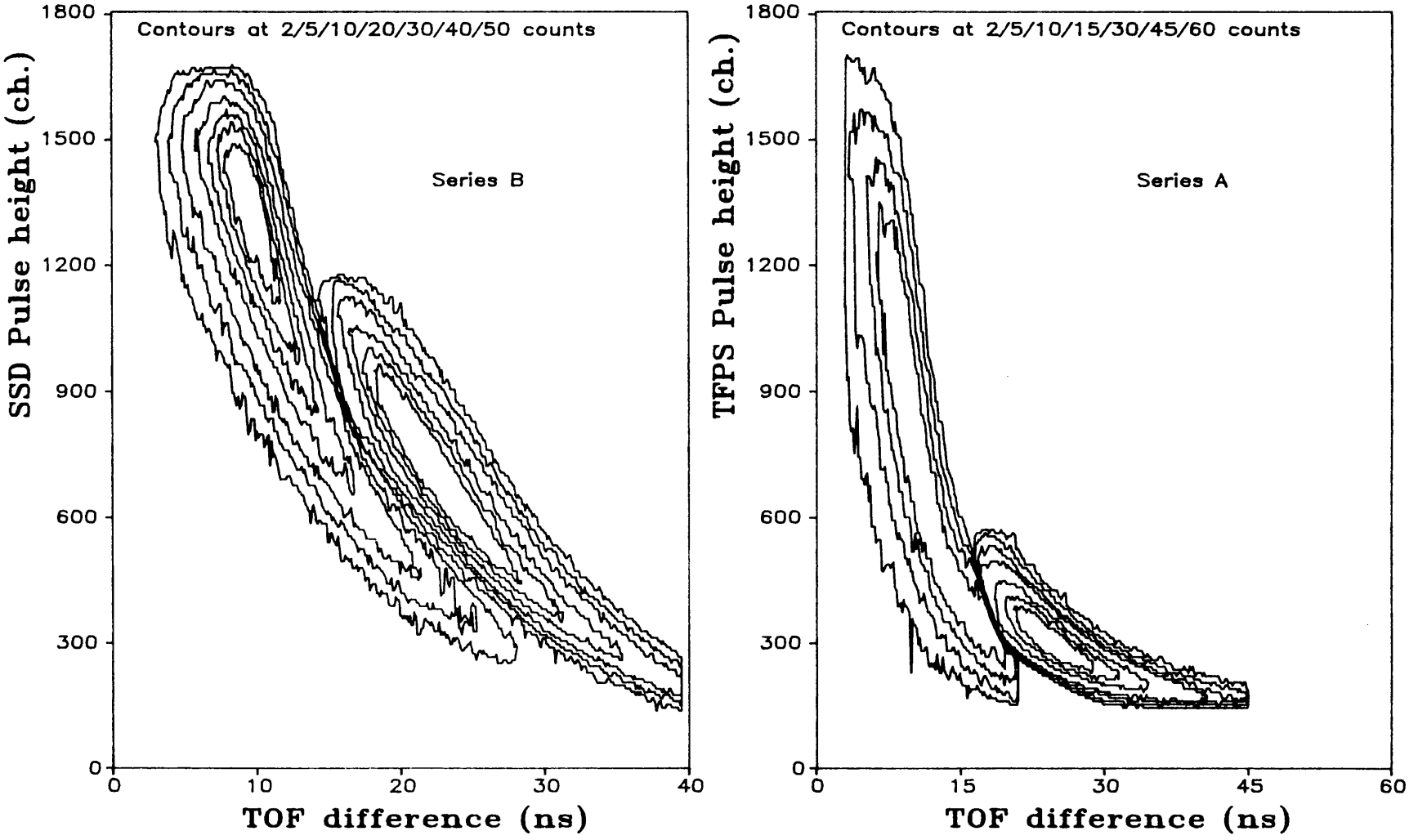

FIGURE 2.5 Measured fragment-fragment time-of-flight difference as a function of the 180^{o} fragment detector pulse height, for the two run series using different fragment detectors.

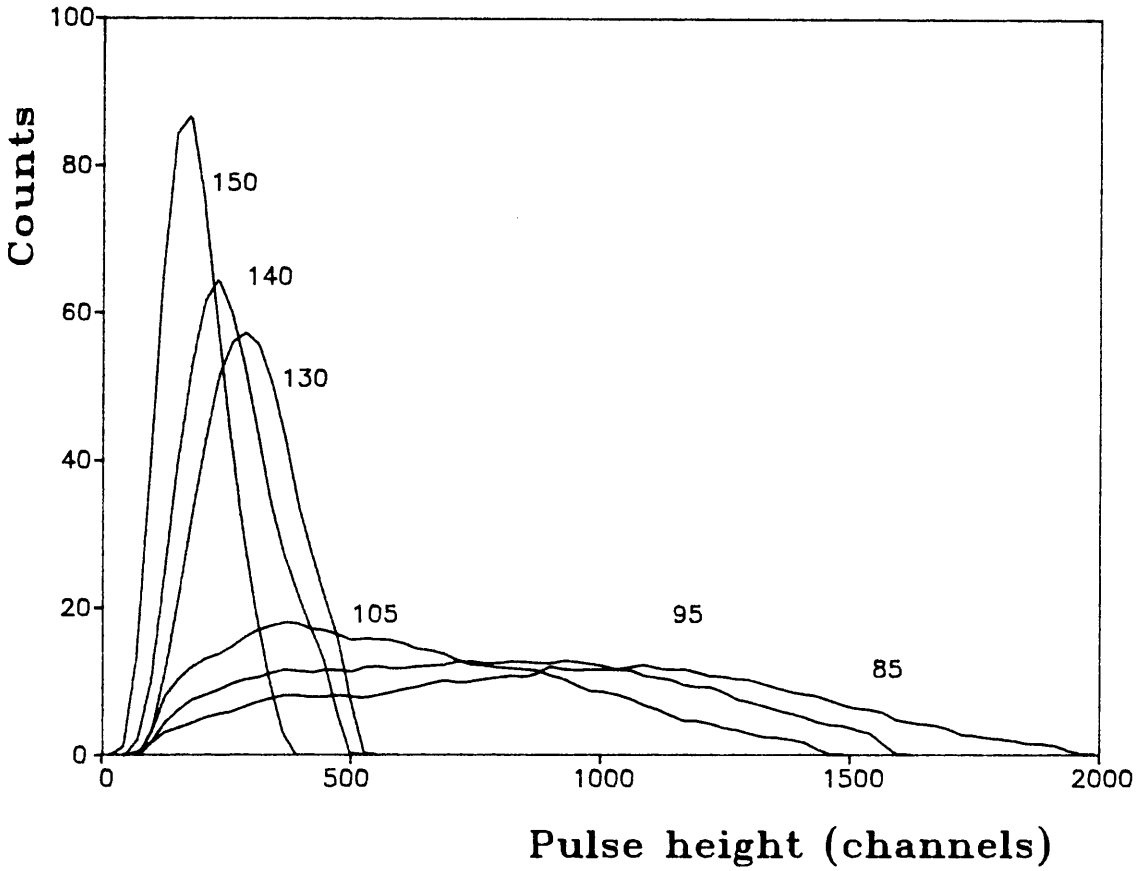

FIGURE 2.6 Pulse height distributions as a function of fragment mass for the NE810 thin film plastic scintillator used in this experiment.

Up to about 10 MeV, neutron elastic scattering from hydrogen is isotropic in the centre of mass, with the result that, for small detectors, the neutron energy spectrum N(E) is related to the measured proton recoil energy spectrum M(E) by (Pe 79)

$$N(E) = - \frac{E}{AV\sigma(E)} \frac{dM(E)}{dE} \qquad (2.6.1)$$

where A is the hydrogen number density, V is the detector volume, and $\sigma(E)$ is the (n,p) reaction cross-section at energy E, which to a first approximation is effectively constant from 1 to 10 keV and then roughly follows an $(E)^{-\frac{1}{2}}$ relationship.

In the NE213 liquid scintillator, electron induced scintillation consists principally of a fast light output component with a decay time constant of 4 ns along with a much less intense component with a decay time constant of 25 ns, whereas for a proton induced scintillation the fast 4 ns component is accompanied by a relatively slow component with decay time constant of 47 ns. Since γ-rays cause electron induced scintillation,the differing decay times could be separated by using ORTEC 270 constant fraction timing photomultiplier bases to provide pulse height and timing (CFTD) signals, and by comparing the pulse heights one is able to separate the signals due to neutrons and γ-rays. Such a procedure is generally known as pulse shape discrimination (PSD). Due to the intersection of the proton and electron distributions in the low energy region, a lower energy limit of about 0.35 MeV for neutron detection is imposed.

Figure 2.7 is a schematic diagram of the electronics used in this experiment to obtain PSD, utilizing timing-pick-off control (TPOC) units, timing single channel analyzers (TSCA) and time-to-amplitude converters (TAC), as well as amplifiers and delay amplifiers. Figure 2.8 is a plot of a typical pulse height versus PSD spectrum obtained, illustrating the clear separation of neutrons and γ-rays.

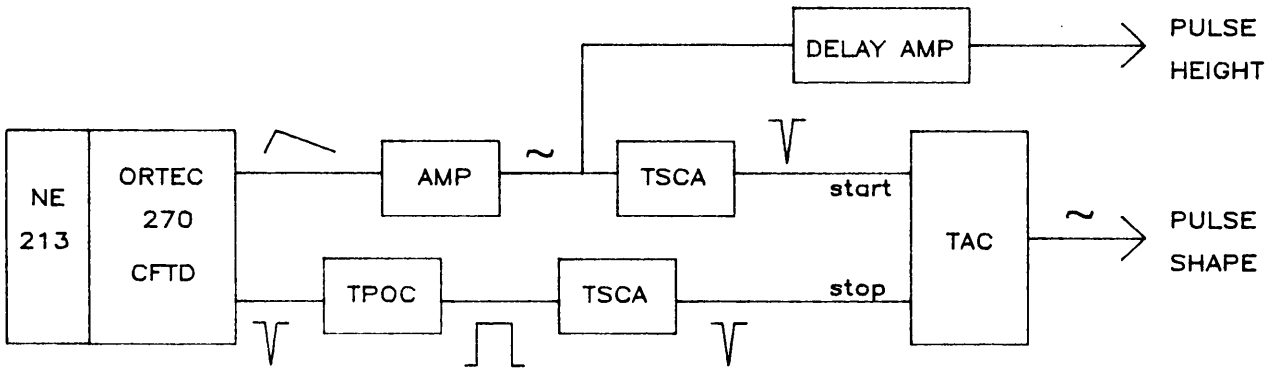

FIGURE 2.7 Block diagram of the electronics used for obtaining n/γ pulse shape discrimination.

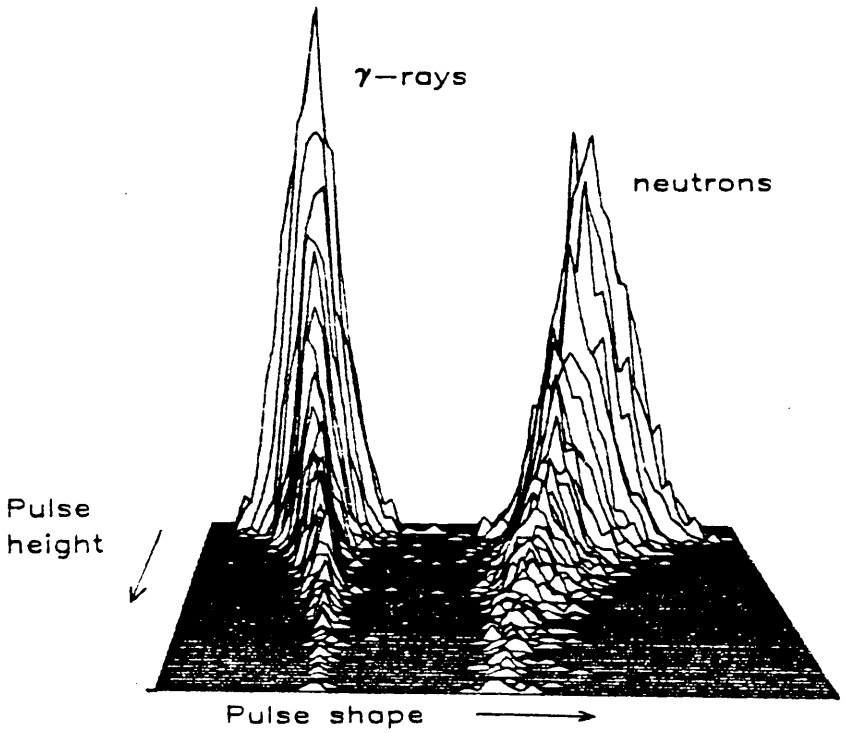

FIGURE 2.8 Pulse shape discrimination spectrum versus neutron detector pulse height, demonstrating the clear n/γ separation obtainable.

Two of the four neutron detectors used in this experiment were NE213 liquid scintillators, and the other two were NE102A plastic scintillators, for which pulse shape discrimination is not possible since there is not the same characteristic difference in decay time constants between protons and electrons.

One of the NE213 detectors was a 25 mm diameter, 25 mm long glass bubble-free unit which could be positioned in any orientation without causing the gas bubble (present for thermal expansion of the liquid) to interfere with the detector characteristics. This detector was used for detecting neutrons emitted between 0^{o} and 90^{o} to the fission axis. The other NE213 detector was a glass unit, 50 mm diameter by 25 mm long, with extended expansion chamber. The two NE102A detectors were 50 mm diameter by 25 mm long.

The neutron detectors were situated in a plane perpendicular to the incident neutron beam axis, so as to minimize any asymmetry that may have been introduced in the background component. Two detectors (one NE213 and NE102A) were positioned 46 cm and 36 cm from the target centre respectively along the fission fragment detector axis (0^{o} and 180^{o}), the bubble-free NE213 detector could be freely positioned anywhere between 0^{o} and 180^{o} and was 23 cm from the target centre, and the second NE102A detector was positioned at 90^{o}, 35 cm from the target centre. Figure 2.9 is a schematic illustration of the detector arrangement.

To determine neutron energy, time-of-flight techniques were used. The fast timing signal from the 0^{o} fragment detector provided the start pulse for timing. A dispersion in the neutron energy spectra with respect to fragment mass was formed due to the differing flight times as a function of fragment mass. This timing dispersion was up to 6 ns, which was corrected for by a procedure outlined in section 3.2.2, resulting in a timing resolution of about 2.5 ns (FWHM).

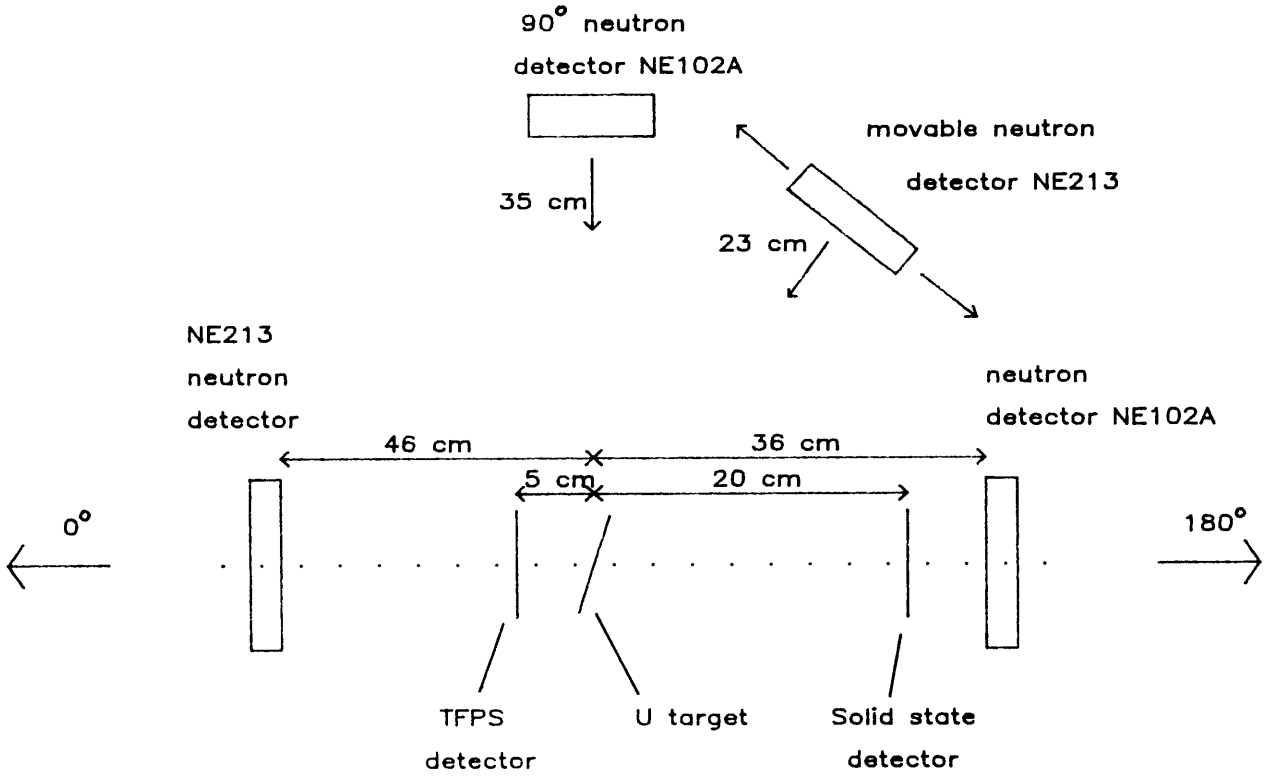

FIGURE 2.9 Schematic of the neutron detector orientation with respect to the fission axis and fragment detectors for this experiment. The movable neutron detector could be positioned anywhere between 0^{o} and 180^{o}.

2.7 Detector efficiency calibration

2.7.1 Fragment detectors

Since an asymmetric fragment detection system was used, the fragment detectors subtended different solid angles to the fission foil, giving rise to different but proportionate singles count rates. The number of fragment-fragment coincidence events in which the light fragment travels towards the 0^{o} detector was found to be the same as the rate for events in which the light fragment travels towards the 180^{o} detector. This implied that the dispersion effects of non-coplanar fragment emission and neutron recoil on the fragments was negligible.

2.7.2 Neutron detectors

The neutron detection efficiency was determined by comparing TOF neutron energy spectra with published data.

Due to the unusual arrangement of the experiment, it was necessary to calibrate the neutron detectors in situ in order to take into account absorption and scattering effects of the materials comprising the experimental arrangement. To obtain an averaged neutron energy spectrum distribution, for detector efficiency determination, a timing start pulse had to be generated that imposed no angular dependence on the spectrum being measured. This was achieved by using the timing signal from prompt γ-rays emitted at fission, which were detected in either of the NE213 detectors, which had PSD capability. It was assumed that the anisotropy of γ-ray emission with respect to neutron emission direction was negligible. This assumption was borne out by measuring the detector neutron energy distribution with respect to γ-ray timing signals from two different detector orientations, that is, for the two NE213 detectors used.

The efficiencies were determined by comparing the experimental neutron energy distributions with a Watt spectrum, see section 1.7.1. The obtained curves (see Figure 2.10) resembled the theoretical curve, with suitable application of detector bias. The theoretical efficiency distribution (Ow60) is of the form:

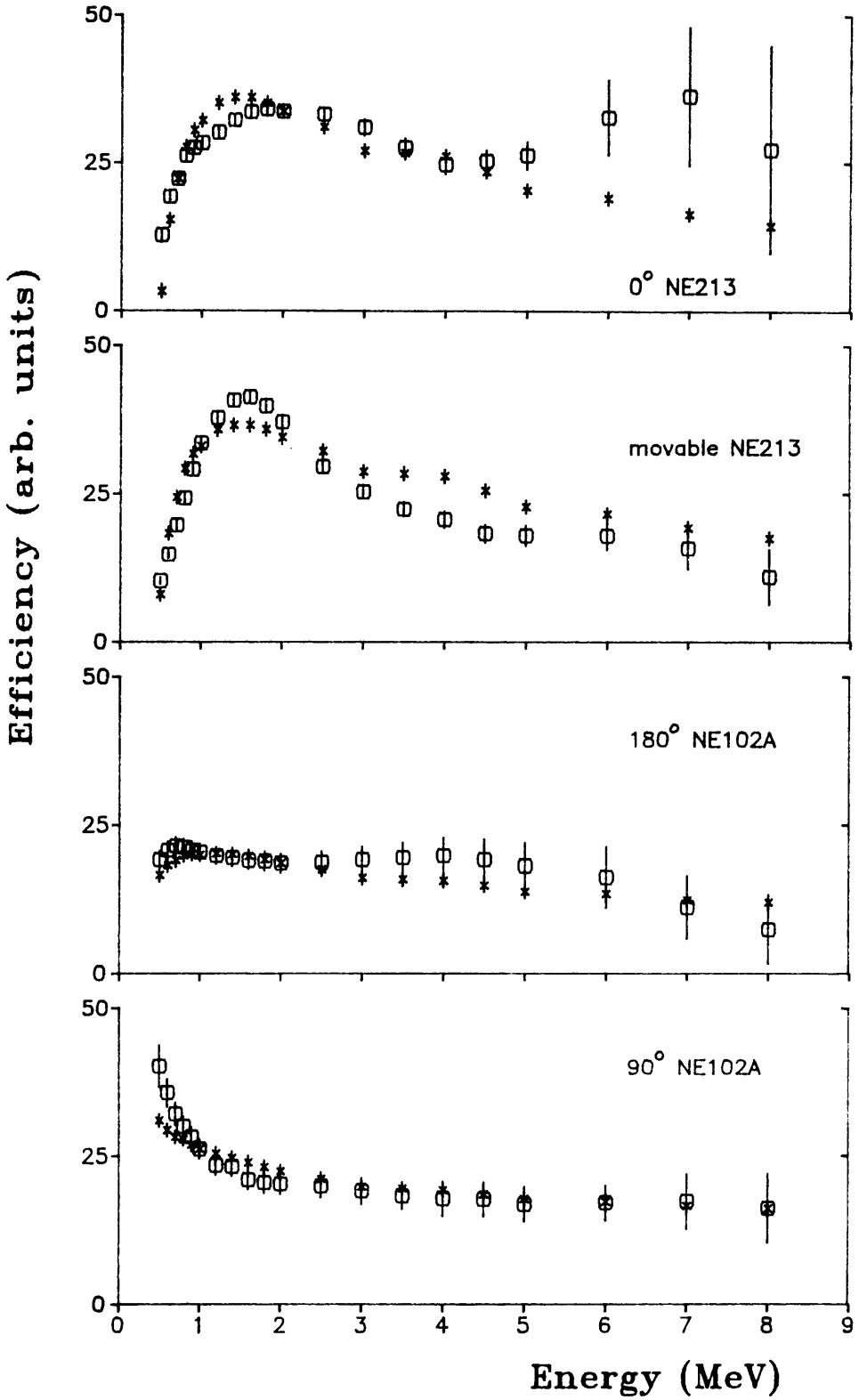

FIGURE 2.10 Measured (o) neutron detector efficiency for the four neutron detectors used, compared with values derived from equation 2.7.1 (*), with appropriate energy bias.

$$\varepsilon(E) = \frac{(E-E_b)}{E}\,(1-\exp(-n*\sigma(E)*x)) \qquad (2.7.1)$$

where E = neutron energy, E_b = detector bias, n = proton density in the scintillator ($4.6*10^{22}$ for NE213), $\sigma(E)$ = n-p scattering cross-section at neutron energy E, and x = mean detector thickness.

2.7.3 Incident beam flux

The simplest means of monitoring the incident neutron beam flux was to use the fragment detectors of the experiment. The fragment detector singles rate was directly related to the fission rate in the foil.

These measurements yielded some unexpected results, which at first were very difficult to interpret. Plotting the singles rate (averaged over three minute intervals) over each 100 hour data run and comparing the plot with information from the reactor operators led to the following conclusions concerning the constancy of the incident thermal neutron beam flux due to the restricted mode of reactor operation at 5 MW:

1) The neutron beam flux was not steady over long periods of time, due to reactor core temperature fluctuations and fuel poisoning, giving rise to variation in the neutron flux profile of the reactor core. The effect of this is seen as a gradual reduction in incident neutron flux in the first 36 hours.

2) Sharp fluctuations in flux occasionally occurred, especially prior to a reactor 'reverse', or 'scram' when the reactor would shut down.

A typical 'eventful' data run is illustrated by the fragment singles rate, plotted over a 100-hour run, in Figure 2.11.

A further anomaly observed by the neutron detectors was a variation in γ-ray background and reactor neutron flux, which sometimes displayed an increase in γ-ray background for decreasing neutron flux and vice versa. This was due to a complex combination of climatic and diurnal effects that affected both the operation of the reactor and the amount of airborne radio-activity present in the experimental environment.

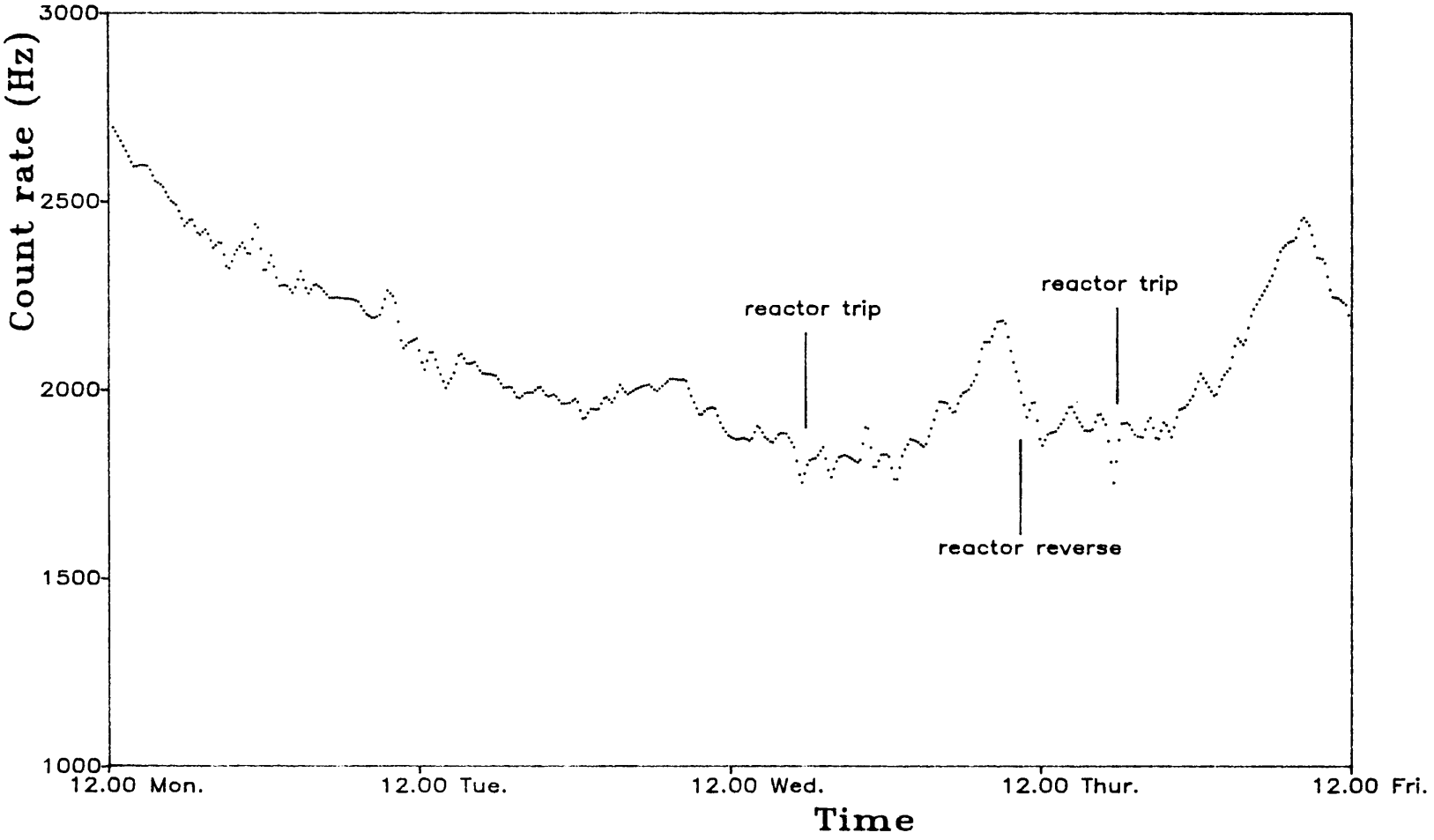

FIGURE 2.11 Fragment detector count rate recorded over a 100 hour data run. Each point is the average rate over 3 minutes

2.8 Electronics

A fission event was identified as any timing coincidence between the two fragment detectors that came within a prescribed timing window (approximately 100 ns). The 0^{o} detector was always used as the start signal for coincidence identification, since sufficient external delay had been introduced to the 180^{o} detector pulse.

The trigger logic used to identify and record a fission event is shown schematically in Figure 2.12. Having identified a fragment-fragment coincidence, this trigger was used to gate the 0^{o} timing signals so that a 'true' start signal was formed. This signal was then used as the common start to an octal time-to-digital converter (TDC) for time-of-flight (TOF) data acquisition and strobe for an octal analog-to-digital converter (ADC) for pulse height acquisition.

The single width CAMAC octal TDC contained eight analysing channels that were coupled to a common start input for measuring time intervals over a range of 0 to 200 ns with a resolution of 100 ps. If no stop pulse arrived within 200 ns an internal timer simulated a stop and the output value was overrange and ignored. The single width CAMAC octal ADC contained eight peak-measuring analysing channels measuring positive unipolar or bipolar signals in the range 0 to 2 V with 1 mV resolution.

Figure 2.13 is a block diagram of the electronics used for the neutron-fragment TOF measurements, as well as the PSD spectra for the two liquid scintillation detectors. Either timing single channel analyzers or gate and delay generators were used to bring all the detector signals (T) within the prescribed timing window of the octal TDC. Delay amplifiers were used to bring analog signals (L) within the strobe window of the octal ADC.

The singles counts (S) for each detector were recorded using two CAMAC single width presettable quad-scalers with a range of 24 bits per scaler.

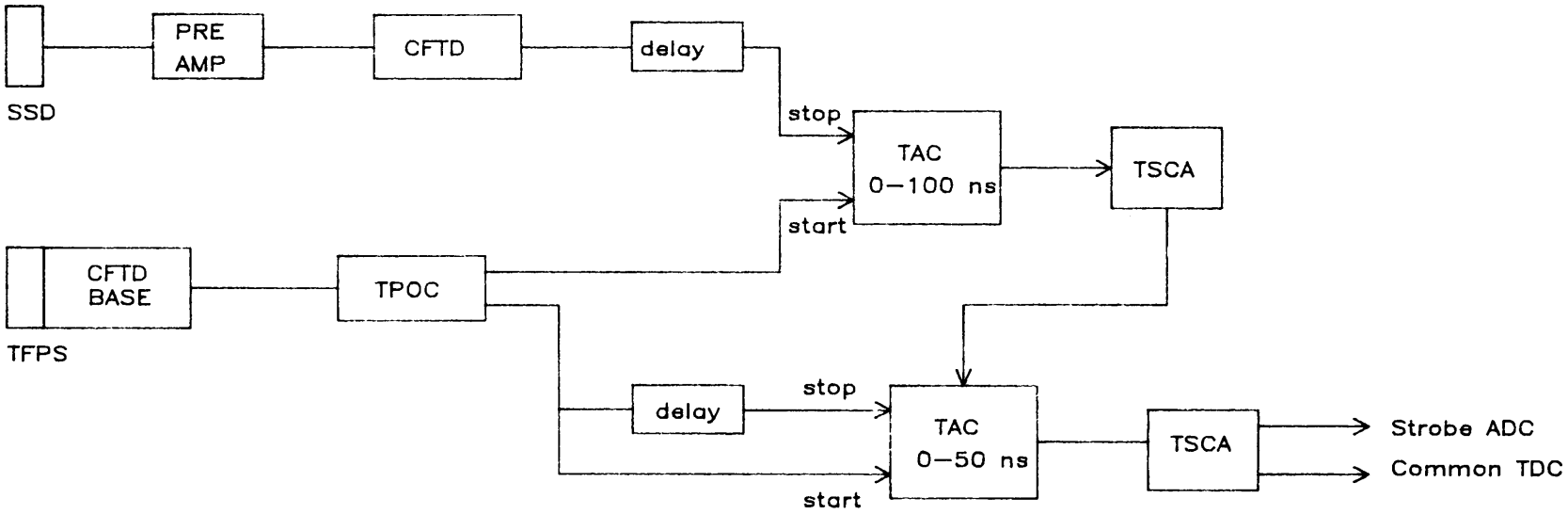

FIGURE 2.12 Block diagram of the electronics to identify a fragment-fragment coincidence and provide a timing signal for time-of-flight measurements (common start for TDC) and strobe for the octal ADC.

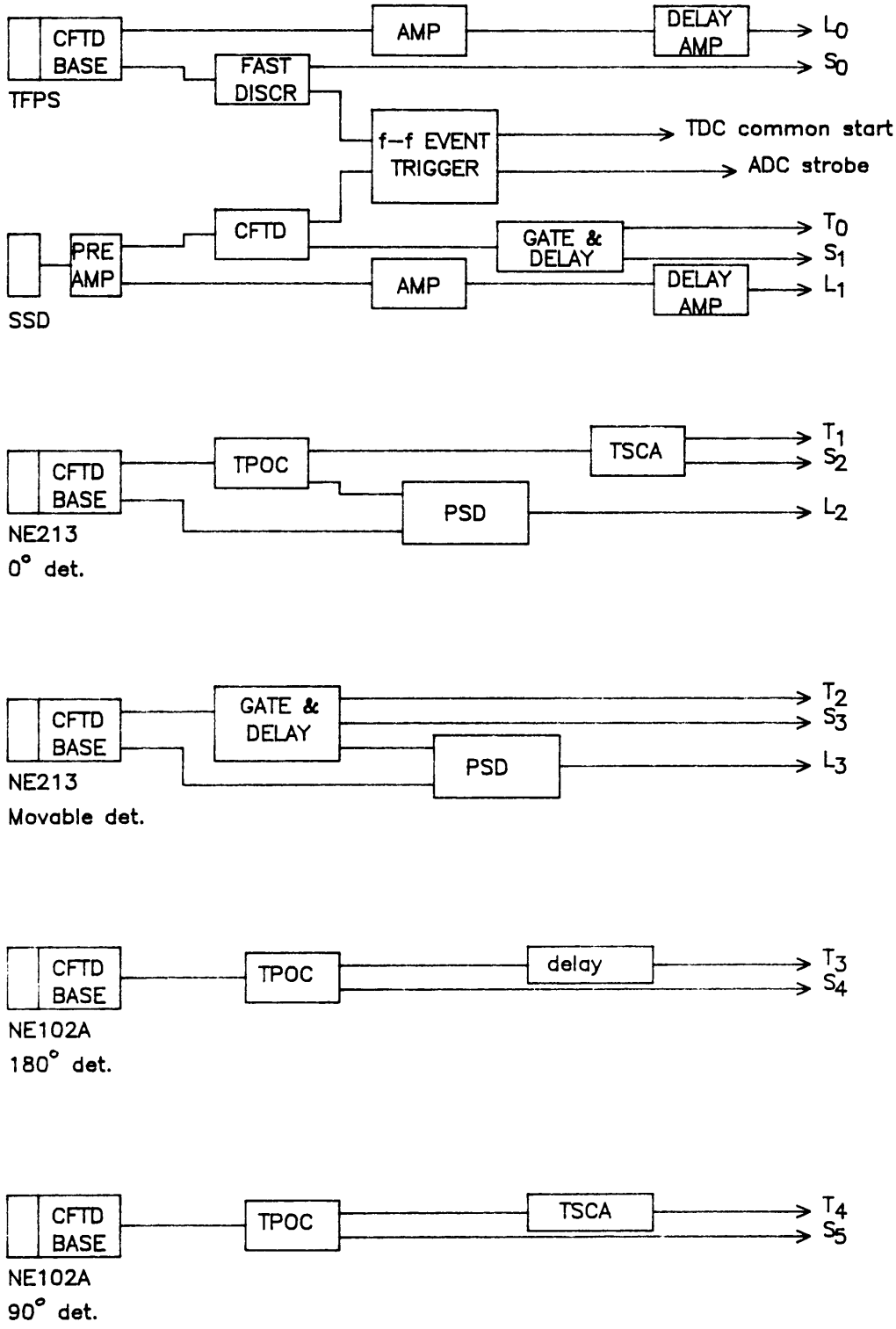

FIGURE 2.13 Block diagram of the electronics for fragment-neutron/γ-ray coincidence measurements of time-of-flight (T), pulse height and pulse shape (L) and singles rates (S).

The CAMAC logic is shown in Figure 2.14. The ADC and TDC unit had an effective dead time of 90 μs, during which time an innibit signal was imposed on the TDC, ADC and scalers. The inhibit signal was generated by the CAMAC LAM (Look At Me) set by the ADC, the LAM also being the signal to the computer that the units were ready for interrogation.

2.9 Data acquisition

The experiment was on-line to a Hewlett-Packard M-series mini computer with 384 kbytes of memory and 16 bit word length. Logic control of the experiment was from the computer via CAMAC.

The fission event trigger rate was about 30 per second. Upon receipt of an event trigger (CAMAC LAM) the contents of five channels of the octal TDC, four channels of the ADC and six channels of the quad-scalers were read into computer memory. The information contained in the TDC and ADC were checked to identify candidate fragment-fragment-neutron (f-f-n) coincidence events which fell within prescribed windows. If successful, the information was recorded along with the computer clock time, with a resolution of 10 ms, on disc. Preliminary on-line analysis of the data could be performed during the experiment to monitor detector performance. Figure 2.15 is a flow chart of event identification used by the computer. The data on disc was transferred, at the end of each data run, to magnetic tape for permanent storage and later off-line analysis.

In a typical data run lasting about 100 hours, the average continuous operating time of the reactor, approximately 30 000 fission (f-f-n/γ) events were recorded, the number being dependent on the relative positions of the neutron detectors.

A series of data runs (series A) were made using two TFPS as fragment detectors. The electronics used was similar to that used in the second series (B) (using one TFPS and one SSD), except that a TDC was not available so time-to-amplitude converters (TAC) were used for TOF information, these signals being recorded by the octal ADC. A schematic of the electronics for this experiment is shown in Figure 2.16. Due to insufficient electronics PSD spectra could not be included.

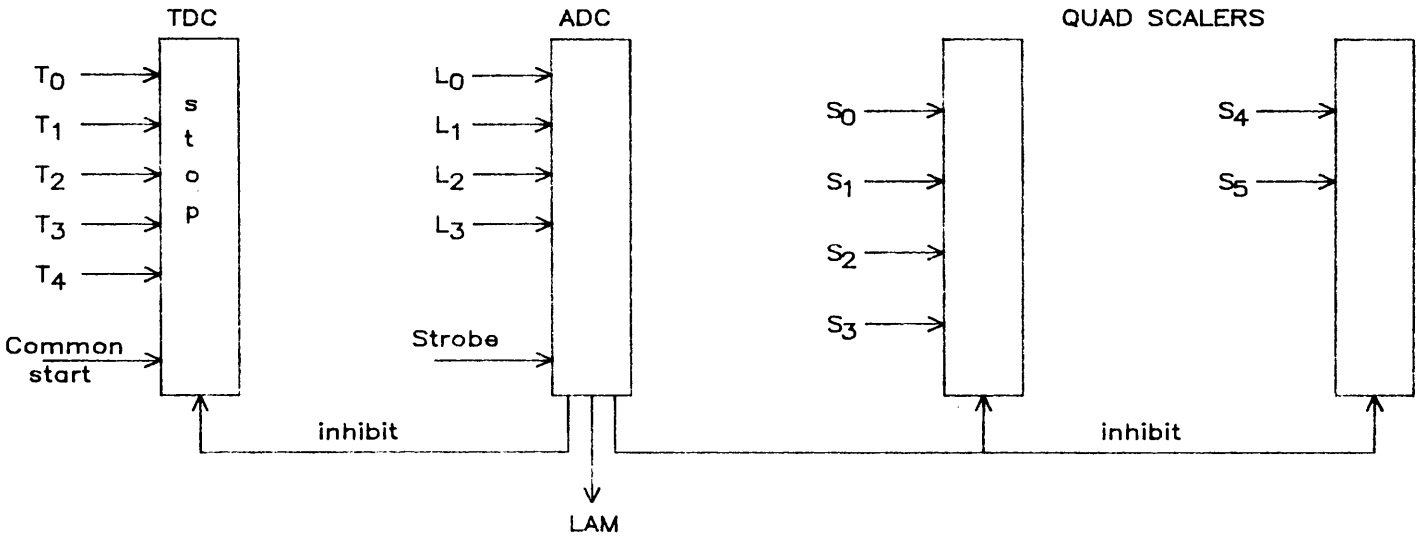

FIGURE 2.14 Block diagram of the CAMAC logic for the octal TDC, octal ADC and two quad-scalers. The ADC provided an inhibit signal to all the units whilst it was busy and unable to convert input signals.

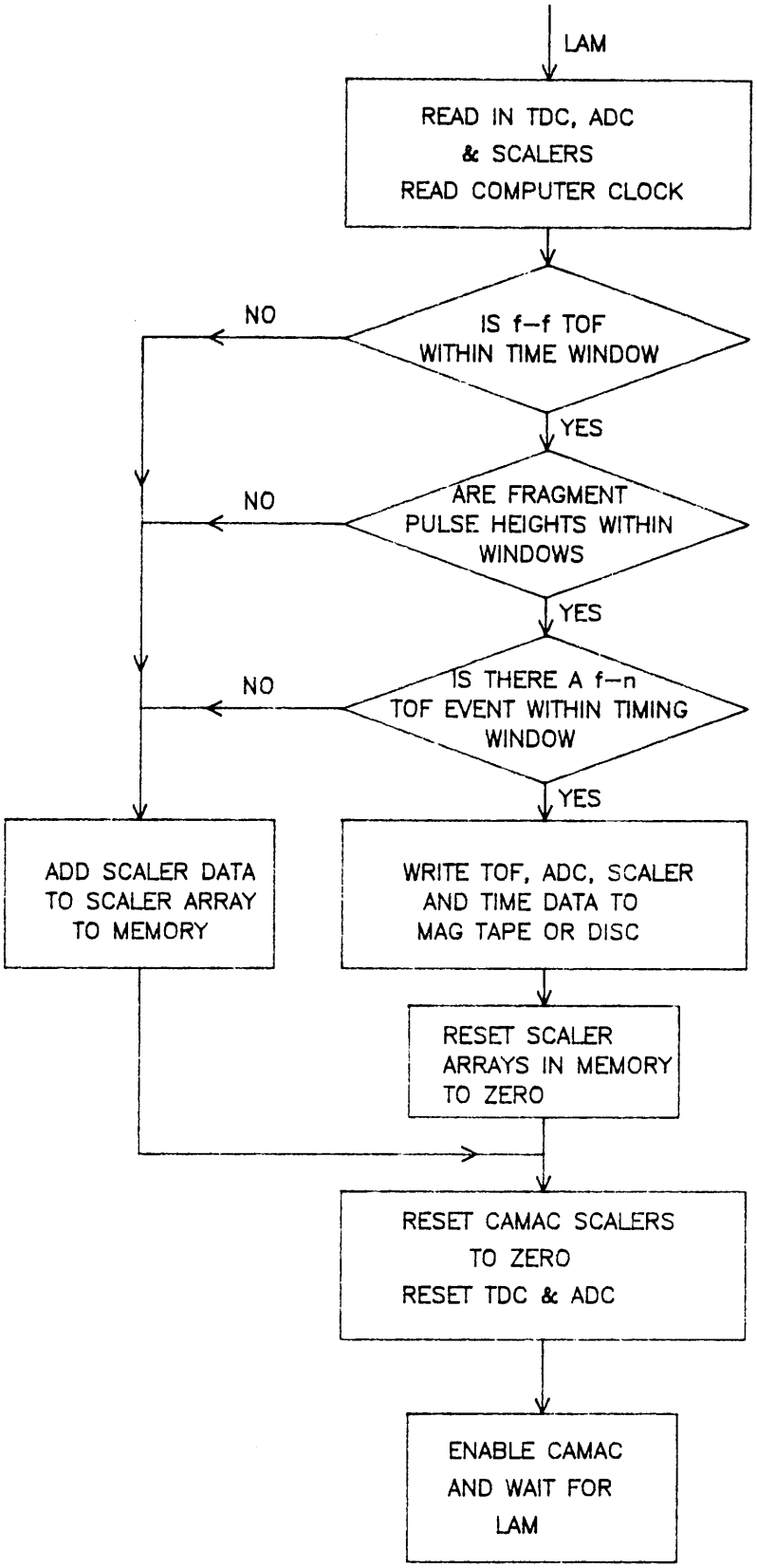

FIGURE 2.15 Flow chart for fragment-fragment-n/γ event identification by the computer during the experiment.

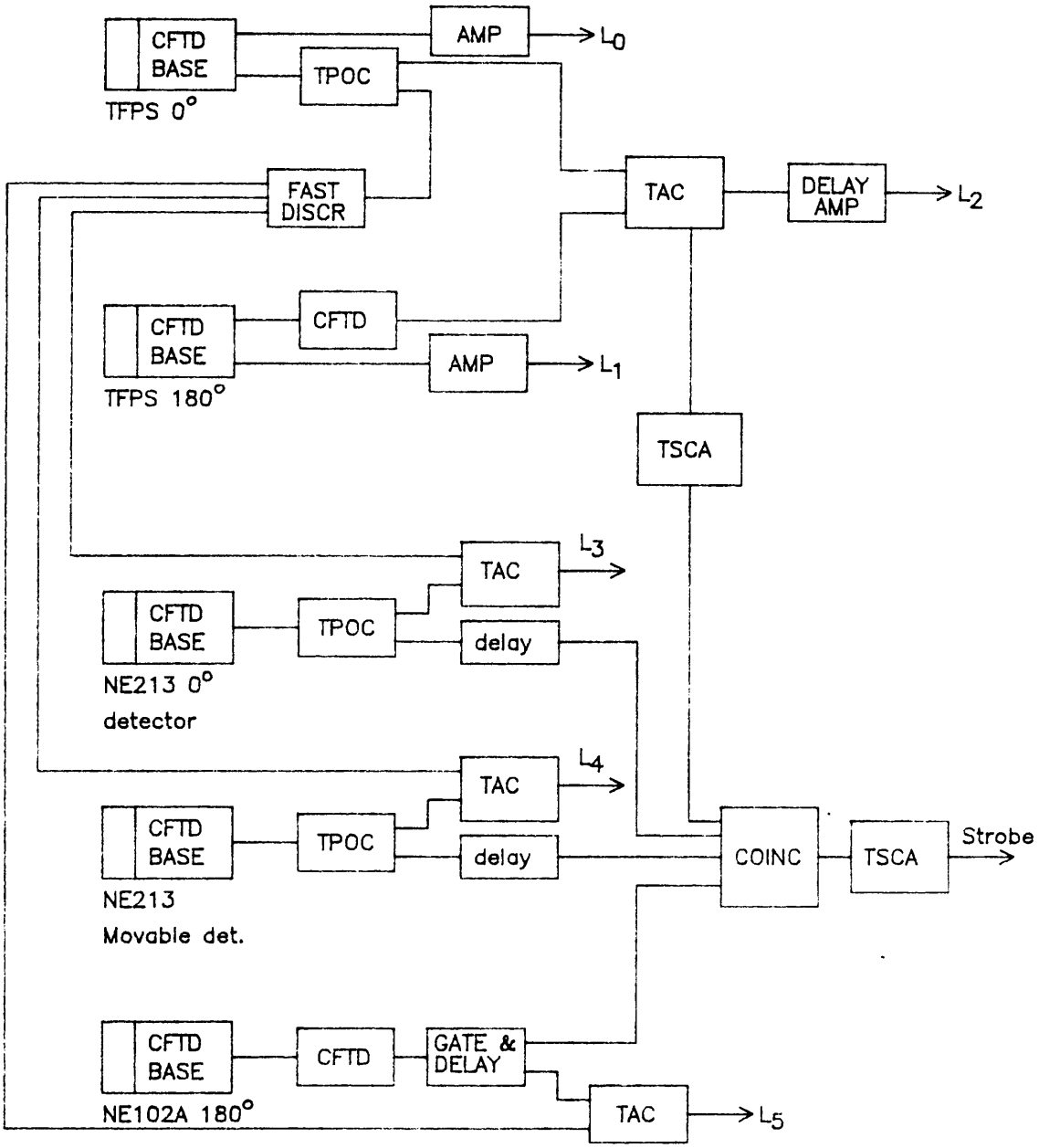

FIGURE 2.16 Block diagram of the electronics to identify fragment-fragment-n/γ events for series A experiment using two NE810 thin film plastic scintillator detectors.

The experiment was run for a period of four months for series A and seven months for series B. Neutron fragment angular correlations were measured with the moving neutron detector at 30^{o}, 45^{o}, 60^{o}, 75^{o}, 90^{o}, 120^{o}, 135^{o}, 150^{o} and 180^{o} to the 0^{o} detector. For normalization purposes data was also taken with the moving detector at 0^{o}.

For series A approximately 8 000 f-f-n/γ events were recorded at 30^{o}, 60^{o}, 90^{o}, 120^{o} and 150^{o}, and 48 000 and 29 000 events at 0^{o} and 180^{o} respectively. For series B approximately 15 000 f-f-n/γ events were recorded for each moving neutron detector position and 54 000, 144 000 and 100 000 events at 0^{o}, 180^{o} and 90^{o} respectively.

3 DATA REDUCTION AND ANALYSIS

3.1 Introduction

The raw data written to magnetic tape contained coincidence events that fell within broad acceptance windows. For the two data series, A and B, the number of events recorded was 200 000 and 500 000, respectively, for all neutron detector configurations. Application of more precise windows on the TOF and PSD (where applicable) spectra enabled data sets to be produced on magnetic tape for more detailed further analysis. This reduced the total number of events, since each event stored on the data set tape (DST) was known to be a reasonably good candidate as either a f-f-n or f-f-γ coincidence event. For cut studies a further compressed DST was made for each data series onto which only the TOF, PSD and pulse height data were stored to facilitate in rapid scanning of the whole data.

It should be noted that since this was a triple coincidence experiment, fission events in which only the fragments were detected were not recorded. The advantage of this was a considerable saving in data storage space, since the f-f-n coincidence rate was a factor of 400 down on the f-f coincidence rate.

3.2 Cut Studies

Obtaining neutron-fragment angular correlations as a function of fragment mass and neutron energy required detailed analysis of the data in the form of cuts being applied to the various spectra recorded. The cut studies were divided into three main areas:

1) Fragment-mass separation

2) Neutron-γ-ray separation

3) Neutron energy normalization

Since the series A data did not contain PSD information, this data was used more specifically for fragment mass separation analysis.

3.2.1 Mass separation

A convention is defined here for fission events in which light fragments travelling towards the 0^{o} detector are referred to as LH events, and heavy fragments travelling towards the 0^{o} detector are referred to as HL events.

Due to unavoidable dispersion effects to the fragment TOF data (see section 2.4), a fragment-mass resolution of approximately 10 amu was achieved. To obtain such a resolution in mass separation the following procedure was used to generate acceptance windows, for specific fragment mass division regions, on single and two-parameter spectra obtained from fragment detector pulse heights and f-f TOF difference distributions.

For a specified fragment-mass division one has a f-f TOF difference of $T \pm \Delta T$, where ΔT is the dispersion in T attributable to such a fragment mass division (see Figure 3.1) (ΔT being made up of two components, kinematic and experimental effects). Applying the $T \pm \Delta T$ window to the integral two-parameter plots, containing all data, of f-f TOF difference versus fragment detector pulse heights (0^{o} and 180^{o} detector) resulted in acceptance zones being formed for both the two parameter plots. An example is given in Figure 3.2 for mass 95 in the LH and HL regions. The resultant pulse height windows also generated an acceptance zone in the two-parameter coincident fragment detector pulse height distribution. Application of these acceptance zones to the data created tighter windows for the single parameter spectra (f-f TOF, pulse height (0^{o}) and pulse height (180^{o})). These single-parameter cuts enabled event-for-event analysis of the data to be performed rapidly by identifying candidate n-f events falling within the mass division region being analyzed.

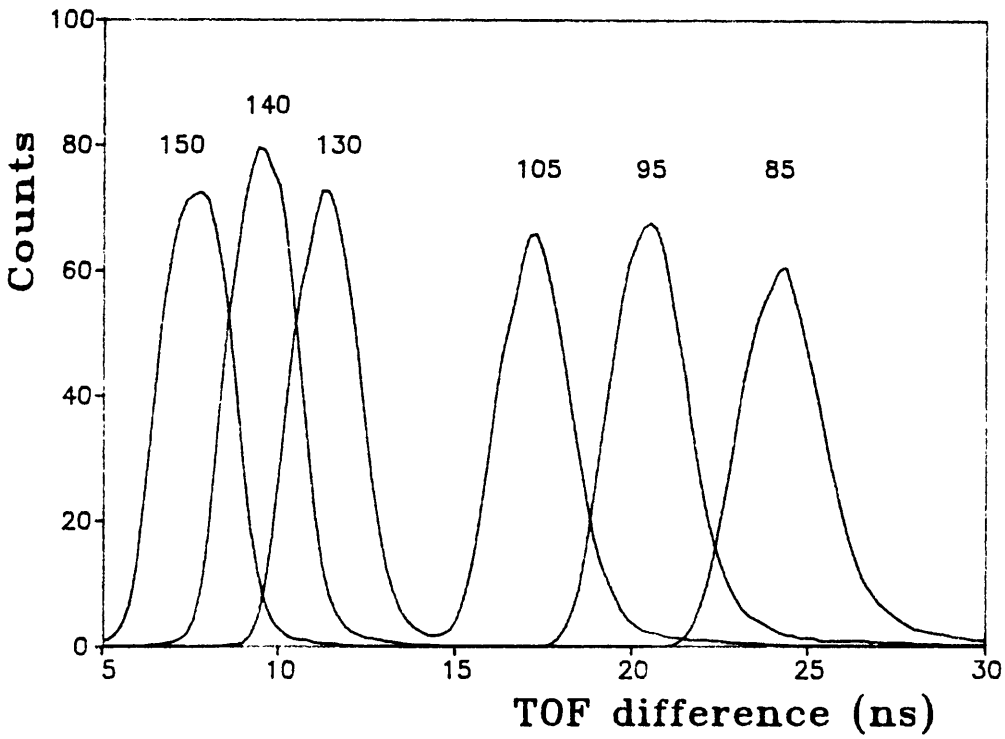

FIGURE 3.1 Calculated fragment-fragment time-of-flight difference for specific fragment mass divisions for fragments emitted from an inhomogeneous target foil, average thickness 1 mg cm^{-2}.

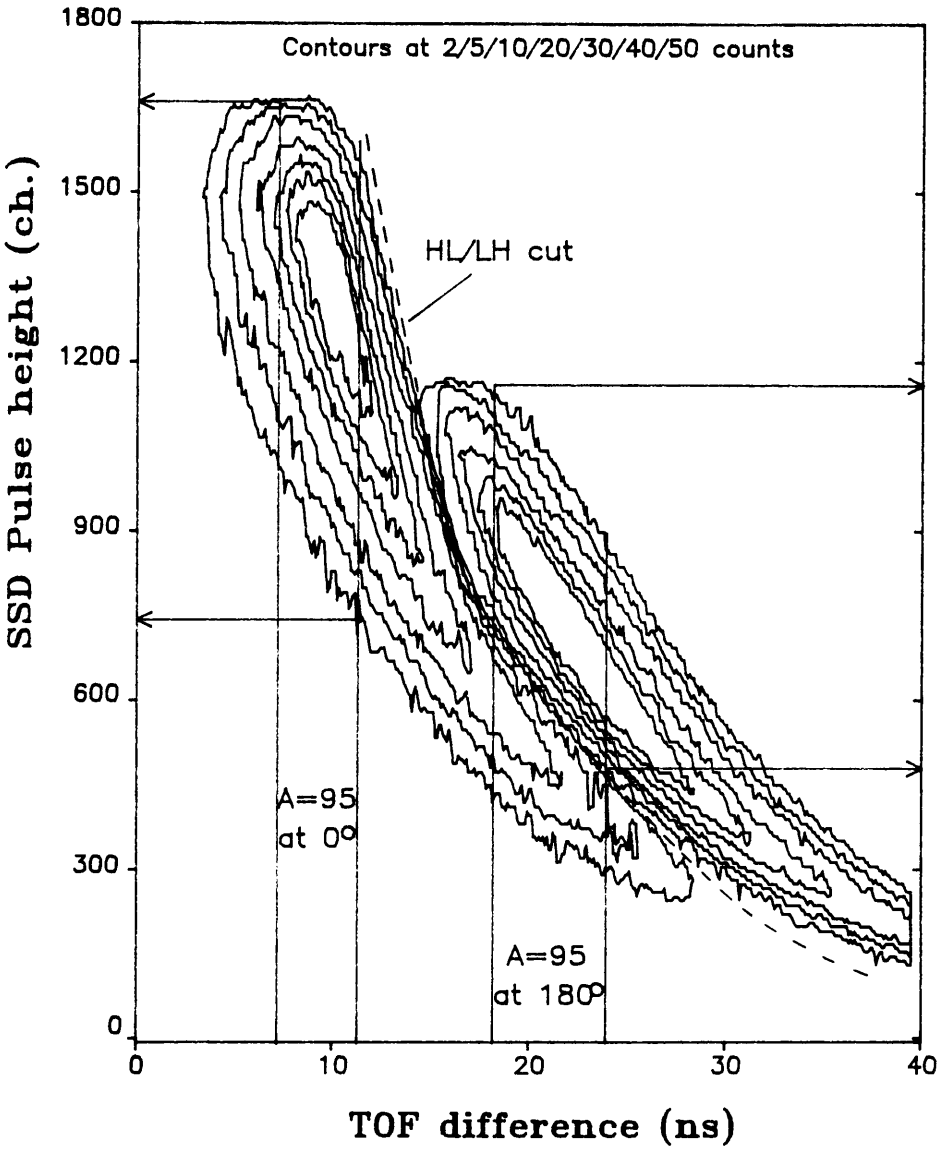

FIGURE 3.2 Measured fragment-fragment time-of-flight difference with respect to the 180^{o} solid state fragment detector pulse height. The pulse height cuts applicable for identifying a fragment mass division 95/141 are indicated.

Figure 3.3 illustrates the uncut integral pulse height distribution obtained in the TFPS and SSD detectors, compared with published data for unstraggled fission fragments (Aj82, Go84). Plotting the coincident fragment detector pulse heights against each other (Figure 3.4), illustrates a) the mass separation into two regions associated with detection of a LH or HL event, and b) the area of overlap, that is, low pulse height in both detectors, which was due to the effect of straggling of the fission fragments in the target foil. Most of the f-f coincidence events falling within the latter region were resolved into LH or HL events by careful analysis of the two-parameter f-f TOF versus pulse height spectra, and by creating tighter acceptance zones for such events.

Applying the acceptance zones for each two parameter distribution with respect to three light-fragment mass-division regions, corresponding to mass regions 80-90, 90-100 and 100-110, six data sets (3 for LH and 3 for HL events) were produced for n-f angular correlation analysis.

3.2.2 Fragment-neutron, fragment-γ-ray separation

Figures 3.5 and 3.6 are two representations of the f-f TOF difference versus fragment-neutron (orγ-ray) TOF difference (f-n/γ). Since the γ-ray has a fixed TOF, the TOF difference between fragment and γ-ray was a direct indication of the fragment velocity, as is more clearly illustrated in Figure 3.5, which for unstraggled fission fragments is directly related to the fragment mass. Within the resolution of these plots it was noted that the cuts applied to obtain data in the desired mass division regions were justified.

Figure 3.7 is a typical plot of the f-n/γ TOF difference as measured in one of the neutron detectors. The neutron-γ-ray overlap was due to the variation in the timing start signal of the different fission fragment masses.

Applying appropriate cuts to the f-f TOF versus f-n/γ TOF (Figure 3.5), f-n/γ TOF versus PSD (see Figure 3.8), and f-n/γ TOF versus fragment detector pulse height (see Figure 3.9) clean separation of the neutrons and γ-rays was obtained.

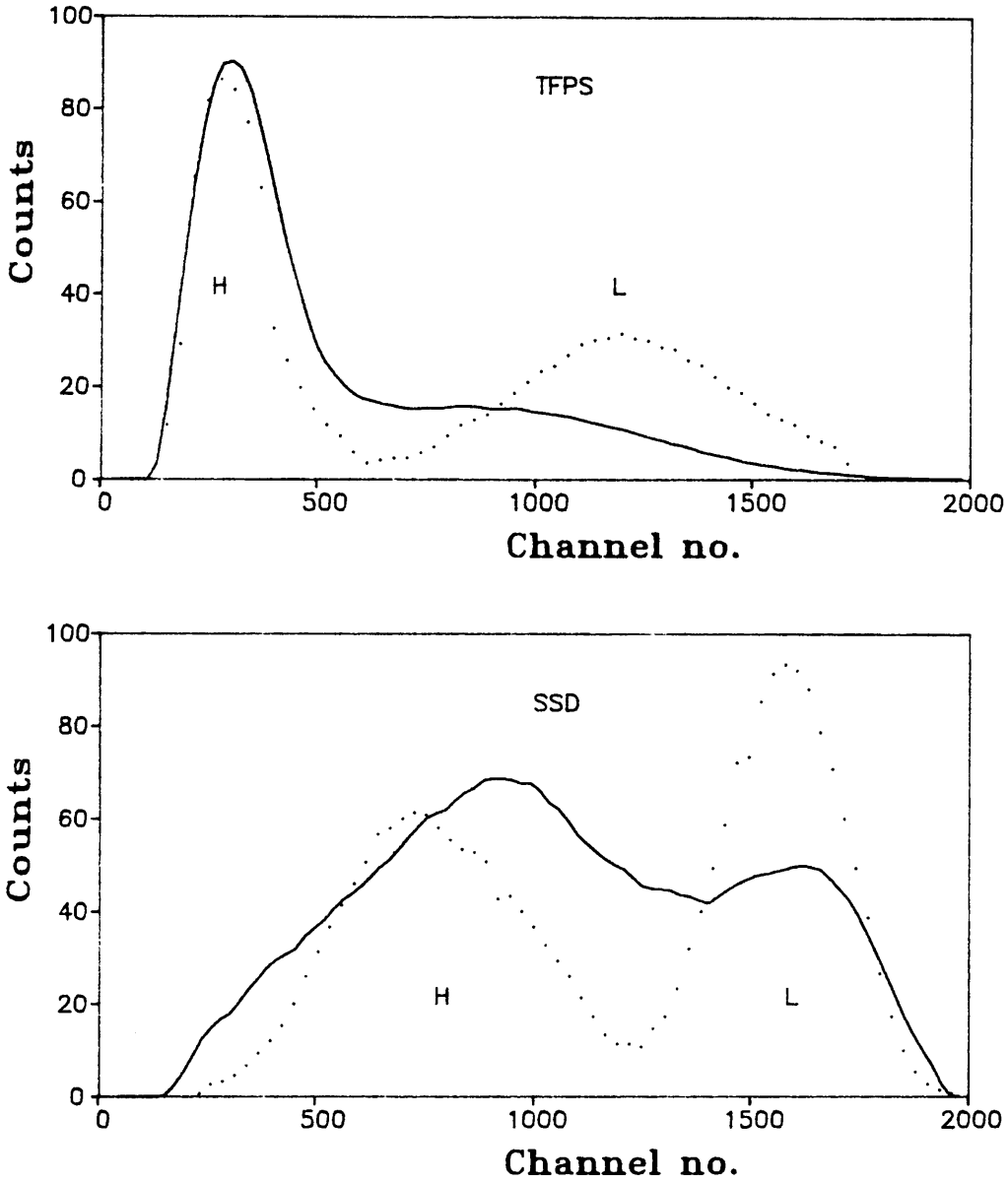

FIGURE 3.3 Measured fission fragment pulse height distribution for TFPS and SSD (-) compared with published data (...) (Ref.Aj82, Go84) for unstraggled fission fragments. The light (L) and heavy (H) fragment mass regions are indicated for the two detectors.

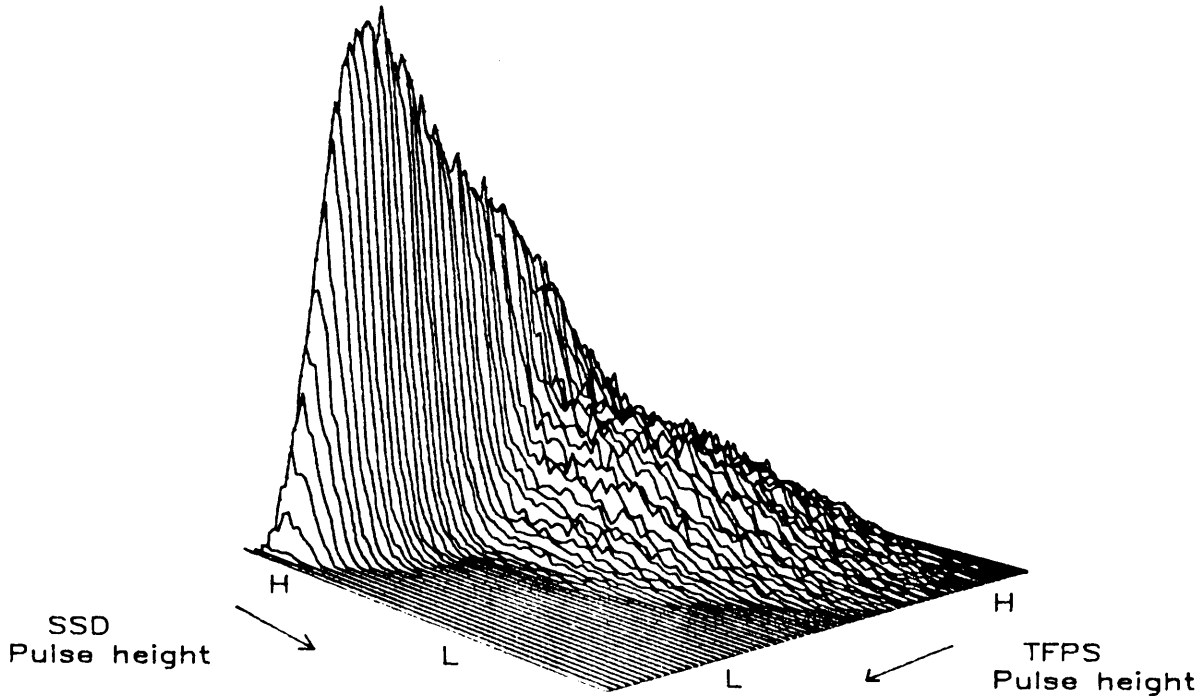

FIGURE 3.4 TFPS versus SSD pulse height distribution for coincident fission fragments. L and H refer to the detected light and heavy fragments respectively.

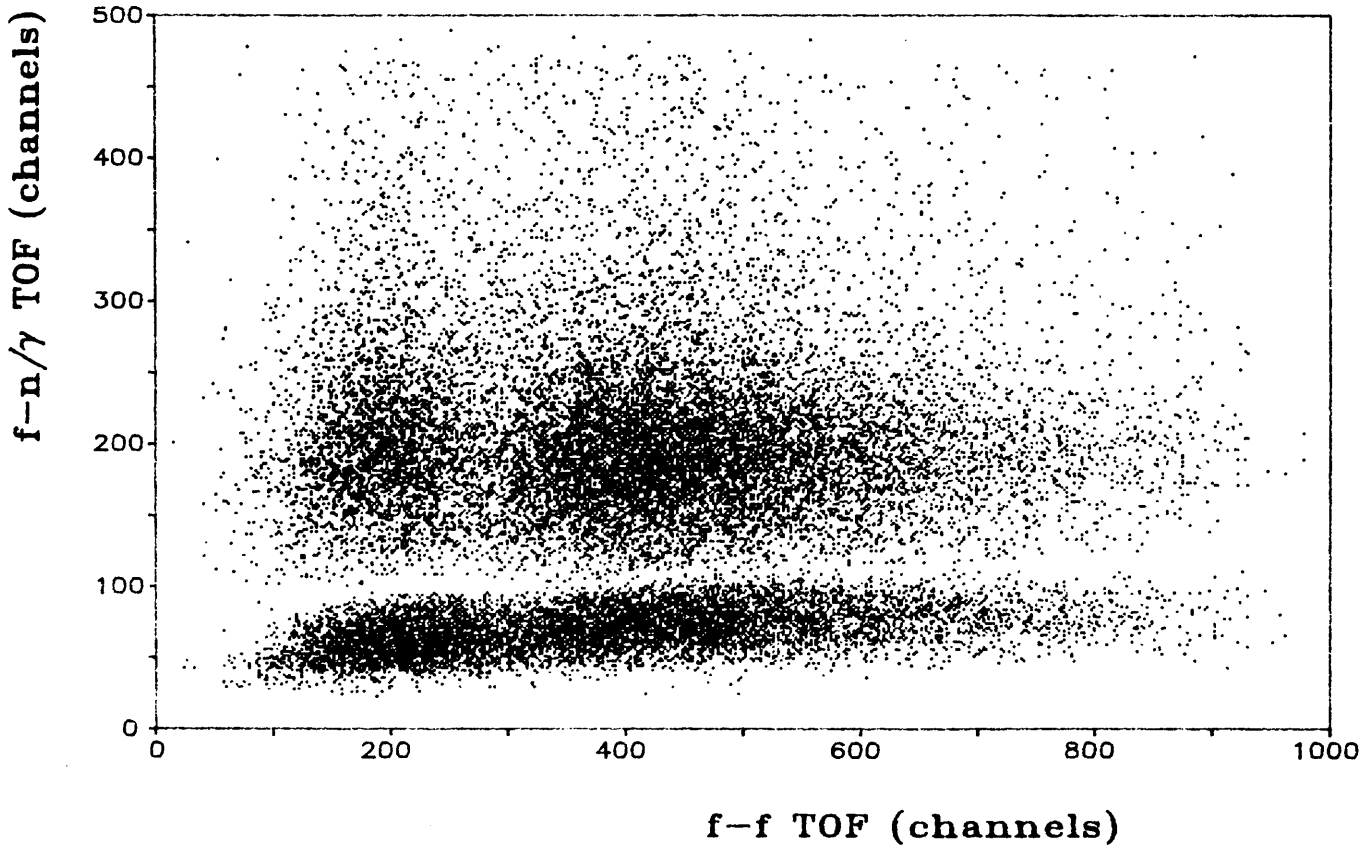

FIGURE 3.5 Scatter plot of fragment-fragment time-of-flight versus fragment-n/γ time-of- flight of the 0^{o} neutron detector. An asymmetry is clearly seen between the number of neutrons corresponding to the light or heavy fragments arriving at the 0^{o} fragment detector. The slope of the γ-ray distribution reflects the TOF difference of light and heavy fragments arriving at the 0^{o} fragment detector.

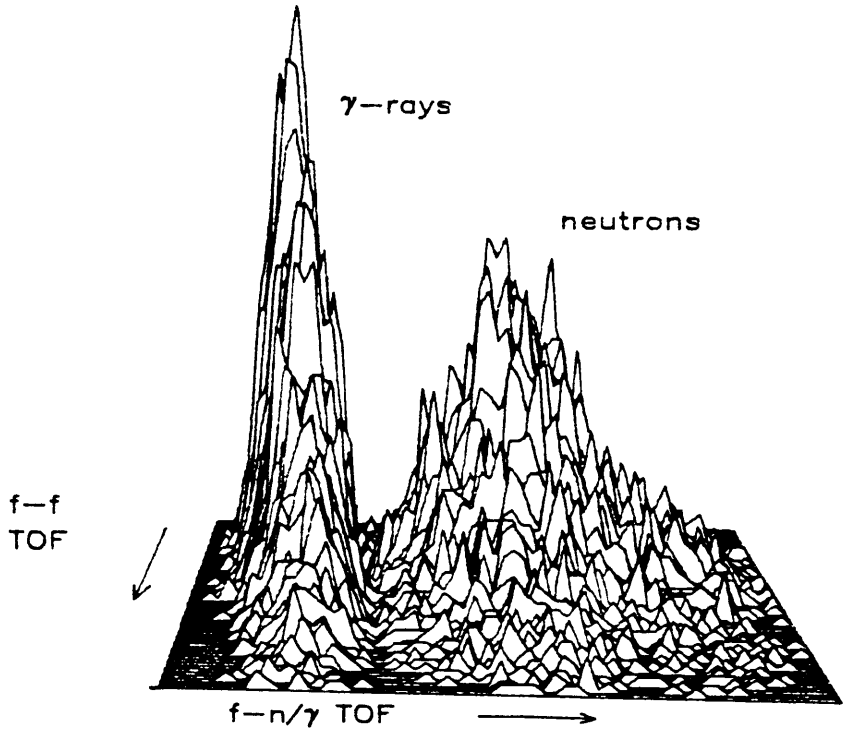

FIGURE 3.6 Measured fragment-fragment TOF difference versus fragment-n/γ TOF between a fragment seen at 0^{o} and a neutron or γ-ray in the 0^{o} neutron detector.

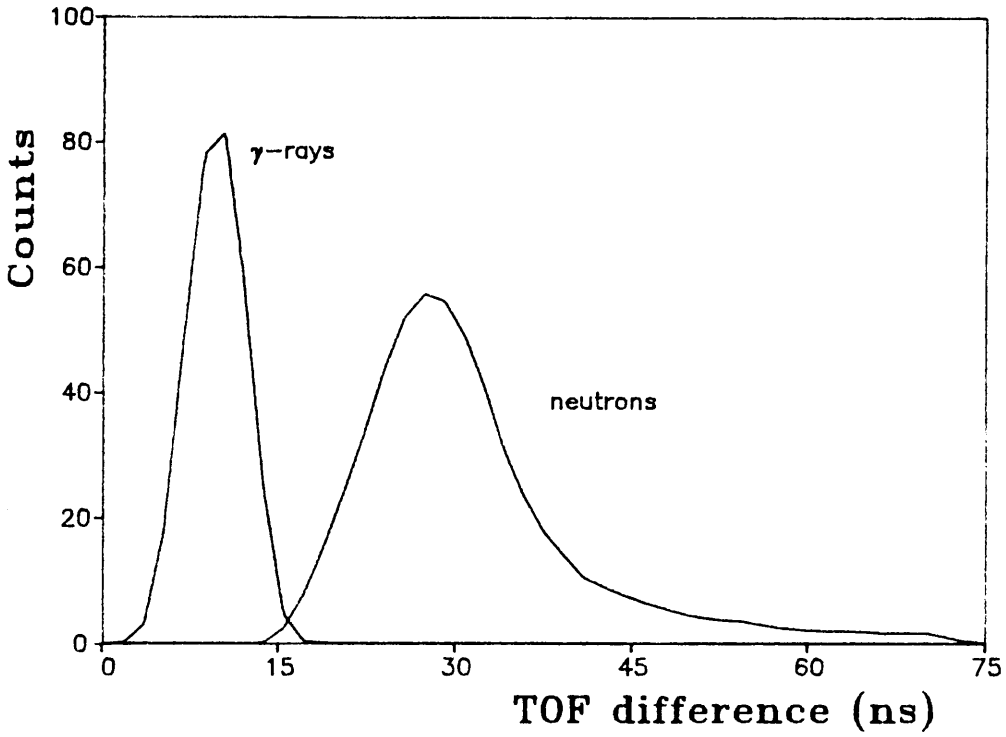

FIGURE 3.7 Typical integral fragment-neutron/γ TOF difference distribution.

An important feature observed in the plot of f-n/γ TOF versus PSD (Figure 3.8) was that the background component lies predominantly in the γ-ray region, that is, it is fair to assume a virtually zero background component in the neutron spectrum after application of pulse shape discrimination (see Figure 3.11).

3.3 Coincidence event selection

Depending on the acceptance zones and windows applied in an event by event analysis of the data, the following data sets were then produced:

1) f-f-n coincidences as a function of light fragment direction for all observed neutron energies

2) f-f-n coincidences as a function of light fragment direction and neutron energy

3) f-f-n coincidences as a function of fragment mass in 10 amu steps for all neutron energies

4) f-f-n coincidences as a function of fragment mass in 10 amu steps and neutron energy

3.4 Corrections to the data

Using the information obtained from f-n/γ TOF versus fragment pulse height, and versus PSD (Figures 3.8 and 3.9), a correction to the TOF data, taking into account the variation in fragment velocity as a function of fragment mass (which defined a timing start pulse), could be made. The effect of this correction is illustrated for the f-γ TOF distribution in Figure 3.10, the peaks corresponding to HL and LH events. Due to the dispersion in fragment velocity for a given mass, the FWHM of the corrected f-γ-ray spectrum was 5.0 ns, compared with a detector calibration width of 2.5 ns. The γ-ray peak in each channel of the f-n/γ TOF spectrum was taken as the time equals zero point for neutron energy determination as a function of fragment TOF difference (mass division).

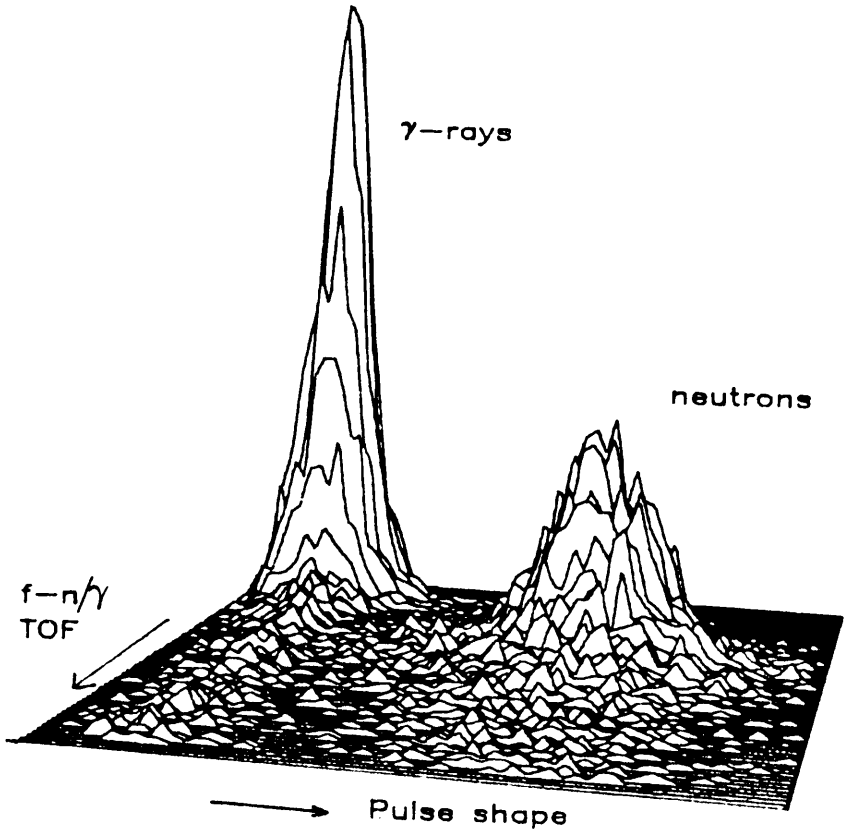

FIGURE 3.8 Fragment-n/γ TOF difference versus PSD spectrum. Note the ridge in the γ-ray region over the full range of the TOF distribution due to background.

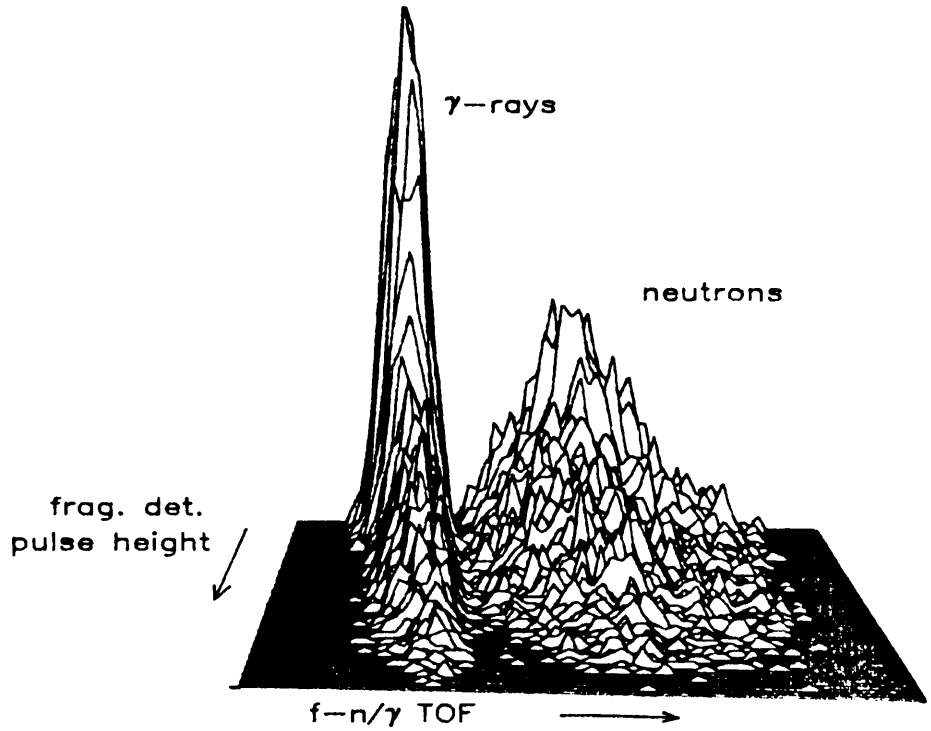

FIGURE 3.9 Fragment-neutron/γ TOF difference versus 0^{o} fragment detector pulse height.

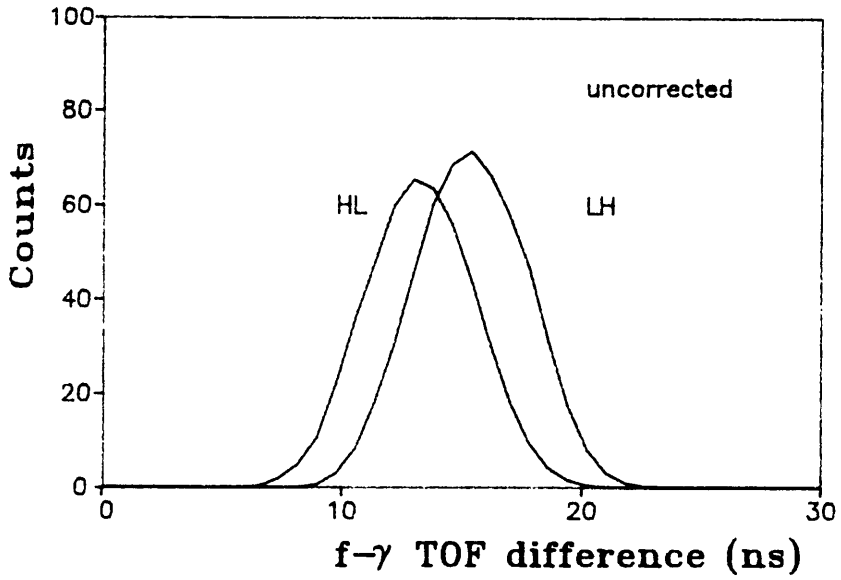

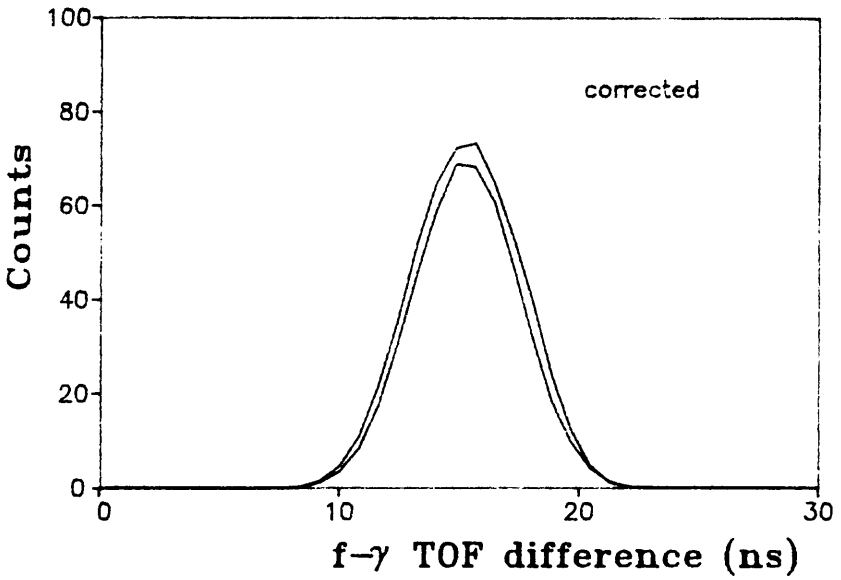

FIGURE 3.10 γ-ray TOF spectrum before and after correcting for the differing fragment start times, that are evident in Figure 3.5 and 3.9.

The constraints on the data due to the multi-parameter cuts were such that the background contribution was reduced to less than 1% of the data. Figure 3.11 is a comparison of a typical neutron TOF distribution with and without a PSD cut but with all other cuts applied, illustrating the very clean neutron spectrum obtained. It was decided therefore not to consider background subtraction to those detectors using PSD. In the case of the neutron detectors for which PSD could not be done, comparison of the TOF spectra with PSD cut spectra provided an estimate of the background ratio on a channel-by-channel basis (the comparison being done for equivalent fragment-neutron detector orientation). Due to significant differences in the data acquisition characteristics of the two run series and the fact that no PSD data were available in series A, this data was not included for final n-f angular correlation analysis.

The detector efficiency curves took into account the neutron absorption effects of the material present between the fission source and the detector. In the case of the rotating detector it was assumed that the neutron absorption and scattering effects at different angles to the fission axis were uniform as a function of neutron energy. Thus the mean singles rate at each detector angular position was used to normalize the data to the value measured with the moving detector at 0^{o}.

The distributions obtained for the different detectors and angular bins were normalized to one another taking into account the data accumulation time. Finally, the angular distribution data were normalized with respect to the 90^{o} data set to unity.

Using the appropriate neutron detector efficiency curves (Figure 2.10), the TOF distributions were converted to neutron energy distributions in 0.1 MeV bins from 0.5 MeV to 3.0 Mev and in 0.5 MeV bins from 3.0 to 10.0 MeV.

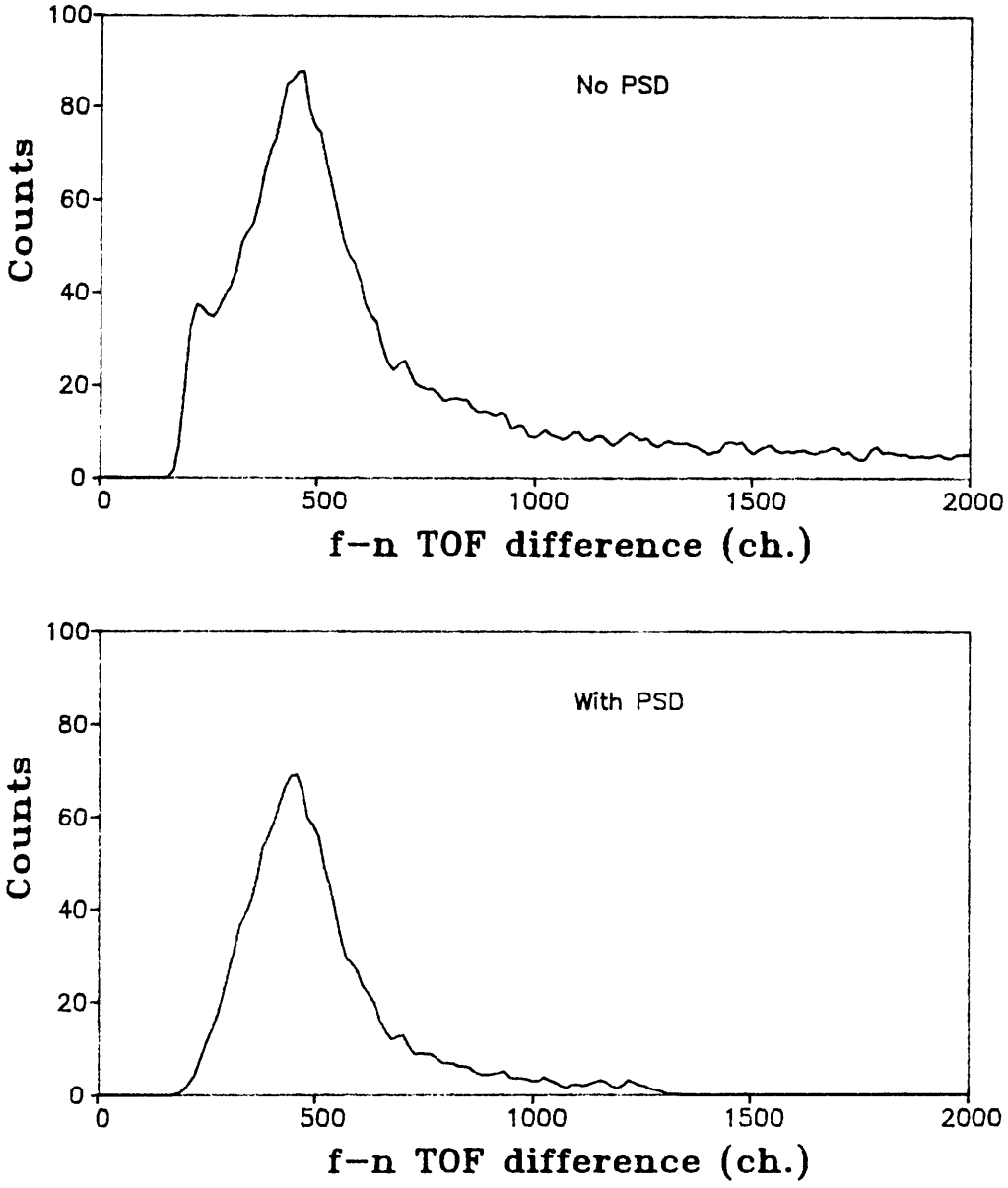

FIGURE 3.11 Typical neutron TOF difference, with respect to 0^{o} fragment detection, distribution with and without a pulse shape discrimination cut. Note the effectively total removal of background events.

The neutron energy uncertainty caused by the width of the γ-ray peak was a major drawback to the neutron energy resolution of the data. The γ-ray peak dispersion was an inherent feature of the variation in fragment kinetic energy for a given fragment mass. Compounded within this dispersion was the distortion to the fragment kinetic energy distribution due to fission fragment energy degradation in the fission foil. Since the γ-ray distributions had a dispersion of 2.5 ns FWHM, the uncertainty in neutron energy for the 0^{o} detector was taken to be -0.05, +0.05 MeV at 0.5 MeV, -0.15,+0.17 MeV at 1 Mev, -0.35, +0.50 MeV at 2.0 MeV and -1.3,+2.0 MeV at 5 Mev neutron energy. Neutron-fragment angular correlations will be presented for mean neutron energies of 0.5 1.0, 1.5, 2.0, 2.5, 3.0, 4.0, 5.0 and 6.0 MeV. Beyond 6 MeV the number of counts were too few for adequate statistics.

The statistical errors introduced to the angular distributions depended on the data sets outlined in section 3.3, the worst case being for n-f angular distributions as a function of neutron energy and fragment mass in which the data bins contained, on average, 30 events.

3.5 Results

In presenting the n-f angular correlations, the spectra are all with respect to the light fragment direction. It should be noted that this does not necessarily mean that the neutron was emitted by the light fragment. Comparison of the results is made with published data wherever possible.

The neutron-fragment angular correlations obtained in this experiment are presented in tabulated form in Appendix B. Only statistical errors have been given. The contribution to the error due to systematic factors is uncertain, but felt to be small on the grounds of satisfactory agreement of a number of independent, but inter-related, parameters (for example, LH/HL fragment detection rate, correspondence between 30^{o} LH n-f data and 150^{o} HL data, etc.).

3.5.1 Neutron energy distribution

Figure 3.12 is the neutron energy distribution in the laboratory frame of reference, measured at 0^{o}, 30^{o}, 60^{o}, 90^{o}, 120^{o}, 150^{o} and 180^{o} with respect to the light fragment direction. Each plot is compared with a Maxwellian distribution as described in equation 1.7.2 with a temperature T = 1.33 MeV. In the lower energy (< 1.5 MeV) region of the distributions there is evidence of the effective mixing of the neutron emission spectra from the light and heavy fragments, the difference between 0^{o} and 180^{o} being a reflection of the neutron multiplicity ratio $\bar{\nu}_l/\bar{\nu}_h$ (≈ 1.18). Interpolation of the data over the full angular range yielded a neutron energy distribution shown in Figure 3.13 and compared with a Maxwellian distribution, as in equation 1.7.2 with T = 1.33 MeV. It can be seen that the experimental and published data agree within error bars over the energy range of interest in this analysis, that is, from 0.5 to 5.0 MeV.

3.5.2 n-f angular correlation

Summation of all the data, $E_n \geq 0.5$ MeV, as a function of light fragment direction resulted in a n-f angular correlation as shown in Figure 3.14, in which the data is compared with published results of Fraser (Fr52) and Skarsvag Sk(63) over the equivalent energy range.

The ratio $N(0^{o}):N(90^{o}):N(180^{o})$ of $8.75 \pm 0.62:1:4.28 \pm 0.48$ is comparable to the result of Skarsvag of $8.63 \pm 0.32:1:3.81 \pm 0.14$. The n-f angular correlation is considerably more anisotropic than the data of Fraser.

3.5.3 n-f angular correlation as a function of neutron energy

Figure 3.15 is an isometric plot of the n-f angular correlation as a function of neutron energy. The data of Skarsvag (Sk63) have been plotted for 0^{o} and 180^{o} points, indicating the comparison in the trend of the angular correlation with increasing neutron energy. To facilitate visibility, error bars have only been included selectively.

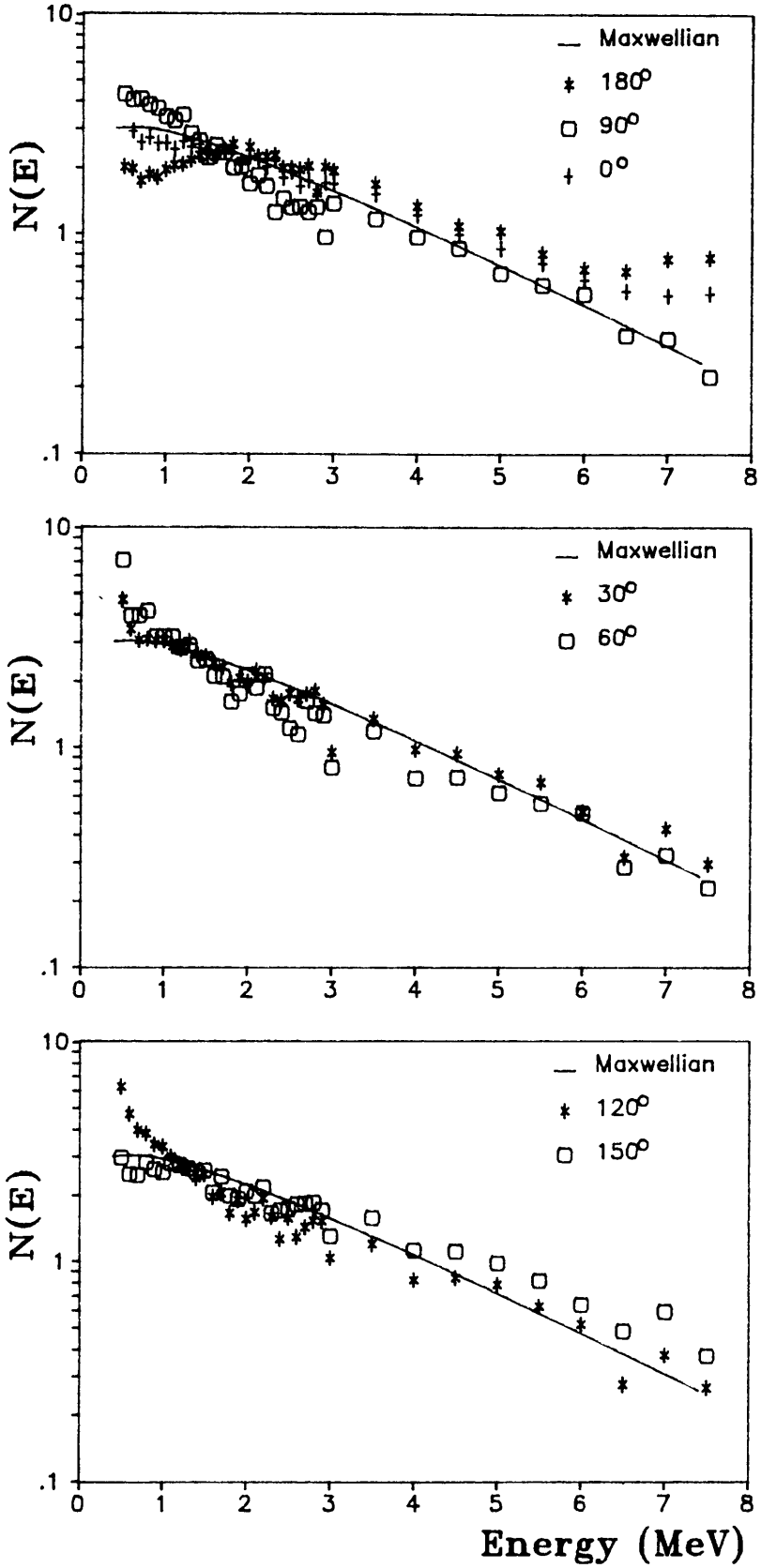

FIGURE 3.12 Neutron energy distributions at selected angles with respect to the light fragment direction and compared with a Maxwellian distribution with temperature 1.33 MeV.

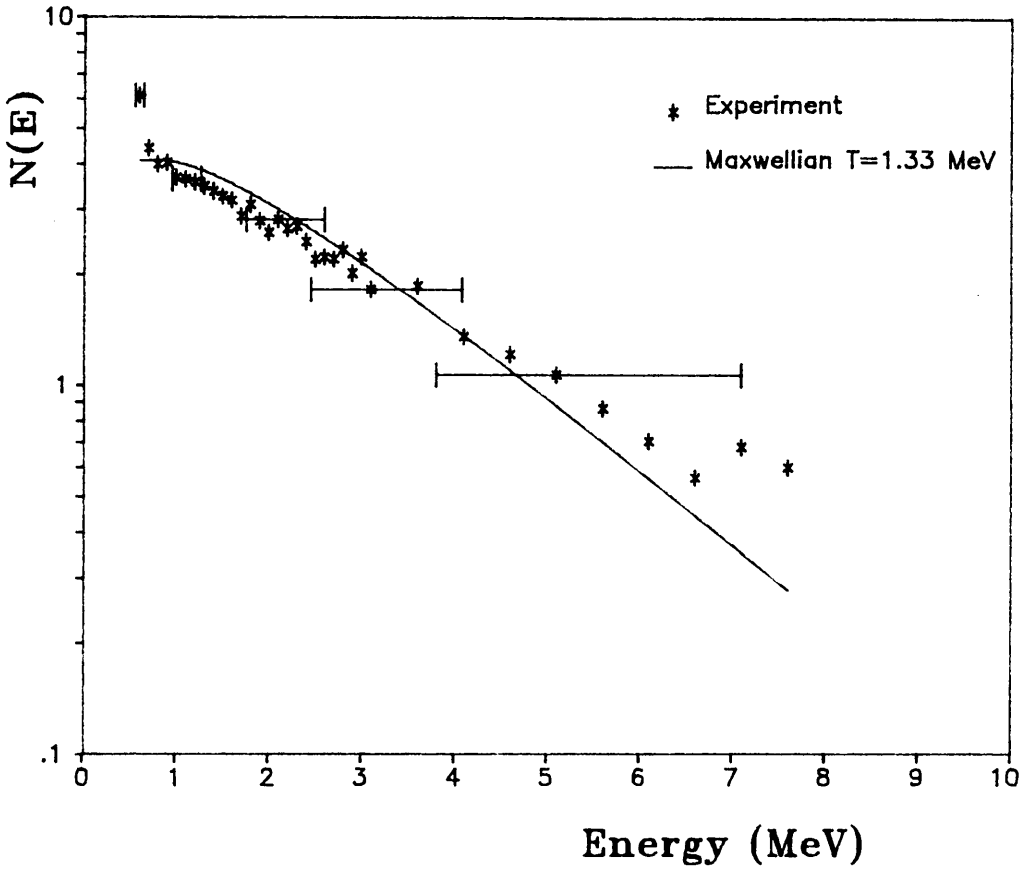

FIGURE 3.13 Interpolated total laboratory neutron energy distribution compared with a Maxwellian distribution. The error bars shown are due to the width of the γ-ray peak.

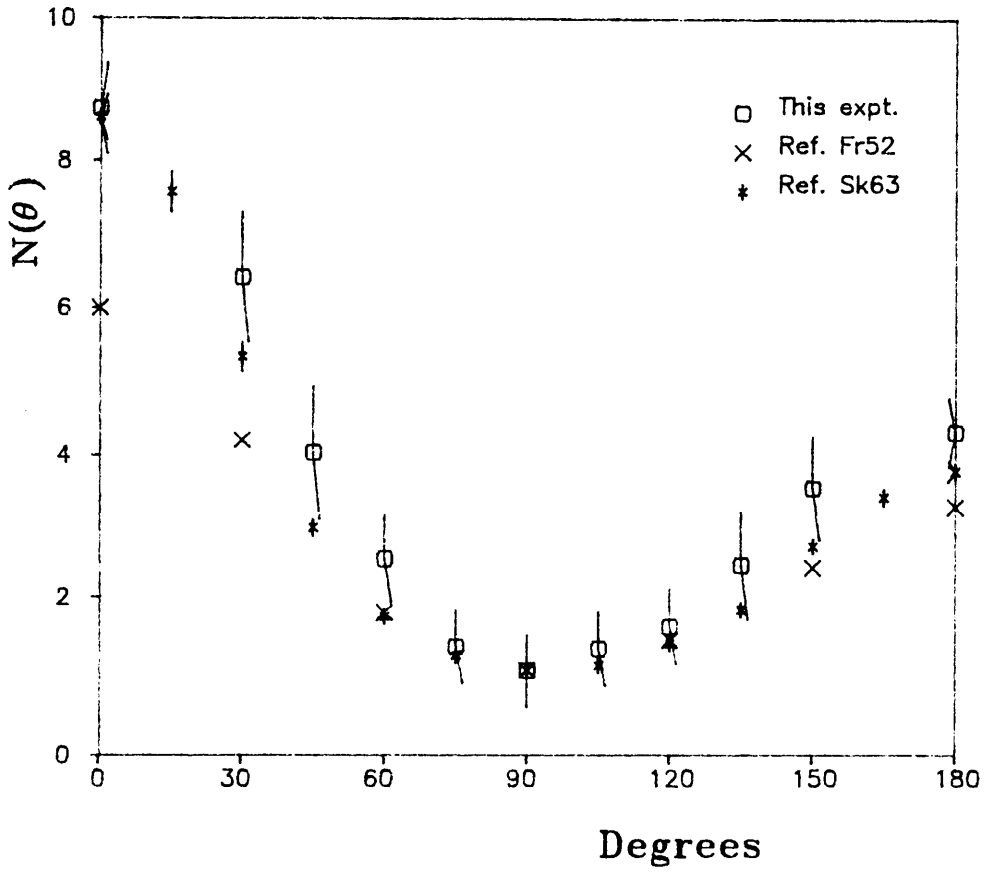

FIGURE 3.14 Neutron-fragment angular correlation for this experiment (o) with respect to the light fragment direction, compared with Ref. Fr52 (X) and Sk63 (*) for similar neutron energy ranges. All data has been normalized to N(90^{o}) equal to unity.

Of interest in the plot is an apparent levelling-off in the increase in anisotropy at 0^{o} around 3 MeV, which is also observed in the data of Skarsvag. However, although the effect is duplicated at 180^{o} this is not the case with the Skarsvag data. The mechanism creating this fluctuation is unknown.

3.5.4 n-f angular correlation as a function of fragment mass

Figure 3.16 is an isometric plot of the n-f angular correlation for all neutron energies as a function of light mass regions 85±5, 95±5, and 105±5. No comparison of this data has been made since no previously published measurement of such distributions exists for ^{235}U (n_{th},f).

An interesting feature of the data appears if one compares the ratio $N(0^{o})$: $N(180^{o})$ for the tnree mass regions, which are 1.88, 2.23, 2.70 respectively. This implies that the anisotropy is becoming more forward-peaked (with respect to the light fragment direction) as the fragment mass division becomes more symmetric. Comparing these values with the yield-weighted neutron multiplicity (Bo71) ratio $\bar{\nu}_l/\bar{\nu}_h$ over the same mass regions one obtains the values 0.63, 1.16, 1.96 respectively. For a simplistic assessment of the neutron emission process one would have expected to observe a change in the angular correlation, in going through the mass range, from a backward-peaking distribution (A = 85) to a forward-peaking one (A = 105).

3.5.5 n-f angular correlation as a function of fragment mass and neutron energy

The n-f angular correlations for mass regions 85±5, 95±5 and 105±5 as a function of neutron energy (0.5 - 5.0 MeV) are illustrated in Figure 3.17.

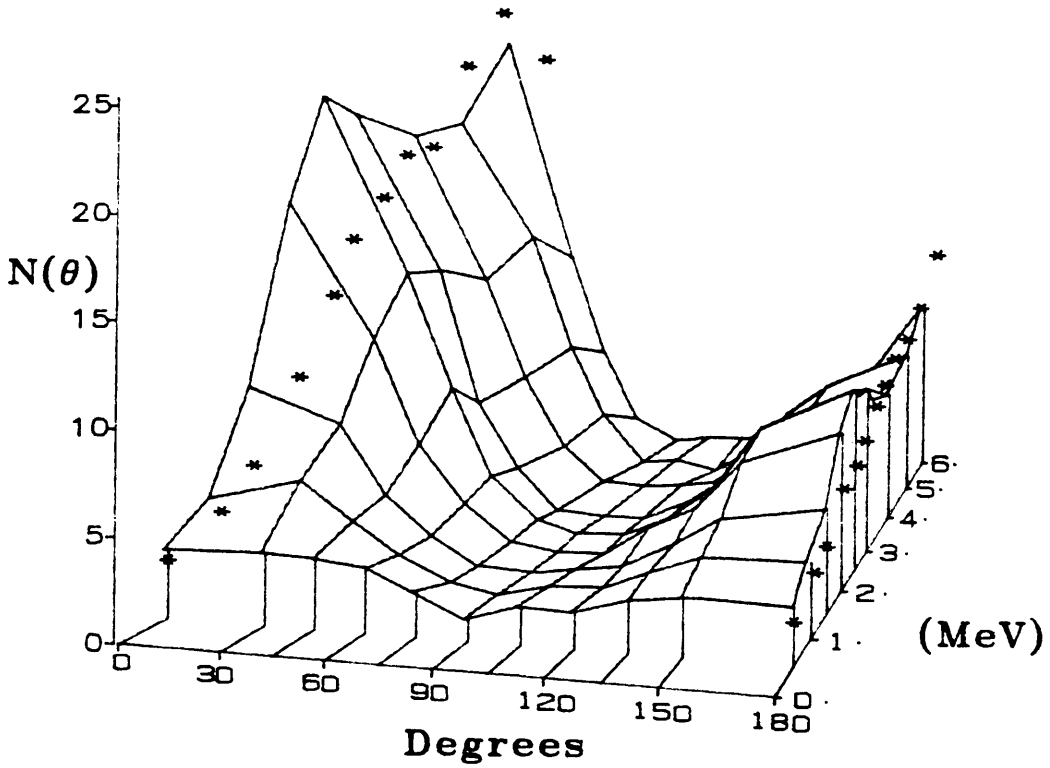

FIGURE 3.15 Neutron-fragment angular correlation, with respect to light fragment direction, as a function of neutron energy. Comparison is made at 0^{o} and 180^{o} with ref. Sk63 (*).

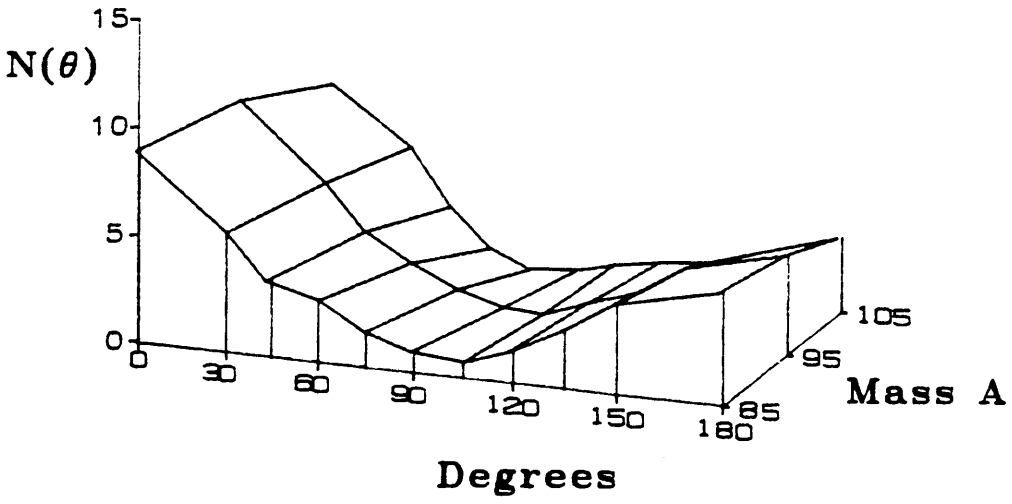

FIGURE 3.16 Neutron-fragment angular correlation, with respect to light fragment direction, as a function of fragment mass division region for all neutron energies.

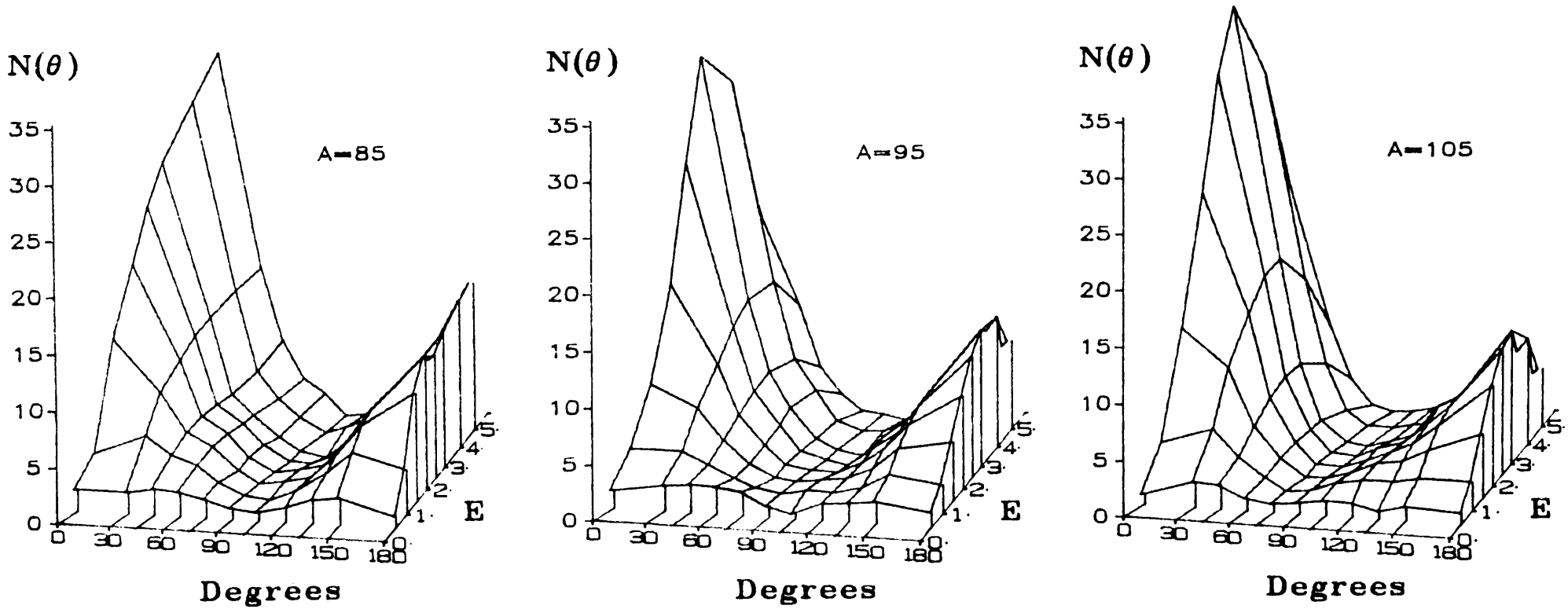

FIGURE 3.17 Neutron-fragment angular correlation, with respect to light fragment direction, as a function of neutron energy for the three mass division regions.

From these distributions can be seen a further indication of the difference in neutron emission characteristics, as a function of neutron energy for the three mass division regions. The variation in the ratio $N(0^o):N(90^o)$ with energy for the three mass regions appears to account for the observed fluctuations seen in the angular correlation for all fragment masses (Figure 3.15), although the mechanism for this is not directly obvious.

The trend in the ratio $N(0^o):N(180^o)$ is comparable above 1.5 MeV for the three mass regions, as shown in Figure 3.18. However, below 1.5 MeV unusual fluctuations are observed. Due to the complex nature of the neutron emission process in fission, it is not easy to draw immediate conclusions as to the meaning of the observed effects. It is important to note that although the data have been normalized to the 90^o data set to unity, errors in the 90^o value will be reflected equally for all data points in the normalization. Thus the effect of errors in $N(90^o)$ will not affect the comparison of $N(0^o):N(180^o)$.

3.6 Discussion

Experimental results have been presented of the measurement of n-f angular correlations as a function of both neutron energy and fragment mass region. Taking into account the statistical errors on the data, and from comparisons of the data with published results, the structure seen in the n-f angular correlations, as a function of neutron energy and also as a function of fragment mass region, was considered significant.

The motivation for this experiment was to search for evidence of a scission-neutron component in neutron emission from fission, and/or any deviation from isotropic emission of neutrons in the fragment centre of mass frames of reference. In order to identify these components a theoretical model of the neutron emission process needed to be developed, the parameters within the model being possible indicators of scission and anisotropy components.

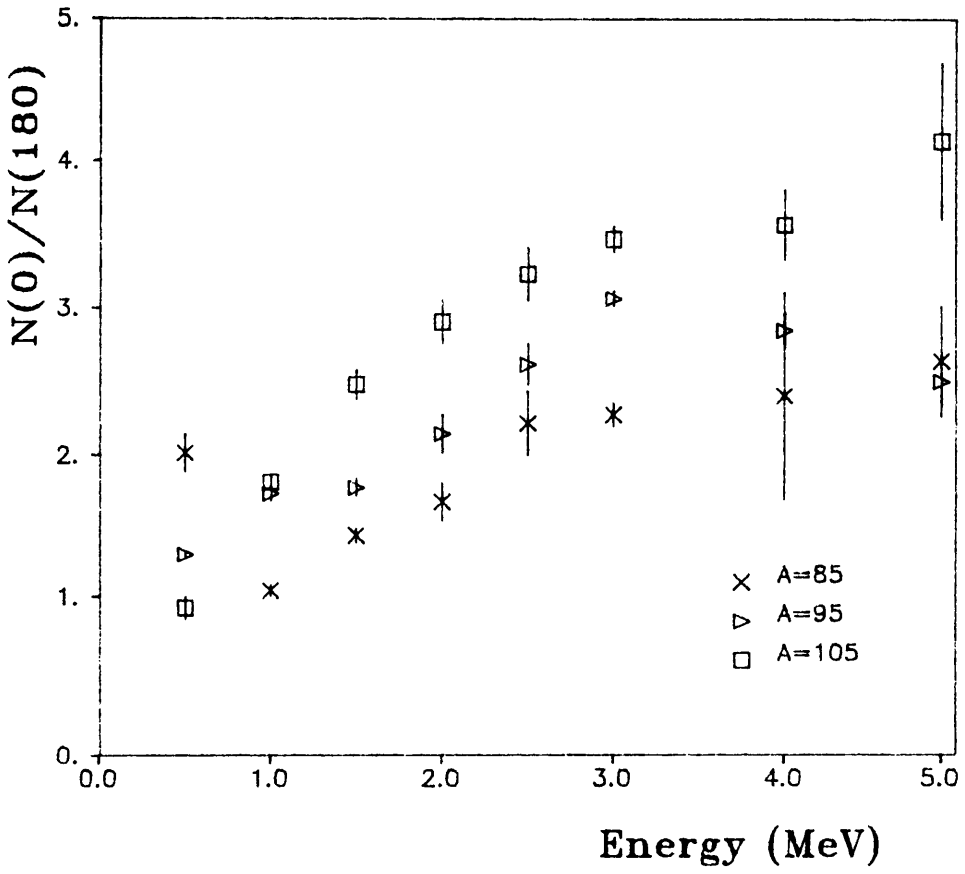

FIGURE 3.18 Variation in the ratio $N(0^{o}):N(180^{o})$ over the neutron energy range for the three mass regions.

4 MONTE CARLO SIMULATION OF FISSION

4.1 Introduction

Depending on what aspect of the fission process is studied, theoretical models of the fission process have been developed (Mo77, Ki80, Be81, Ma82) that are capable of predicting, with fair accuracy, the observable effects of interest, such as prompt mass, charge and kinetic energy distributions, etc. Extrapolation of the models to other areas of interest invariably leads to deviation of the results compared with experimental data.

The problem encountered in this experiment is that the whole fission process plays an important role in the formulation of a model to predict the measured angular correlations. Although it would be possible, in principle, to formulate a model that made use of the best theoretical treatments yet developed, it would be impractical due to the massive computer memory and computation time requirements.

For the purpose of this work two models were investigated that attempted to reproduce the measured n-f angular correlation data as a function of mass division, the laboratory frame neutron energy distribution, and provide an indication of the magnitude and form of the neutron emission components at scission, during fragment acceleration and from fully accelerated fragments.

4.2 Simple model

To simulate the fission process an algorithm must be produced with realistic input and output parameters. As a first approximation, in an attempt to duplicate the observed n-n angular correlation results in ^{252}Cf s.f. by Pringle (Pr77), a simple model of the fission process was developed.

This model made use of input parameters such as prompt mass distribution, fragment kinetic energy distribution, and average neutron

multiplicity as a function of fragment mass, $\bar{\nu}$ (A). The neutrons were assumed to be emitted with a Maxwellian energy distribution and $\bar{\nu}$ (A) assumed to be of a Gaussian form with a mean equal to the experimentally determined values. This type of distribution was also utilized (Fr 78), for a description of the n-n angular correlation in $^{235}U(n_{th},f)$. However, it was felt to be unrealistic (besides producing unsatisfactory correlation predictions) and a binomial distribution was chosen. The advantage of a binomial distribution is the imposition of a definite cut-off in the maximum number of neutrons a fragment could emit corresponding to a finite available excitation energy. The binomial distribution used was of the form:

$$P_\nu = \frac{m!}{\nu!(m-\nu)!} * (\bar{\nu}/m)^\nu * (1-\bar{\nu}/m)^{m-\nu} \qquad (4.1)$$

where ν is the number of neutrons emitted with value of m equal to 3,4 or 5, the value of m finally selected being one which gave the best neutron multiplicity distribution averaged over all fragment masses.

Figure 4.1 is a comparison of the neutron multiplicity distribution for a particular fragment mass using a Gaussian and a binomial distribution. No data exist regarding the neutron multiplicity distribution for individual fragment masses, therefore one has to depend on the resultant shape of the averaged distribution. Figure 4.2 illustrates the distribution resulting in the two cases when averaging the multiplicity over all fragment masses. Note that the distribution due to averaging many Gaussians is now a histogram.

When using a binomial distribution, with m = 4, the resultant total average neutron multiplicity agreed reasonably well with experimental data. A scission-neutron component was essential in order to duplicate the experimental n-f angular correlations. However, n-n angular correlation predictions did not agree satisfactorily with the measured values.

The major drawbacks of the simple model were:

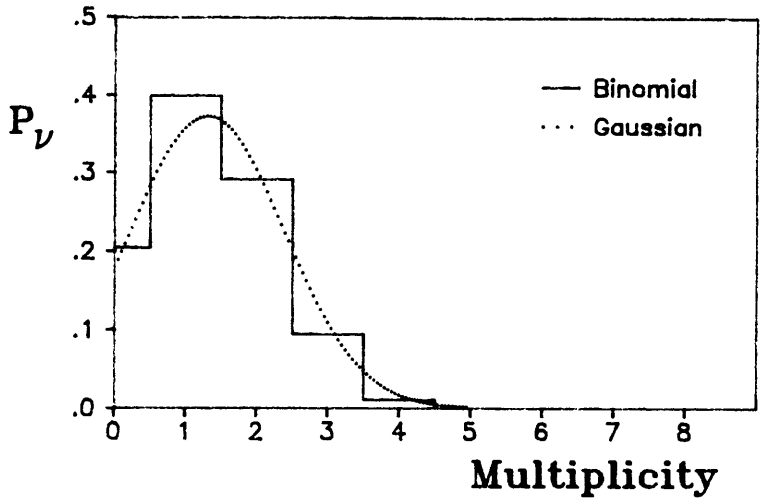

FIGURE 4.1 Calculated neutron multiplicity distribution for a binomial and Gaussian distribution for an individual fragment with average neutron multiplicity of 1.4.

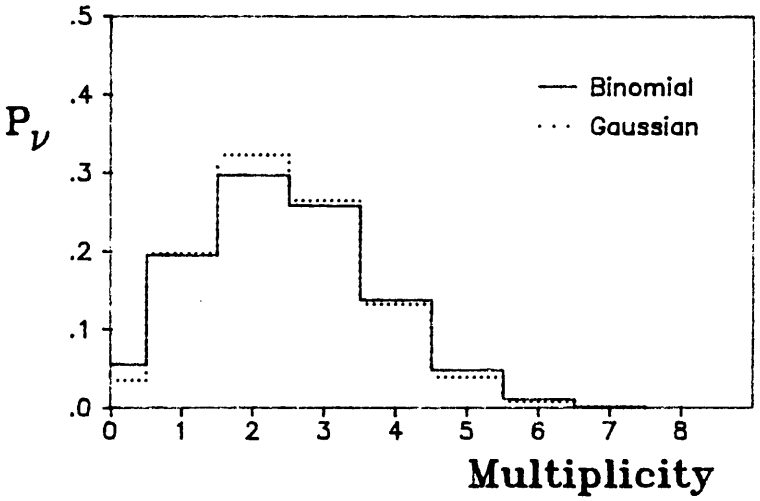

FIGURE 4.2 Calculated neutron multiplicity distribution averaged over all fission fragments emitting neutrons with either a binomial or Gaussian distribution and resulting in an average total neutron multiplicity of 2.416.

1) No account was taken of the charge distributions for each fission fragment mass division. The effect of this was a) on the kinetic energy distribution, since this is mainly derived from Coulombic repulsion of two charge centres i.e. $Z_1 * Z_2 / r^2$, and b) on the amount of excitation energy available for neutron emission, this being a function of the binding energy of the nucleus for a specific (A,Z) configuration.

2) No energy restriction was applied to the number of neutrons emitted by the fission fragments. This is an important feature when considering fission fragments with greater than average kinetic energy. Experimentally it has been shown (Sc73) that such fragments have minimal excitation energy and therefore have a very low probability of emitting neutrons.

3) The fact that angular momentum effects, which also play a role in restricting last neutron emission, that is, competition of γ-ray emission over neutron emission, become more prominant for higher fragment residual angular momentum was neglected.

4) There were no kinematic restrictions when neutron kinetic energy was randomly sampled from a Maxwellian form, whereas for each emission event the neutron kinetic energy should be dictated by the amount of excitation energy available in the nucleus.

5) When including a scission component, the effect upon binding energy excess (and thus excitation energy, neutron energy distribution) is ignored.

The conclusion to be drawn from the results and flaws of the simple model was that more careful consideration of the neutron emission characteristics in fission was needed in order to simulate the observed n-n and n-f angular correlations. It has been demonstrated (Ma85) that false interpretations of the n-f angular correlations can result when using rough models of the fission neutron emission process. A new model was produced which was more realistic energetically, that is, it took into account the drawbacks mentioned above.

4.3 New Monte Carlo model

In developing this model, approaches similar to those used by other researchers (Mo77, Ma82, Be81) were followed. A basic difference of this model with respect to the others is the final purpose of the procedure, namely to simulate neutron-fragment angular correlations and to take into full consideration a possible scission neutron component and possible emission during fragment acceleration.

4.3.1 Primary mass yield

Most data on fragment mass yields are from fission products. Measurements of primary mass yields involve precise measurement of the momentum and kinetic energy of both fragments, and such data have only recently started to become available from such detector systems as Cosi fan tutte, at ILL, Grenoble. Estimates of the primary mass yield, based on measurements of neutron yield as a function of fragment mass, have been made (Bo71) and these data were used for the average primary mass yield.

4.3.2 Nuclear charge distribution

No data exist for the average nuclear charge distribution as a function of primary fragment mass. Therefore it was necessary to estimate a nuclear charge distribution for the primary fragments. In estimating a nuclear charge, a Gaussian distribution was assumed such that the charge could be as much as $\pm$ 2 units of charge from the mean value assumed. The main criterion in making an estimation of the nuclear charge was to reproduce the nuclear charge distribution for product mass 80-107 as measured by Lang et al (La80) and the width of the distribution $\sigma_z(A)$. The procedure followed in determining the initial fragment nuclear charge will be outlined in more detail in section 4.3.8. A feature also incorporated was the simulation of the observed odd-even charge effect seen in fission experiments, which was incorporated within the fragment de-excitation process.

4.3.3 Fragment kinetic energy

Calculating the fragment kinetic energy was impractical since knowledge of the degree of fragment deformation was required. Models have been produced (Da75) in which the distance between the nuclear centres was calculated, providing information not only on fragment kinetic energy but also excitation energy. However, due to the uncertainties involved in the calculations, inclusion of this feature was neither justifiable nor practical.

The total kinetic energy distribution as a function of prompt fragment mass was therefore taken from Asghar et al (As78) and Belhafaf et al (Be83). The dispersion about the mean was taken to be the effect of differing Z_1/Z_2 ratios. Thus a Z_1/Z_2 ratio greater than mean Z_1/Z_2 had a higher kinetic energy than the mean total kinetic energy, and vice versa.

4.3.4 Binding energy release

A criterion had to be met where the total binding energy release had to be greater than the fragment kinetic energy. If this was not met that particular fission configuration was rejected. In determining the total binding energy release for each fission configuration the mass tables of Wapstra and Bos (Wa77) were used.

The residual energy release was assumed to be distributed between the fragments in the form of deformation energy and intrinsic excitation. Present understanding of how this energy is shared between the fragments is limited. As a first approximation the excitation energy of the fragments was deduced from the following relationship:

$$Ex = \nu(BE + \eta) + E_\gamma \qquad (4.2)$$

where ν is the average neutron multiplicity, BE is the average neutron binding energy, η is the average neutron kinetic energy, and E_γ is the average total energy in γ-ray emission.

This value was calculated for each fragment mass and the ratio of the excitation between complementary fragment masses was used to define the sharing of the residual excitation energy for each simulated fission. The ratio for each fragment mass division was adjusted until satisfactory average neutron multiplicities were obtained.

4.3.5 Fragment de-excitation

The most favoured mode of fragment de-excitation is initially by neutron emission, but as the residual fragment excitation energy approaches the separation energy of the last neutron, de-excitation by γ-ray emission begins to compete due to the high angular momentum state of the fragment. Therefore some cut-off energy which was greater than the separation energy of the last neutron was empirically selected.

The neutron evaporation process followed similar lines to one of the earliest Monte Carlo calculations (Do59), based on Weisskopf's nuclear evaporation model (We54). The probability of observing a neutron of kinetic energy, e, was assumed to be of the form:

$$P(e)\,de = \sigma_{inv}(e)\,e\rho(U)\,de \qquad (4.3)$$

where $\sigma_{inv}(e)$ is the inverse cross-section for the neutron capture reaction, and $\rho(U)$ is the total nuclear level density in the final nucleus, both of which must be calculated.

4.3.6 Level density determination

The nuclear level density is defined, from Holmes et al (Ho76), by the formula:

$$\rho(U) = \frac{0.482 * \exp(2\sqrt{aU})}{A^{5/6} * U^{3/2}} \quad MeV^{-1} \qquad (4.4)$$

where a is the level density parameter. The effective residual excitation energy of the nucleus, U, is defined as:

$$U = E_x - BE_n - e - d \qquad (4.5)$$

where E_x is the initial excitation energy (prior to neutron emission), BE_n is the neutron separation energy, e is the kinetic energy of the neutron, and d is the pairing energy correction term.

For nuclei not too far removed from the β-stability valley it has been determined (Ho76) that, as a good approximation:

$$d = P - (c_1 + 80/A) \qquad (4.6)$$

where P = P(Z) + P(N) is the pairing energy correction term, and c_1 is an empirically determined constant. Similarly, the level density parameter a is defined as:

$$a = (d_1 + d_2 S) * d_3 \qquad (4.7)$$

where S = S(Z) + S(N) is the shell energy correction term, and d_1, d_2, d_3 are empirically determined constants. Table 4.1 gives the values used for c_1, d_1, d_2 and d_3 for the range of Z and N used in the calculations. The values for the pairing and shell energy correction were taken from Truran et al (Tr70).

An alternative and more simple definition of the level density parameter derived by Gilbert and Cameron (Gi65) is of the form:

$$a/A = 0.130 + 0.0102 * (S - 0.33 * D) \qquad (4.8)$$

where S is the shell correction energy, and D is the distance to the nearest closed nucleon shell.

Neither formula 4.7 nor formula 4.8 is necessarily appropriate for fission fragment nuclei. However, the more recent analysis of Holmes for nuclei close to the line of stability gives more consistent results and since odd-even effects are implied from the pairing energy correction term, this formula was used in the calculations.

Region	Number Z	Number N	c_1	d_1	d_2	d_3
$Z \leq 30$	odd	odd	0.0	0.05264	0.001592	1.2
	odd	even	0.0	0.05260	0.002209	1.2
	even	odd	0.0	0.05267	0.001901	1.2
	even	even				
$Z > 30$ non-deformed nuclei	odd	odd	0.5	0.1254	0.006929	1.0
	odd	even	0.5	0.1286	0.006723	1.0
	even	odd				
	even	even	0.5	0.1247	0.006368	1.0
$Z > 30$ deformed nuclei	odd	odd	0.5	0.1127	0.007429	1.0
	odd	even	0.5	0.1125	0.008390	1.0
	even	odd				
	even	even	0.5	0.1104	0.006922	1.0

TABLE 4.1

Empirically determined constants for calculating the level density parameter. Deformed nuclei are taken to be those nuclei with $54 \leq Z \leq 78$ and $86 \leq N \leq 122$. For $Z = N$ nuclei and $Z = N-1$, $N =$ closed shell values the level density parameter is divided by 1.1.

4.3.7 Inverse cross-section determination

Since the fission fragment is a nuclide that is far from the line of nuclear stability, knowledge of characteristics such as neutron absorption cross-section is virtually non-existent. One must therefore extrapolate from data applicable in known areas. Empirically a relationship such as (We 54):

$$\sigma(e) = a + b/e \qquad (4.9)$$

can be used, where $a = 2.2 + 0.76A^{2/3}$ and $b = 2.12A^{-2/3} - 0.05$. Since such a model does not take into account the neutron-to-proton ratio - a feature applicable in other areas of the Monte Carlo, a more complete description of the cross-section formulation was chosen.

By adaptation of a computer program, PELINSCA (En74), the inverse capture cross-section for any nucleus could be calculated. The procedure followed was to determine the cross-section in terms of the optical model. The optical potential comprised a real central part $V_c(r)$ to represent the Coulomb interaction along with a Woods-Saxon potential. The general potential V(r,E) used to describe the nucleus of radius r at energy E was of the form

$$V(r,E) = V_c(r) - V_0 \pm \left[\frac{(N-Z)}{A} Vss\right] f(r) - i\, W_{vol}\, f(r)$$

$$-iW_{sur}\, g(r) - (V_{so} + iW_{so})\, h(r)(\underline{L}.\underline{S}) \qquad (4.10)$$

where $V_c(r)$ represents the repulsive central Coulomb potential for a uniformly charged sphere of radius R_c, and V_0 represents the energy dependent attractive real part of the central potential expressed as:

$$V_0 = 46.0/\ (1.0 + 0.00646*E + 0.000035*E^2) \qquad (4.11)$$

This potential was increased for protons and decreased for neutrons by the symmetry potential V_{ss} of magnitude 27 MeV and is a term which was taken to be independent of energy. The shape of the potential as a whole is a volume distribution described by the Woods-Saxon form factor:

$$f(r) = \frac{1}{1 + \exp((r-R_v)/a_v)} \qquad (4.12)$$

where a_v represents the diffuseness of the nuclear boundary of the potential. The nuclear radius was assumed to be given by $R_v = r*A^{1/3} + r_v$, where r = 1.16 fm is the nuclear radius, the thickness of the diffuse layer r_v = 0.6 fm and a_v = 0.62 fm (En74).

W_{vol} represents the imaginary (absorption) part of the complex volume distributed central potential which is assumed to have the same form factor f(r) as the real part:

$$W_{vol} = \frac{12.5*E}{(1.0 + 0.0008*E + 0.000038*E^2)} \qquad (4.13)$$

W_{sur} represents the attractive imaginary surface-absorptive part of the central potential whose form factor is taken to be of a Gaussian form:

$$W_{sur} = \frac{14.0}{(1. + .011*E + .00065*E^2)}$$

$$R_{sur} = 1.1 + 1.16*A^{1/3}, \quad a_{sur} = 0.5 \qquad (4.14)$$

A complex attractive Thomas-spin-orbit potential was defined by $V_{so} + iW_{so}$, with $V_{so} = 0.152*V_o$, and $W_{so} = 0.112*W_{vol}$

From the optical model the total reaction cross-section, σ_{tot}, is defined as:

$$\sigma_{tot} = \sigma_{abs} + \sigma_{el} \qquad (4.15)$$

where σ_{abs} is the absorption cross-section and σ_{el} the elastic cross-section. The absorption cross-section is expressed in terms of the diagonal elements of the collision matrix S by:

$$\sigma_{abs} = \frac{\pi}{k^2} \sum_j (2j+1)(1-|S_j|^2) \qquad (4.16)$$

Since the optical model does not reproduce sharp variation in the cross-section (resonances) it therefore describes an energy averaged S-matrix element $<S_j>$. This leads to an absorption cross-section of the form:

$$\sigma_{abs} = \frac{\pi}{k^2} \sum_j (2j+1)(1-|<S_j>|^2) \qquad (4.17)$$

$$= \frac{\pi}{k^2} \sum_j (2j+1)T_j$$

where T_j is defined as the transmission coefficient.

The program PELINSCA evaluates T_j until it becomes very small for a given j and thence the absorption cross-section computed for a given energy E. Comparisons of a typical cross-section distribution as a function of energy are given in Figure 4.3 for this model and those of Madland and Nix (Ma82) using a Becchetti-Greenlees potential, and of the simple model equation 4.9. Although the shape of the cross-section for differing nuclei was similar, the subtle differences were retained by storing the absorption cross-section for each A,Z configuration in energy bins of 0.1 MeV from 0.0 to 10.0 MeV in a file on disc. The inverse cross-section σ_{inv} required for the Monte Carlo was merely the stored cross-section for fragment A+1,Z.

4.3.8 Neutron emission

For each excitation energy a neutron emission probability distribution P(e)de was produced. This distribution was randomly sampled to produce a neutron with kinetic energy e. This process was repeated until the residual excitation energy was less than the defined cut-off energy required for further neutron emission (neutron separation energy plus dE_x).

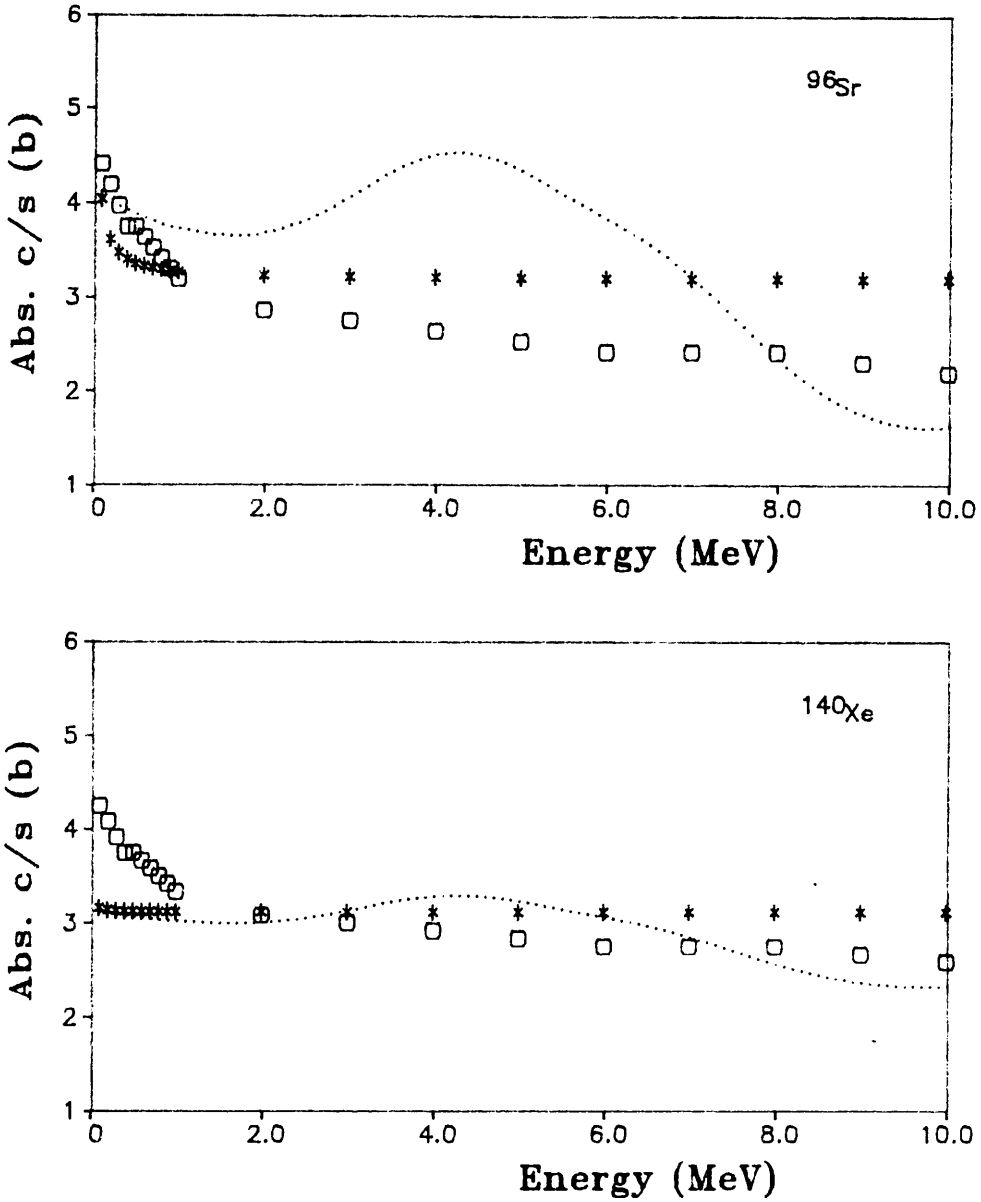

FIGURE 4.3 Typical absorption cross-section distributions for two nuclei, calculated using PELINSCA (...) compared with those of ref. Ma82 (□) and the simple relationship $\sigma = a + b/e$ (*).

As has been mentioned in section 1.5, the effect of high fragment angular momentum would act to suppress neutron emission, especially last neutron emission. Although angular momenta have not actually been taken into account fully in this model, a cut-off energy in excess of the separation energy for last neutron emission was imposed. The value of the cut-off energy was selected empirically for each prompt fragment mass.

One of the initial variable parameters which has an influence on the neutron multiplicity is the initial fragment charge distribution, since this affects the binding energy release per fission and hence the amount of available excitation energy. This parameter was adjusted over all fragment masses until reasonable agreement was obtained in reproducing the product charge distribution and neutron multiplicity distribution as a function of fragment mass. The other variables playing an important role were the selection of the excitation energy ratio and the energy cut-off point for last neutron emission.

4.3.9 Other modes of neutron emission

Two other modes of neutron emission were considered: 1) Scission neutrons, that is, neutrons emitted from a frame of reference at rest in the laboratory. 2) Neutron emission from fragments with velocity less than the final fragment velocity, that is, during fragment acceleration.

The number of neutrons per fission assumed to originate at scission was sampled between 0.0 (i.e. no scission component) and 0.7, representing a scission component of 30% of the average total neutron multiplicity of 2.416. Since there is as yet no reliable knowledge of the form of the scission neutron energy distribution, it was assumed to have a Maxwellian form, the variable parameter here being the temperature T to be used. Values for T were selected between 0.5 and 2.0 MeV, based on values sampled by previous authors (Ka63, Kl71, Gr73, Pi77). Introduction of a scission component is at the expense of excitation energy to be shared between the fragments. The simplest assumption was to share the residual excitation energy between the two fragments in the same manner described for the simulation with a zero scission component.

Emission during acceleration was only considered in a situation with zero scission neutron component. A simple method was used for sampling emission during fragment acceleration; if the fragment excitation energy was greater than a specified minimum (Ex) one neutron could be emitted from a fragment moving at a specified fraction, c, of the final fragment velocity v_f, where $0 \leq c \leq .9\ v_f$.

4.3.10 Containment of variable parameters

For a particular mode of scission component the Monte Carlo simulated 100 000 fission events; each event was recorded on magnetic tape. A flow chart of the procedures followed to simulate each fission event is given in Figure 4.4. The content of the data recorded per event is shown in Table 4.2.

In the Monte Carlo the important variable parameters as a function of fragment mass were:

1) The average charge of the prompt fragments
2) The dispersion in the average charge
3) The dispersion in the fragment kinetic energy
4) The ratio for sharing the residual excitation energy between the fragments
5) The cut-off value in the excitation energy to mimic γ-ray competition

These parameters were adjusted until satisfactory agreement was obtained for those distributions that could be compared with experimental data, such as product fragment mass yield, product charge distribution, average product kinetic energy distribution and average neutron multiplicity as a function of fragment mass.

Appendix C gives the computer program for simulating the fission process, with appropriate comments supplied, indicating important variable parameters. Also included is a program adapted from PELINSCA to generate the inverse absorption cross-sections. This program also provided values for the maximum angular momentum of the emitted neutron, but this aspect was not used.

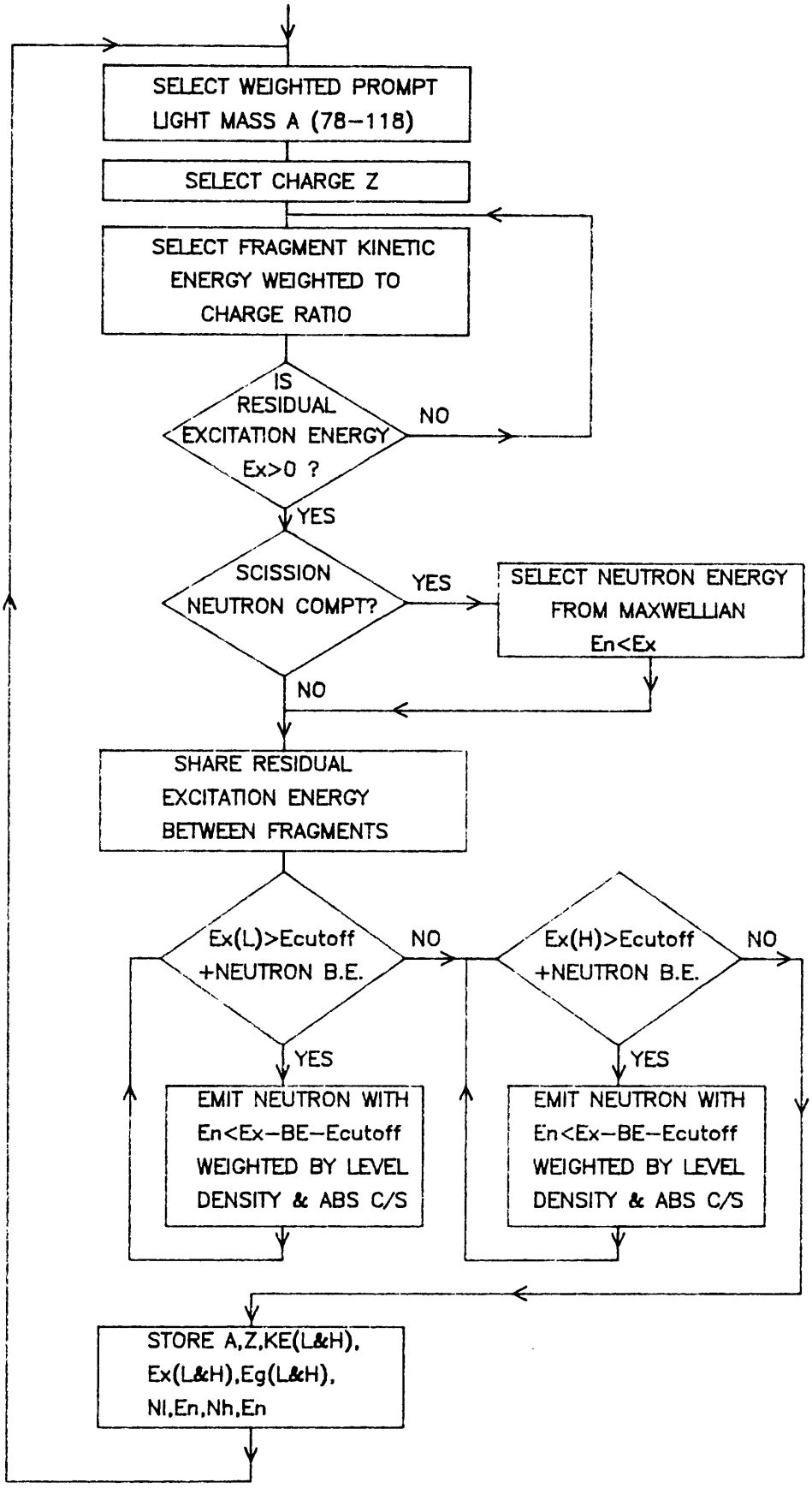

FIGURE 4.4 Flow chart of the procedure followed in simulating a fission event.

WORD	DATA CONTENT	
1	Event no	
2	A_L	Light mass number
3	Z_L	Light fragment charge number
4	E_L	Light fragment kinetic energy
5	E_H	Heavy fragment kinetic energy
6	E_{XL}	Light fragment excitation energy
7	E_{XH}	Heavy fragment excitation energy
8	$E_{\gamma L}$	Light fragment residual energy
9	$E_{\gamma H}$	Heavy fragment residual energy
10	ν_L	Number of neutrons emitted by light fragment
11-19	En1-9	Neutron kinetic energy
20	ν_H	Number of neutrons emitted by heavy fragment
21-29	En1-9	Neutron kinetic energy

Table 4.2 Content of data array stored for each simulated fission event.

4.4 Centre-of-mass neutron emission characteristics

Comparisons of the neutron multiplicity distribution, P_ν, with experimental data (Bo71) are presented in Table 4.3 for simulations having a 0% and 20% scission neutron component. The variation in width of the two simulations is a reflection of the reduction in average excitation energy available for sharing between the fragments when a neutron is emitted at scission.

The neutron energy distribution in the light fragment centre of mass frame for first, second and third emitted neutron, in a typical simulation, is shown in Figure 4.5, illustrating the effect of lower excitation energy for further neutron emission. Illustrated in Figure 4.6 are the total simulated neutron energy distributions in the light and heavy fragment centre-of-mass frames compared with Maxwellian distribution with temperature T_m = 0.7 and 0.58 MeV respectively. In a simulation of 100 000 events neutron centre-of-mass energies up to 8.5 MeV and 6.5 MeV from the light and heavy fragments respectively were observed, indicating the possibility of observing neutrons with energy up to 16 MeV in the laboratory frame of reference. Within the framework of the Monte Carlo even higher energies were feasible.

The neutron emission characteristics generated thus far are comparable with known experimental data, and have a more realistic foundation than the simple model described in section 4.2.

4.5 Angular correlation results

In order to simulate the angular correlations observed experimentally in this work and other published data, it is necessary to transform the neutron frame of reference from the fragment to the laboratory. To do this the neutrons were sampled for emissions over angles $0 \leq \theta \leq \pi$ and $-\frac{\pi}{2} \leq \phi \leq \frac{\pi}{2}$, where $\theta = 0, \pi$ lies along the fission axis and ϕ lies in a plane perpendicular to the fission axis.

P_ν	Ref. Bo67	Monte Carlo 0%	Monte Carlo 20% scission compt
0	0.031 ± 0.006	0.006 ± 0.001	0.003 ± 0.001
1	0.173 ± 0.002	0.064 ± 0.001	0.095 ± 0.001
2	0.334 ± 0.003	0.508 ± 0.002	0.439 ± 0.002
3	0.308 ± 0.003	0.333 ± 0.002	0.405 ± 0.002
4	0.123 ± 0.002	0.089 ± 0.001	0.058 ± 0.001
5	0.028 ± 0.002	0.0001 ± 0.0001	0.003 ± 0.001
6	0.004 ± 0.002		
$\bar{\nu}_t$	2.416 ± 0.008	2.435 ± 0.005	2.425 ± 0.005
ν_{1/ν_h}	1.18	1.20	1.21

Table 4.3 Comparison of experimental data for neutron multiplicity with Monte Carlo prediction for scission components of 0% and 20%.

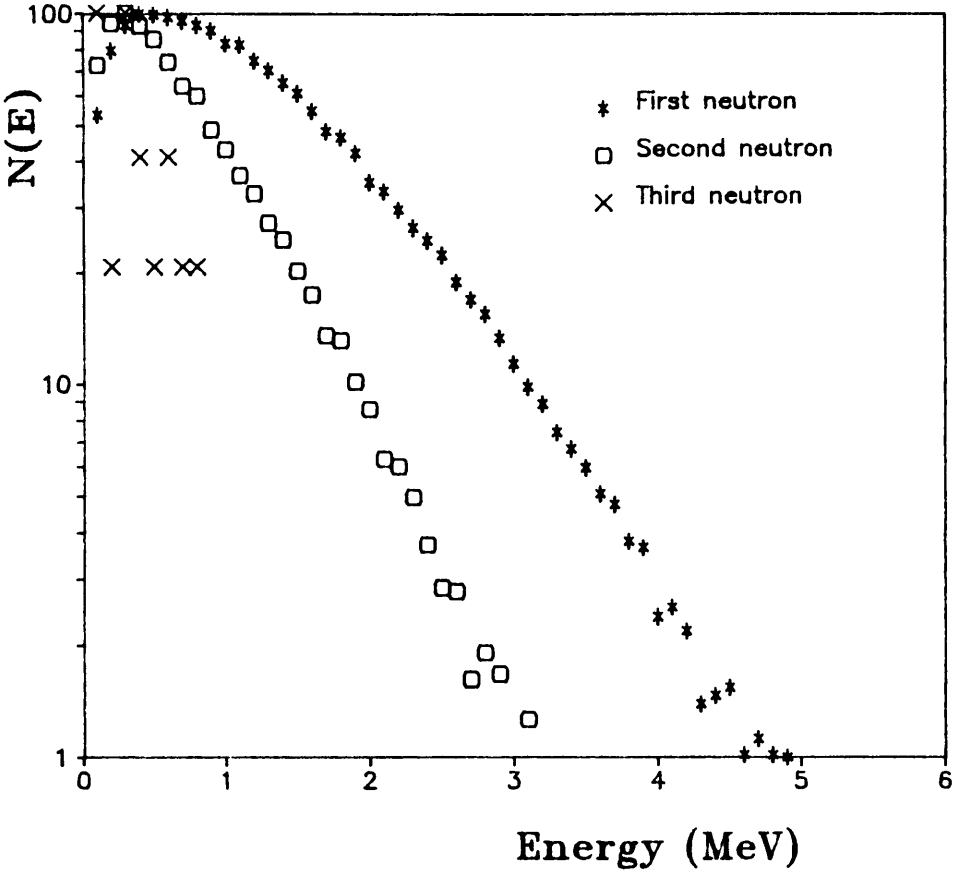

FIGURE 4.5 Calculated neutron energy distribution in the centre of mass frame of the light fragment for first, second and third neutrons emitted from the light fragment. The distributions were normalized to a maximum equal to 100. The probability of observing one, two and three neutrons was 0.629, 0.349 and 0.0004 respectively for this simulation.

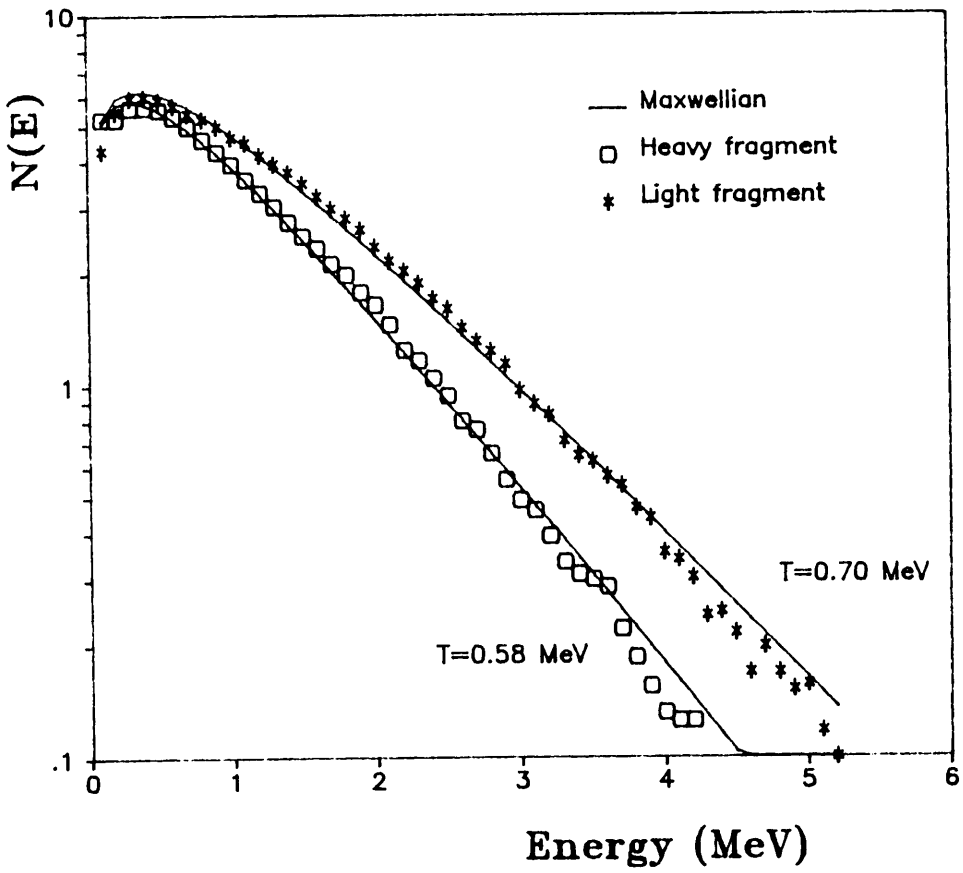

FIGURE 4.6 Calculated neutron energy distribution in the centre-of-mass frames of the respective light and heavy fragments and compared with Maxwellian distributions.

4.5.1 n-f angular correlations

The large number of possible combinations was considerably reduced by initially comparing, with experimental data, the predicted n-f angular correlation averaged over all fragment mass divisions and appropriate neutron energy range. The ratio $N(0^o):N(180^o)$, which will be defined as C_{n-f}, was a convenient parameter to compare with experimental data, since the correlations were all normalized to $N(90^o)$ equal to unity.

The first phase of the analysis was to simulate the fission process with a zero scission neutron component and for all neutron emission to take place isotropically in the centre-of-mass frames of fully accelerated fission fragments. The result of such a simulation was C_{n-f} = 11.2:6.92, compared with an experimental value of 8.76:4.28. This result was comparable with the simulations using the simple model (section 4.2 and reference Fr 78).

The next step was to introduce a) an anisotropy in the emission of neutrons from fully accelerated fragments, b) emission during fragment acceleration, and also a combination of a) and b). Introducing an anisotropy of the form $(1+b\cos^2\theta)$, ($\theta=0^o$-180^o along the fission axis) had the effect of increasing the anisotropy in C_{n-f}. An anisotropy of the form $(1+b\ \cos^2\ (90-\theta))$ improved the comparison of C_{n-f}, but insufficiently to provide satisfactory agreement with experimental data. Assuming isotropic emission from accelerating fragments for excitation energies, Ex, in excess of a given quantity improved the quality of the fits. Best fits to C_{n-f} were obtained for two extreme cases:

1) For $E_x > 15$ MeV and neutron emission from fragments at rest ($0.0V_f$) the result was C_{n-f} = 8.68:5.41.

2) For $E_x > 12$ MeV and neutron emission at 90% of final fragment velocity ($0.9V_f$) the result was C_{n-f} = 8.80:5.46.

A combination of a) and b) in these two cases in no way improved the fit to experimental data.

Extending the analysis for three mass division regions denoted by light masses 85, 95 and 105 the ratio C_{n-f} was again compared with experimental values:

Form of emission	(1) $E_x > 15$, $0.0V_f$	(2) $E_x > 12$, $0.9V_f$	Expt.
A = 85	4.03:4.16	5.46: 7.76	9.50:5.05
A = 95	7.92:5.84	9.07: 5.92	10.83:4.86
A = 105	9.21:6.99	17.80:10.70	10.61:3.93

A χ^2 test of the two cases, as a function of fragment mass, indicated a preference for case (1) (χ^2 = 1.1), thus implying that a scission-neutron component should be considered.

The energy distribution of scission neutrons was sampled from a Maxwellian distribution (equation 1.7.2) with a characteristic temperature T_s, which will be defined (Hi86) as:

$$E_x = a\,T_s^2 = \frac{AT_s^2}{10} \qquad 4.5.1$$

where a and A are the level density and mass respectively of the compound nucleus. This relationship corresponds to a relatively long transit time, $\sim 14*10^{-20}$s, from saddle-to-scission point compared with normally accepted values of $< 10^{-21}$s. At the saddle point the intrinsic excitation energy is considered to be taken up as deformation energy and thus correspond to a 'cold' nucleus (T_s small). For the purpose of defining T_s, if the neutron binding energy release due to

thermal neutron capture in ^{235}U of 6.5 MeV is considered as the excitation energy, then, from equation 4.5.1, $T_s \approx 0.5$ MeV. If one considers the total average excitation energy of the fission fragments, E_x = 24 MeV, then T_s = 1.0 MeV.

A scission neutron component in excess of 25 % was not studied since earlier research (Bo62, Sk63, Gr73) has implied an upper limit of about this value. Variations in n-f angular correlation, as a function of the magnitude of the scission component, were such that within the precision of the experimental data it was sufficient to simulate the fission process for two cases with scission components of 10 % and 20 %. In each case a simulation with a temperature, T_s, of 0.5 or 1.0 MeV was sampled.

The results for C_n-f, assuming isotropic emission of non-scission neutrons in the fragment centre of mass frame and isotropic emission of scission neutrons in the laboratory frame of reference, are shown in Table 4.4.

A χ^2 test of these modes of neutron emission indicated that the 20 % scission component simulations produced improved fits to the data. To see if further improvements to the angular correlations, as a function of fragment mass, could be obtained a) an anisotropy in scission neutron emission, b) an anisotropy of non-scission neutron emission, and also a combination of a) and b) were introduced. Analyzing the 10% and 20% data sets over all fragment masses, comparable best fits were obtained in which there was considered to be isotropic emission of neutrons emitted by fully accelerated fragments and anisotropic emission of scission neutrons, with emission preferentially perpendicular to the fission axis. (This conclusion is comparable to that reached by Green et al (Gr73).) However the agreement with experimental data was still unsatisfactory, especially when comparing the data over the three mass division regions, in which a strong preference for events at 180^o to the light fragment direction for A = 85 was apparent.

Scission compt.	T (MeV)	All light A	A = 85	A = 95	A = 105
10%	0.5	9.39 : 5.72	4.76 : 6.67	8.73 : 6.06	16.5 : 8.94
10%	1.0	8.78 : 5.27	4.32 : 5.29	8.05 : 6.35	15.5 : 6.89
20%	0.5	8.22 : 4.72	6.13 : 5.24	7.67 : 5.03	13.8 : 5.00
20%	1.0	7.26 : 4.08	5.44 : 6.53	6.57 : 5.05	10.3 : 4.11
Expt.		8.75 : 4.28	9.5 : 5.05	10.83 : 4.86	10.61 : 3.93

Table 4.4 Calculated ratio $N(0^o)$: $N(180^o)$ for various forms of isotropic neutron emission, compared with experimental data. Note that the ratios are all normalized to $N(90^o)$ equal to unity.

A further form of neutron emission considered in the fragment centre of mass frame was for the first neutron emitted from each fragment to be emitted isotropically, and the n-th ($n > 1$) neutrons to be emitted anisotropically. In the simulation, the form of the anisotropy was represented by a $(1 + b \cos^2\theta)$ distribution.

A physical explanation for such a process is to consider the effect of the high initial fragment angular momentum on neutron emission. If the initial excitation energy of the fragment is sufficiently high, there will be a higher density of high spin states at accessible excitation energy in the daughter nucleus, thus enabling a high probability of isotropic neutron emission. This availability to access high spin states will decrease rapidly as the fragment excitation energy is reduced after first neutron emission. The most probable orientation of the fragment total angular momentum vector is in a plane perpendicular to the fission axis. Maximum orbital angular momentum will be removed if the neutron is emitted in a plane containing the fission axis, resulting in anisotropic neutron emission of the form described above and in equation 1.8.1.

Improvements in the fits to the n-f angular correlations were obtained for the following combinations of neutron emission:

1) Isotropic emission of scission neutrons
2) Isotropic emission of neutrons from heavy fragments
3) Isotropic emission of the first neutron emitted from light fragments.
4) Anisotropic emission of the n-th ($n > 1$) neutrons emitted from light fragments. Any value of the anisotropy parameter, b, between 0.02 and 0.10 yielded equivalent n-f angular correlations.

For the above combination a scission component of 20% with temperature T_s = 1.0 MeV produced the best χ^2 fit of 0.54. The ratio C_{n-f} $(N(0^o):N(180^o))$ for the n-f angular correlations as a function of mass division and neutron energy is presented in Table 4.5. The n-f angular correlations are also presented graphically in Figures 4.7, 4.8, 4.9 and 4.10. It can be seen that the n-f angular correlation as a function of neutron energy does not produce a particularly satisfactory correspondence with experimental data, especially in the low energy region.

En (MeV)	All light A	A = 85	A = 95	A = 105
0.5	9.21 : 4.06 (8.75 : 4.28)	5.20 : 5.08 (9.50 : 5.05)	8.97 : 4.33 (10.83 : 4.86)	13.6 : 3.41 (10.61 : 3.93)
0.5	1.04 : 0.30 (3.26 : 2.62)	0.85 : 0.28 (2.00 : 1.00)	1.15 : 0.31 (1.67 : 1.28)	0.56 : 0.20 (0.90 : 0.97)
1.0	0.50 : 2.39 (4.84 : 3.56)	0.50 : 0.42 (4.38 : 4.16)	0.41 : 2.29 (4.53 : 2.64)	0.54 : 3.03 (4.74 : 2.64)
1.5	2.95 : 5.24 (9.72 : 5.17)	0.72 : 6.78 (14.57 : 10.2)	2.31 : 5.63 (9.82 : 5.58)	7.63 : 5.79 (14.94 : 6.04)
2.0	16.1 : 7.52 (19.16 : 8.09)	7.25 : 10.1 (21.38 : 12.86)	16.2 : 9.46 (19.07 : 8.97)	26.7 : 4.67 (28.05 : 9.68)
2.5	27.8 : 8.99 (24.97 : 9.62)	13.6 : 9.48 (26.96 : 12.23)	25.7 : 10.6 (31.24 : 11.97)	41.1 : 4.25 (40.21 : 12.44)
3.0	38.4 : 9.89 (23.9 : 9.04)	20.5 : 9.04 (31.46 : 13.91)	42.1 : 11.5 (42.74 : 13.99)	40.9 : 4.78 (47.76 : 13.67)
4.0	60.6 : 10.5 (22.51 : 7.36)	28.4 : 10.6 (38.0 : 15.88)	61.9 : 11.0 (40.04 : 14.09)	72.1 : 6.33 (40.82 : 11.43)
5.0	75.9 : 9.14 (23.24 : 8.53)	83.8 : 10.7 (43.92 : 16.73)	78.3 : 6.47 (24.84 : 9.99)	52.7 : 4.44 (27.12 : 6.53)

Table 4.5 Ratio C_{n-f} (N(0°):N (180°)) produced by the Monte Carlo for a fission process with a 20 % scission neutron component (T_s = 1.0 MeV) and isotropic emission of neutrons except the n-th neutrons (n > 1) from the light fragment, which had an anisoptropy b = 0.05. Results from a simulation of 5 x 10^5 fissions. Experimentally determined values in brackets.

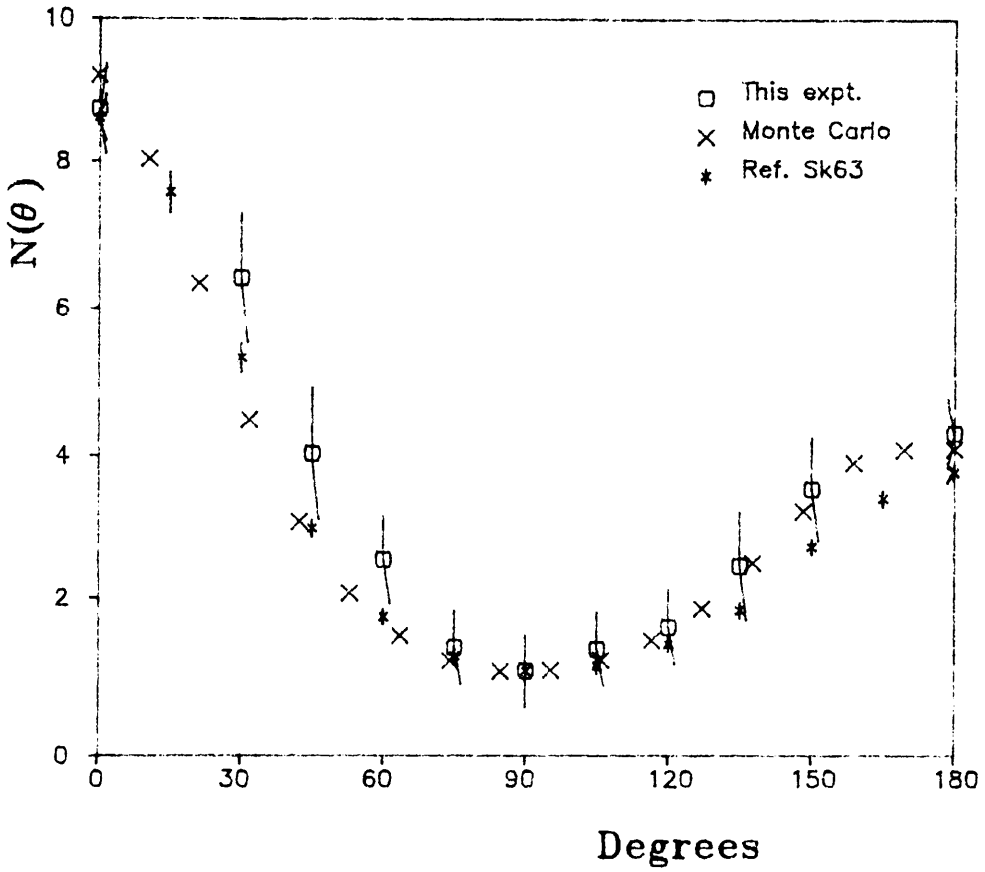

FIGURE 4.7 Simulated neutron-fragment angular correlation with respect to light fragment direction, compared with experimental data.

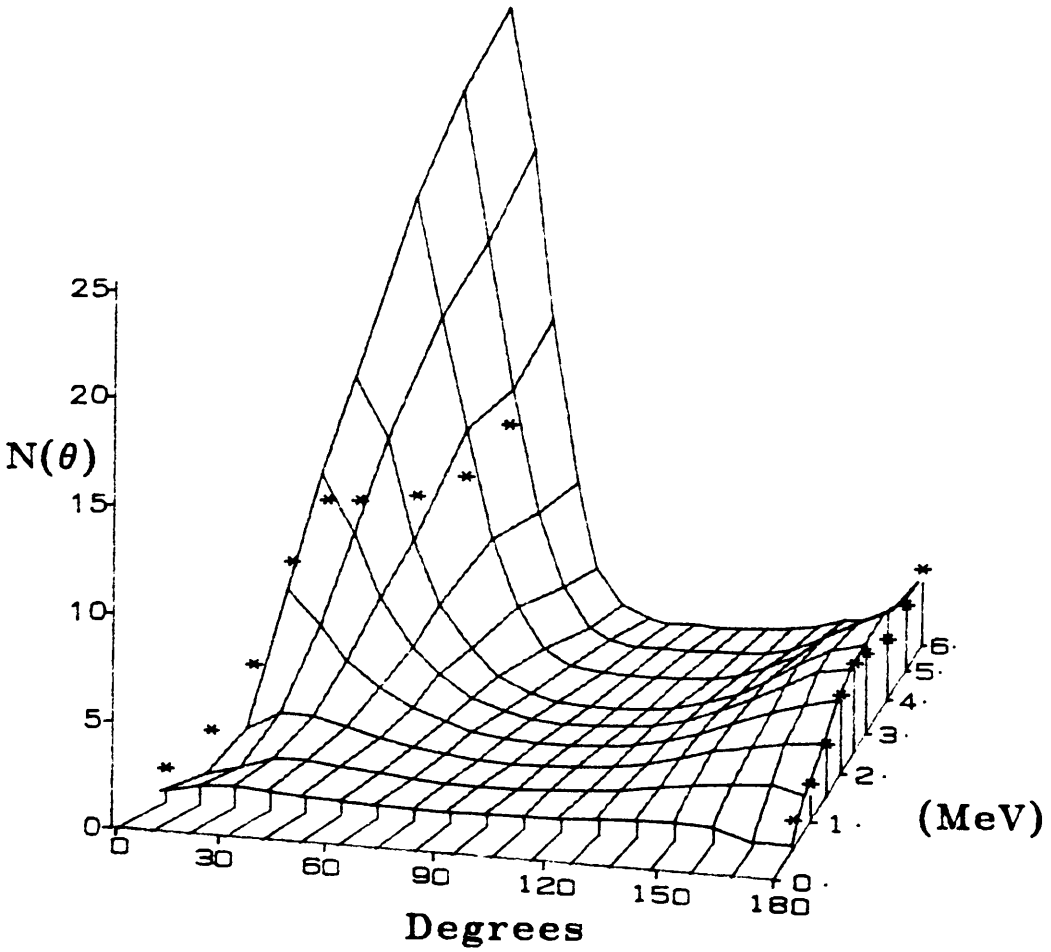

FIGURE 4.8 Simulated neutron-fragment angular correlation as a function of neutron energy and compared with results from this experiment (*).

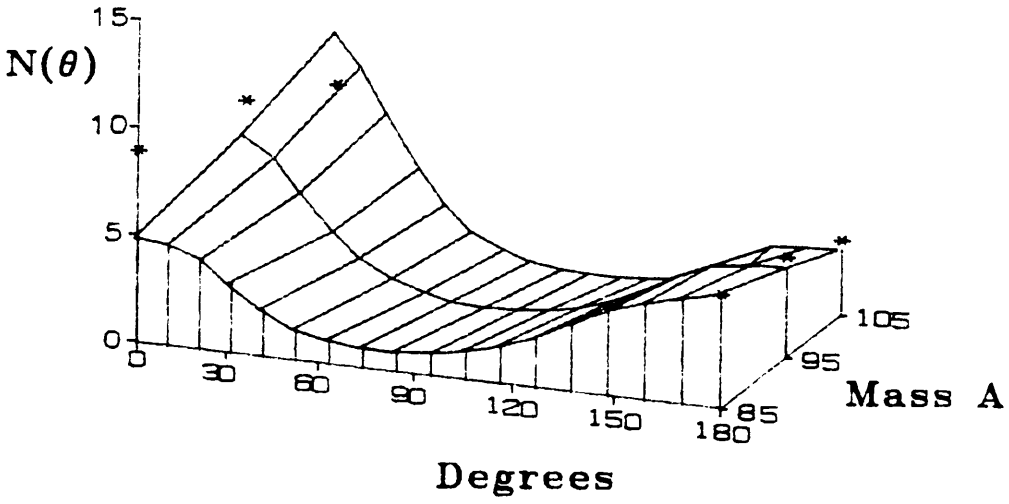

FIGURE 4.9 Simulated neutron-fragment angular correlation as a function of fragment mass division, compared with results from this experiment (*).

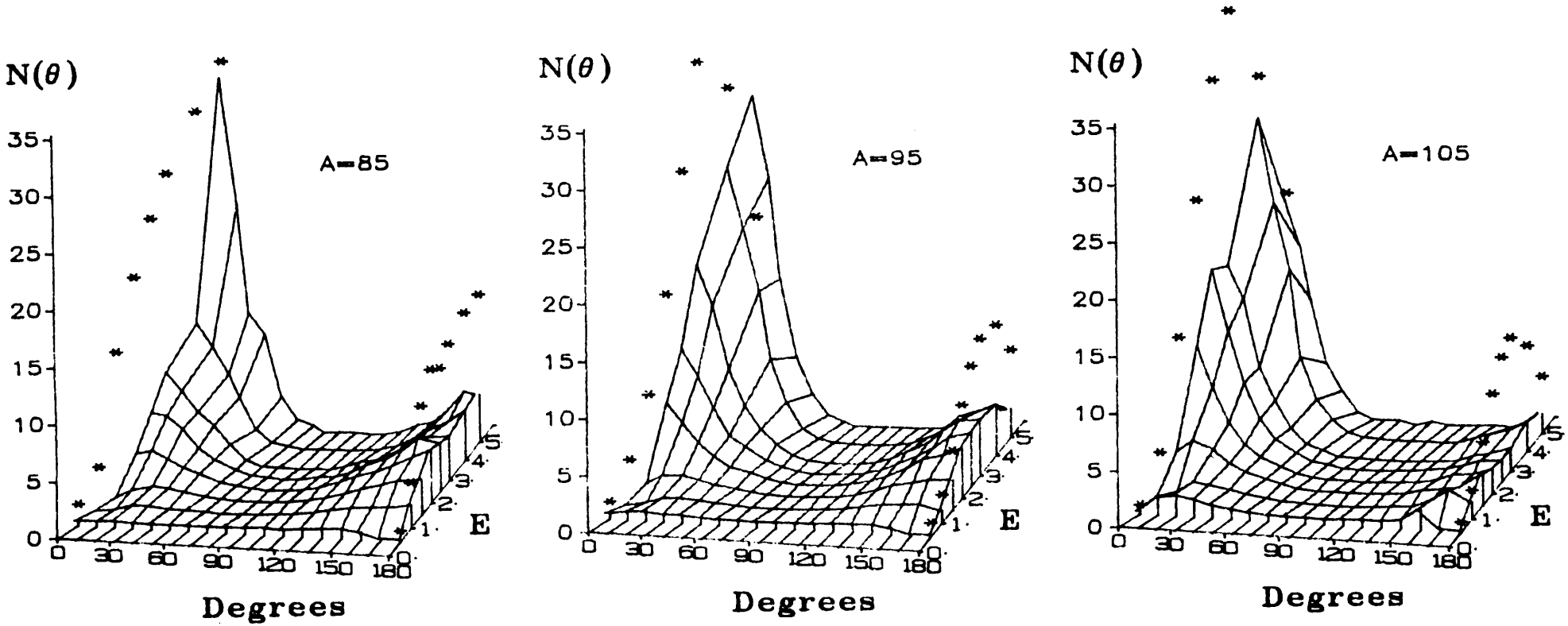

FIGURE 4.10 Simulated neutron-fragment angular correlation as a function of neutron energy for the three mass division regions, and compared with experimental results (*).

Plotting the ratio C_{n-f} as a function of neutron energy and fragment mass division and comparing with experimental data (see Figure 4.11), it can be seen that the same trend as in Figure 3.18 is apparent in the correlation, especially below 1.5 MeV, although the magnitudes are significantly different.

4.5.2 n-n angular correlations

The n-n angular coincidence rate $N_c(\Phi)$ was defined (Pr75, Fr 78) as:

$$N_c(\Phi) = \Omega_1\Omega_2\varepsilon_1\varepsilon_2 \frac{N_f\bar{\nu}P(\Phi)}{4\pi} \qquad (4.5.2)$$

where $P(\Phi)$ represents the number of fission neutrons emitted per unit solid angle at an angle Φ to, and in coincidence with, the ν-th fission neutron. N_f is the fission rate, $\bar{\nu}$ the average neutron multiplicity, Ω the detector solid angle and ε the detector efficiency. The detector singles rate of detector (1) and (2) separated by angle Φ was defined as:

$$N_a = \Omega_a \varepsilon_a \frac{N_f\bar{\nu}}{4\pi} \qquad (4.5.3)$$

where a = 1,2. A ratio was thence defined as:

$$R(\Phi) = \frac{Nc(\Phi)}{N_1N_2} = \frac{4\pi P(\Phi)}{N_f\bar{\nu}} \qquad (4.5.4)$$

Thus, experimentally, the detected rate of coincidences at angle Φ was merely divided by the singles rate of the two detectors.

Within the simple Monte Carlo simulation, outlined in section 4.2, $P(\Phi)$ was taken as the number of coincidences produced at an angle Φ between the detectors, irrespective of the fission axis orientation. This coincidence rate was taken to be proportional to $R(\Phi)$, as defined in equation 4.5.4. In the present simulation such a ratio was consistently found to be backward-peaked as a function of angle, regardless of the form of neutron emission considered in simulating the fission process. This was also the situation in the analysis of ^{252}Cf n-n angular correlation data (Pr77).

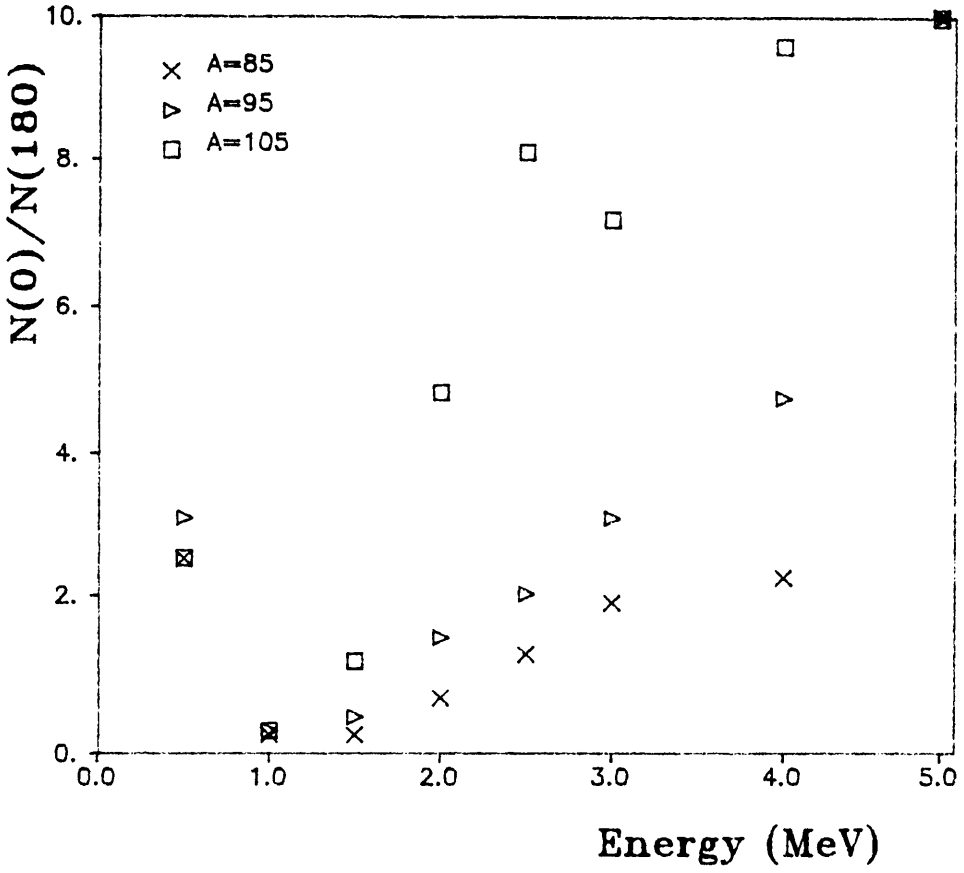

FIGURE 4.11 Variation in the ratio $N(0^{o}):N(180^{o})$ over the neutron energy range for the three mass regions. Note that the vertical scale is double that of Figure 3.18.

Upon further investigation of the procedure to simulate the n-n angular correlation it was realized that the simple equivalencing of $P(\phi)$ to $R(\phi)$ is incorrect. With respect to the Monte Carlo method equation 4.5.3 will be redefined as:

$$N_a = \Omega_a \varepsilon_a \frac{N_f}{4\pi} \sum_{\nu=1}^{6} \nu Q_\nu \qquad (4.5.5)$$

where Q_ν is the neutron multiplicity distribution and the summation is equivalent to $\bar{\nu}$, the total average neutron multiplicity. (Note that the summation is to 6, the maximum value measured (Bo67).) Similarly, the probability of a coincidence between two neutrons is redefined as:

$$N_c(\Phi) = \Omega_1 \Omega_2 \varepsilon_1 \varepsilon_2 \frac{Nf}{4\pi} \sum_{\nu=2}^{6} \frac{\nu!}{(\nu-2)!} P_\nu(\Phi) \qquad (4.5.6)$$

$P_\nu(\Phi)$ is defined as the probability distribution of observing two neutrons separated by angle Φ, and is a function of the neutron multiplicity, ν, per fission event. Note that this summation is from 2 to 6.

To simulate $P_\nu(\Phi)$ it is necessary to relate this coincidence probability distribution to the n-f angular correlation probability distribution. The n-f angular correlation with respect to the light fragment direction is defined as $W_\nu(\theta,\phi)$ where θ is the angle with respect to the light fragment direction, and ϕ describes the angle in a plane perpendicular to the fission axis. W_ν denotes the n-f angular correlation for a fission in which ν neutrons are emitted. Thus $P_\nu(\Phi)$ can be described as:

$$\frac{\nu!}{(\nu-2)!} P_\nu(\Phi) = \sum_{m=1}^{\nu-1} W_\nu(\psi m) \sum_{n=m+1}^{\nu} W_\nu(\psi n) \qquad (4.5.7)$$

where Φ is the angle between (θ_m,ϕ_m) and (θ_n,ϕ_n), and $W_\nu(\psi)$ represents the integral n-f angular correlation at θ over all angles of ϕ $(0-2\pi)$. Note that Φ is represented by:

$$\cos(\Phi) = \cos\theta_m \cos\theta_n + \sin\theta_m \sin\theta_n \cos(\phi_m - \phi_n) \qquad (4.5.8)$$

So far W has denoted the n-f angular correlation integrated over all fragment masses and neutron energies. In denoting the correlation as a function of neutron energy, e, it is necessary to bring the expression for detection efficiency, ε, within the summation expressed in 4.5.7. Thus equation 4.5.6 now becomes:

$$N_c(\Phi) = \Omega_1\Omega_2 N_f \sum_{\nu=2}^{6}\left[\sum_{m=1}^{\nu-1}\varepsilon_m W_\nu(A, e_m, \psi m) \sum_{n=m+1}^{\nu}\varepsilon_n W_\nu(A, e_n, \psi_n)\right] \qquad (4.5.9)$$

where A is the light fragment mass.

From equation 4.5.9 it can be seen that any unusual effects in the neutron emission characteristics, that is n-f angular correlations, will be smoothed out due to the multiplicative nature of the equation to establish the n-n angular correlation. Note that the precision with which tne detection efficiency is known will have a strong influence on the resultant n-n angular correlation.

Due to the aforementioned complexity of extracting an $R(\Phi)$ equivalent to the form used in the experiments, which although not insurmountable are extremely uncertain, no comparison will be made of n-n angular correlations.

5 CONCLUSION AND DISCUSSION

Results have been presented of measurements of the neutron-fragment angular correlations in thermal-neutron-induced fission of ^{235}U. The neutron-fragment angular correlations have been presented as a function of fragment mass division region and neutron kinetic energy. Such data have not been presented before for $^{235}U(n_{th},f)$. Although the accuracy of the data was severely limited by fragment mass resolution and low statistics, a positive identification was made of unusual features in the correlation data which could not be satisfactorily simulated by a simple Monte Carlo model of the fission process. Using the data acquired in this experiment and data from other experiments, a new Monte Carlo model of the fission process was developed which was considered more realistic from an energy and momentum conservation point of view. This model provided limits on the effect of isotropic and anisotropic emission of neutrons at scission and from fission fragments during and after full fragment acceleration.

By comparing the n-f angular correlation experimental data with Monte Carlo predictions over various fragment mass division regions, it was possible to differentiate, quite distinctly, between candidate modes of neutron emission that produced similar mass-averaged n-f angular correlations. The effect of the following modes of neutron emission upon the simulation of n-f angular correlations was investigated:

1) Isotropic and/or anisotropic emission from fully accelerated fragments
2) Isotropic and/or anisotropic emission during fragment acceleration
3) Isotropic and/or anisotropic emission from a frame at rest in the laboratory

and for any combination of the above modes.

The mode of neutron emission with the best χ^2 fit, indicated by the Monte Carlo, was for fission in which 20% of the neutrons emitted originated isotropically from a source at rest in the laboratory frame,

that is, scission neutrons. The energy distribution of these neutrons was best characterized by a Maxwellian distribution with a temperature of 1.0 MeV. The remaining neutrons were emitted from fully accelerated fragments, those from the heavy fragment (a predominantly spherically shaped nucleus) being emitted isotropically in the fragment frame of reference. Neutrons emitted by the light fragment centre-of-mass (a predominantly deformed nucleus at scission) were emitted isotropically for first neutron emission and anisotropically for further neutrons. The anisotropy was described by a $1+b\cos^2\theta$ form with b = 0.02 to 0.10, where $\theta = 0^o$ defines the fission axis.

Existing uncertainties about the division of residual fragment excitation energy between the fission fragments and the form of the scission neutron energy distribution, precluded the necessity to pursue further investigation of neutron emission during fragment acceleration. It is not ruled out that there is in fact emission during fragment acceleration, but in a form more complex than was treated in this work.

Other factors which may have a strong influence on the form of neutron emission were:

1) The effect of angular momentum on neutron emission. A situation was not simulated in which γ-rays were emitted before last neutron emission.

2) The effect of ternary fission, which, although occurring in less than 2 % of fissions, may still be sufficient to affect the angular correlation characteristics.

3) The manner in which excitation energy is shared between the fragments depending on whether a scission neutron has or has not been emitted. This may have an adverse effect. This was most evident when the scission-neutron Maxwellian temperature was sampled at 0.5 MeV.

The method of simulating the fission process highlighted an area of uncertainty where unusual effects could be taking place in the compound nucleus, namely the level density at the very high deformations and high angular momentum prevalent in the fission process. Fluctuations in these parameters would be more apparent if the situation of an extended time delay for the nucleus in its transition from saddle-to-scission point holds true.

It is of interest to note the preliminary results of studies of neutron rich nuclei at the Nuclear Structure Facility, Daresbury, UK. Observations (Ce86) of γ-rays indicate that sudden transitions from prolate to oblate to super-prolate shapes occur in nuclei with very high spin. This would imply considerable fluctuations in level spacings and thus have a considerable effect on neutron transition probabilities.

It has been demonstrated that various types of neutron emission processes yield similar n-f angular correlations, as a function of light fragment direction, to experimental data. It has also been shown that extending comparisons, between experimental data and theoretical predictions, of the n-f angular correlation as a function of fragment-mass division and neutron energy illustrates the necessity of such measurements in order to identify the most likely forms of neutron emission occurring in fission.

Further measurements of n-f angular correlation as a function of individual fragment-mass division and neutron energy in various fissioning nuclei will enable more accurate comparisons to be made with Monte Carlo predictions. Such data are being acquired for ^{252}Cf (s.f.) (Bu85), but this is an extremely time consuming process due to the large number of events required to provide statistical significance.

APPENDIX A

MEASUREMENT OF THE SPATIAL DISTRIBUTION OF URANIUM ON A THIN TARGET FOIL BY EXTERNAL BEAM PIXE ANALYSIS

Measurement of the spatial distribution of uranium on a thin target by external beam PIXE analysis

Particle-induced X-ray emission (PIXE) analysis has, since its inception (Jo70), established itself as a widely used, routine method of analysis, in particular for thin layer samples. The availability of small beam spot sizes and precise positioning of the target enables spatial distributions of elements to be determined.

Experiment

Due to the larger than typical target size which could not be accommodated in a suitable facility in vacuo, an external beam facility at the AEC Van de Graaff accelerator, shown in Figure A.1, was used in these measurements. A 3 MeV proton beam, collimated by using 1.0 mm and 0.4 mm carbon collimators, passed through a 25 μm thick beryllium window into air, to produce a 1.1 mm or 0.5 mm (FWHM) beam spot on the target. The actual target spot size was slightly larger than collimated due to window and air scattering, with a halo of typically 0.5 mm size detected. In passing through the beryllium window, the proton beam was degraded by 480 keV, and by a further 150 keV in passing through the 12 mm of air between the exit window and the target plane. The resultant target beam energy of 2.37 MeV was appropriate for the measurements undertaken. Under normal circumstances, in order to reduce the component of X-rays emanating from argon, the immediate area of the target and detector is usually kept flushed with a stream of helium gas. However, in this case, the extreme delicacy of the fission foil precluded such operation.

The target was mounted on an aluminium block on a vertically mounted X-Y translational table, with a position accuracy of $\pm$0.1 mm, at an angle of 30^{o} to the beam direction. A 3 mm depletion depth, 100 mm^2, intrinsic germanium detector viewed the target spot via a tapered aluminium collimator at an angle of 135^{o} to the beam as shown diagramatically in Figure A.2. Beam spot size and profile were determined by stretching a 10 μm tungsten wire across the target area and scanning the X-ray yield in 0.1 mm steps. The result of this measurement is shown in Figure A.3.

The foil studied had a nominally uniform 20 μg cm^{-2} layer of gold deposited over it. This served as a useful standardizing feature to check that beam current integration was operating correctly. A further beam normalizing

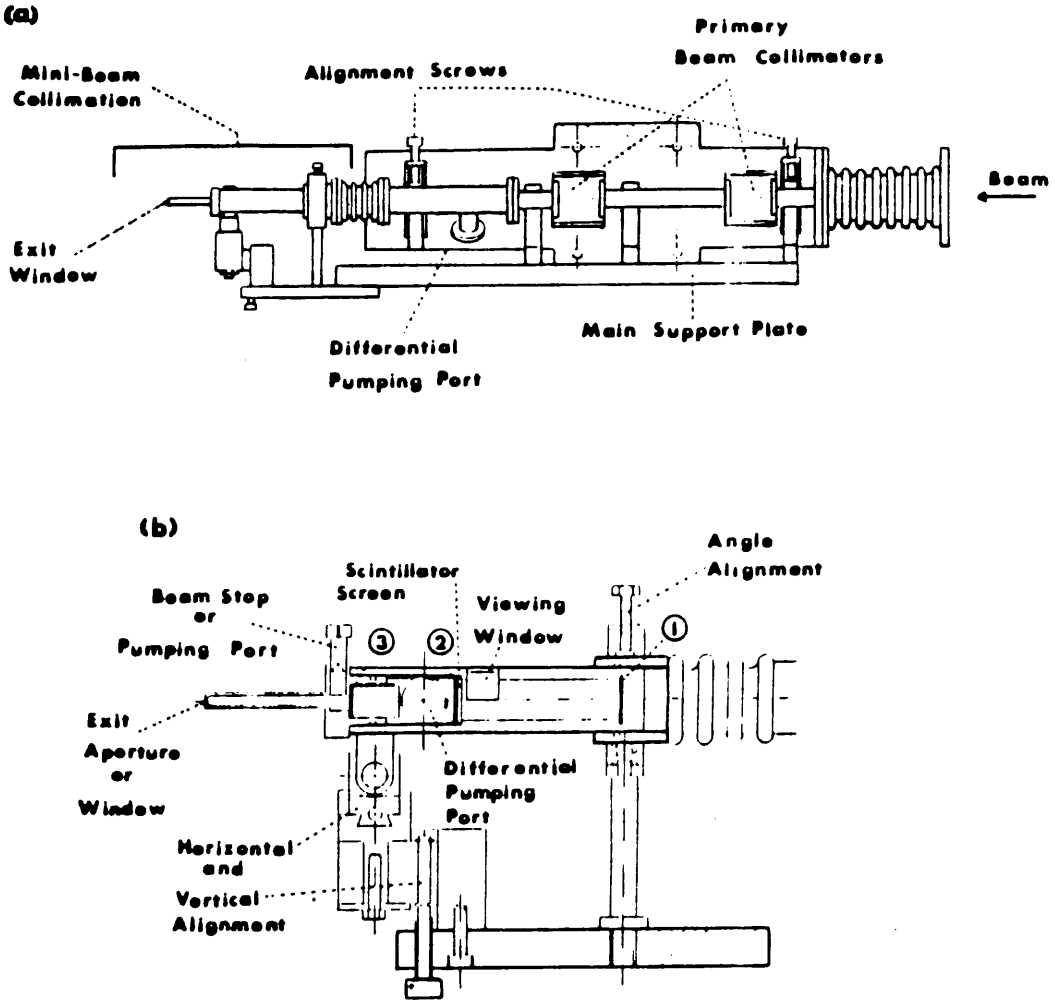

FIGURE A.1 External beam facility of the AEC Van de Graaf, illustrating a) the primary collimation and b) the exit window area.

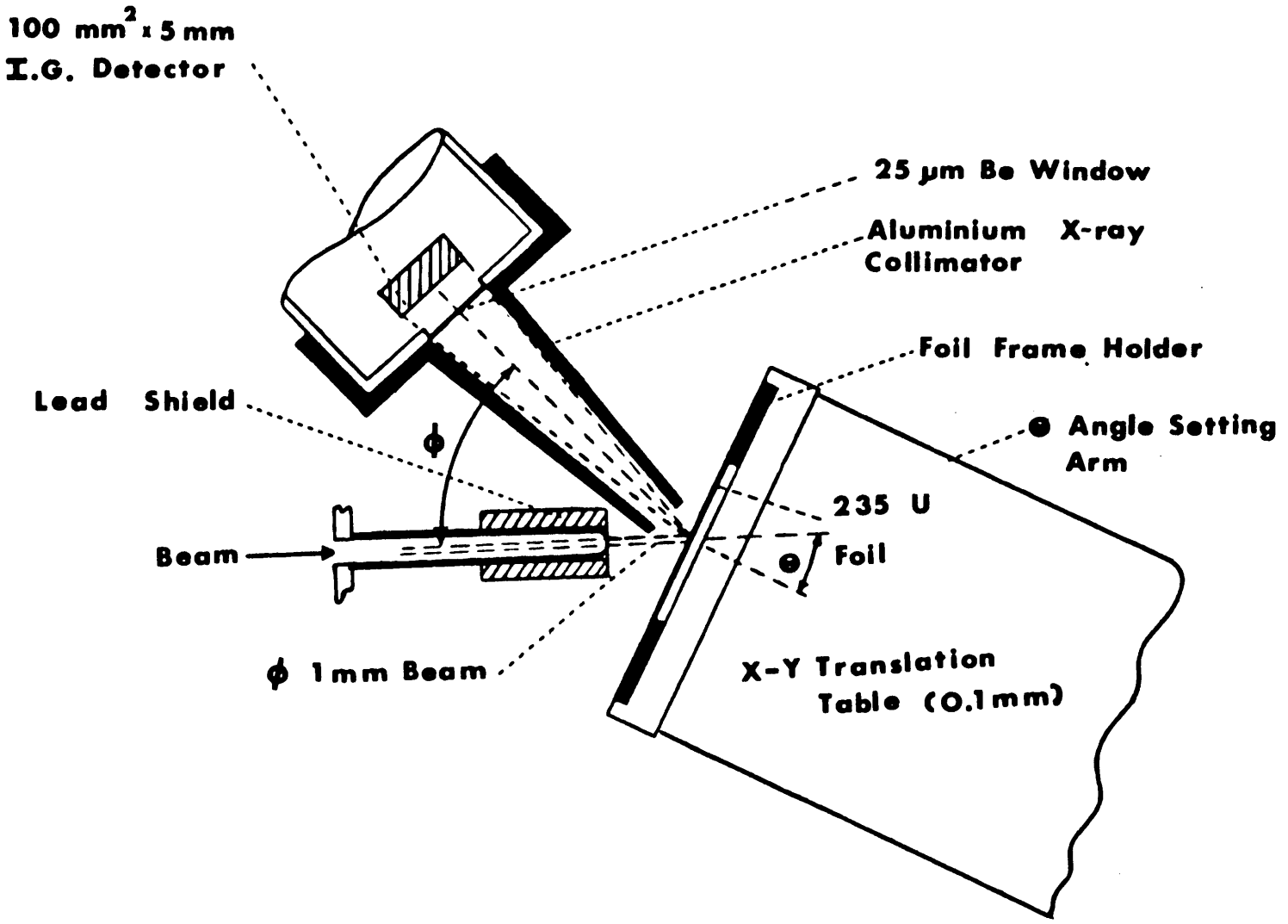

FIGURE A.2 Target and detector area arrangement used for these measurements.

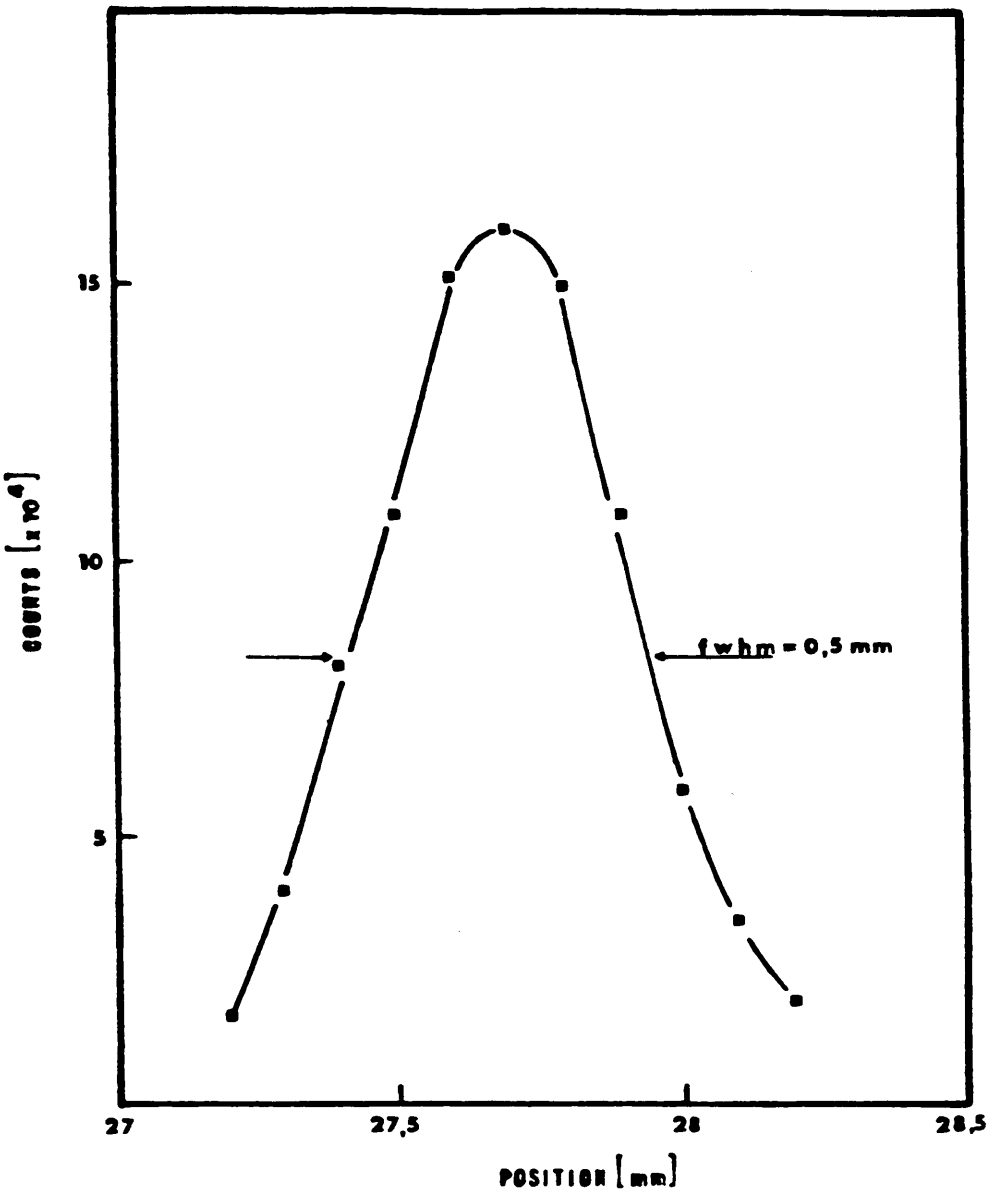

FIGURE A.3 Measured beam profile from a scan of a 10 μm tungsten wire using a 0.4 mm carbon collimator.

parameter was the detected iron contamination of the aluminium block onto which the target was mounted. The system was calibrated using a uranium standard sample of 66.2 μg cm^{-2} and a gold standard sample of 104 μg cm^{-2}, both of which had been previously calibrated by Rutherford scattering (M183).

Typical beam currents of 1 nA were used and spectra recorded for 100 nC. A typical energy spectrum recorded in two minutes by the detector is shown in Figure A.4. The uranium X-rays, $L\beta_1$ = 17.2 keV, $L\beta_2$ = 16.4 keV, $L\alpha$ = 13.5 keV (13.4+13.6), $M\alpha_1 + \alpha_2$ = 3.2 keV are well defined. Also clearly defined are the $L\alpha$ X-rays, 9.6 & 9.7 keV, from the gold layer, as well as a mixture of U_L and Au_L X-rays at 11.6 keV. The intensity of the gold X-rays indicating a nominal thickness of 18 μg cm^{-2}. Other than the iron contamination (K_α = 6.4, K_β = 7.1 keV) in a localized area of the aluminium block, no other contaminants were observed.

Results

The distribution of uranium in several scans of 1 mm step size (1 mm resolution) is shown in Figure A.5. These results indicate that the uniformity is limited to within ± 30 % of the average value, which was determined to be 800 ± 20 μg cm^{-2} from a series of scans covering 40 % of the foil surface area. This average value compares well with the quoted thickness by the supplier of 870 μg cm^{-2} on an absolute scale, but in no way confirms the quoted uniformity of ± 10 %.

Selected areas of the foil were scanned using a collimated beam spot size of 0.5 mm in 0.5 mm steps. The typical variation in the concentration of uranium at this resolution is illustrated in Figure A.6. In these measurements a deviation of 50 % from average value is observed. Considerably larger excursions may be expected on an even smaller scale as implied by optical transmission surveys of the foil.

Although the total surface area of uranium concentration in excess of 30 % from average value is estimated to be less than 3 %, the effective increased thickness in this region means that the fission rate from this region will represent up to 10 % of the observed fission events. Such a result was predicted by Monte Carlo calculations of the fission rate and fragment energy

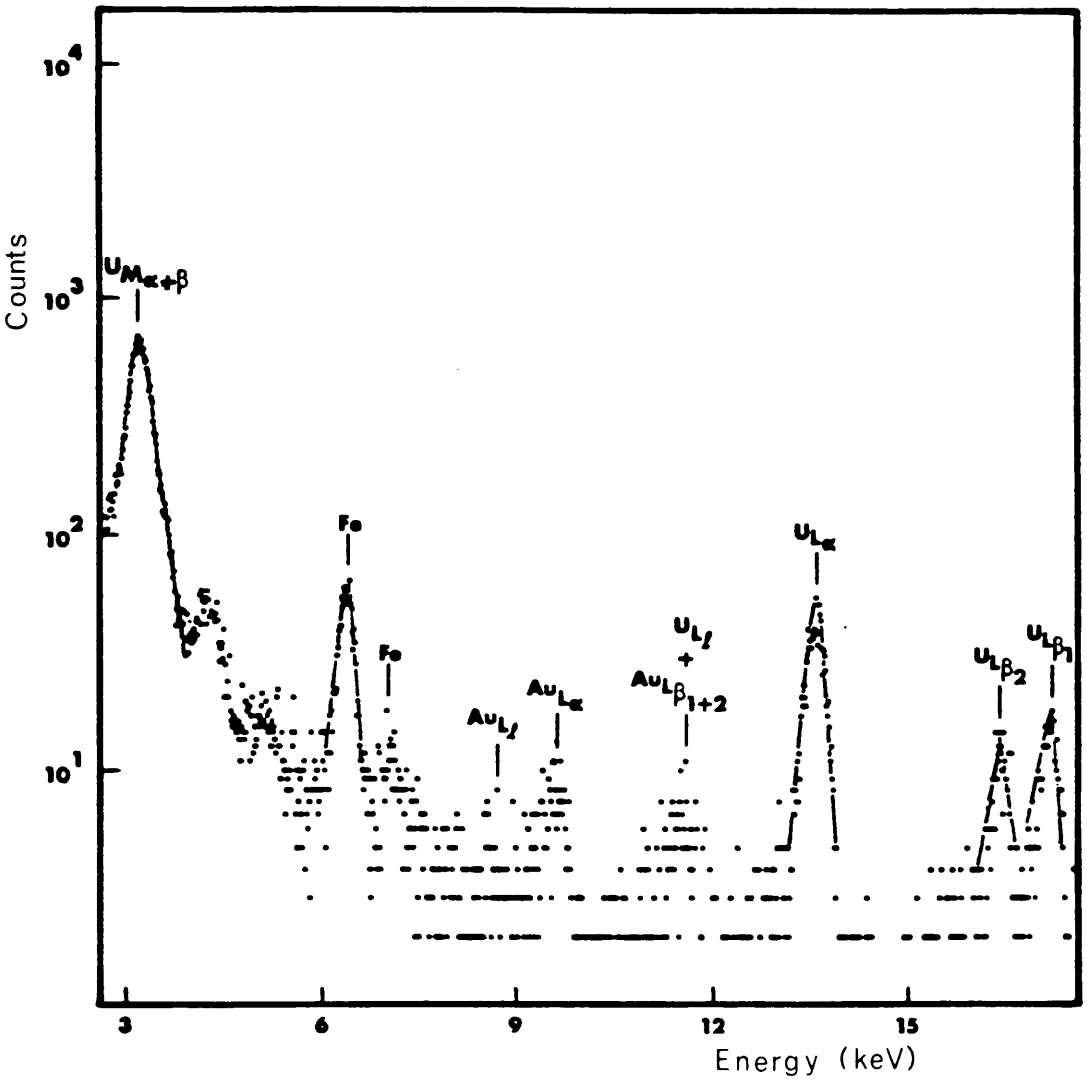

FIGURE A.4 Typical energy spectrum recorded, illustrating the uranium and gold X-rays from the foil and the iron X-rays from the aluminium block supporting the target.

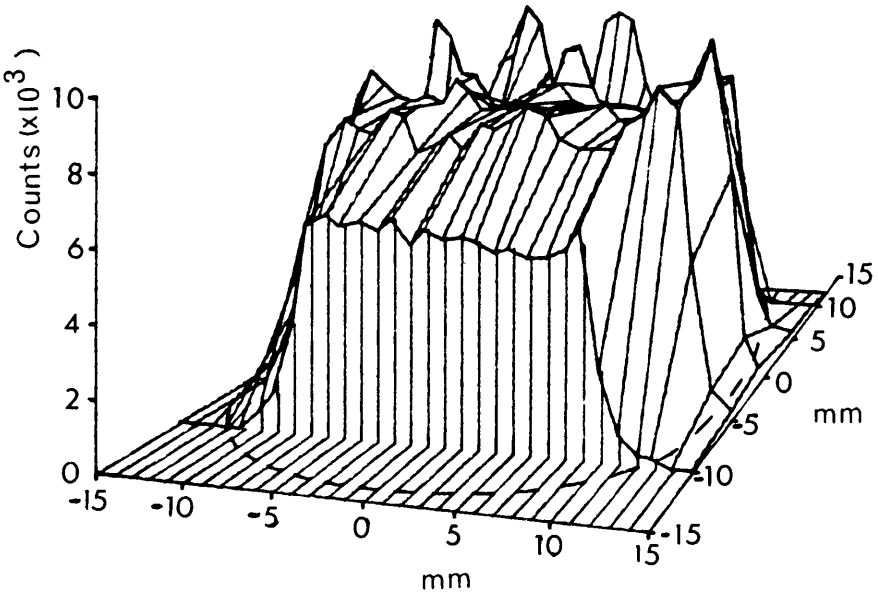

FIGURE A.5 Isometric plot of the uranium distribution for several scans of 1.1 mm resolution. The dashed line illustrates the edge of the foil deposition.

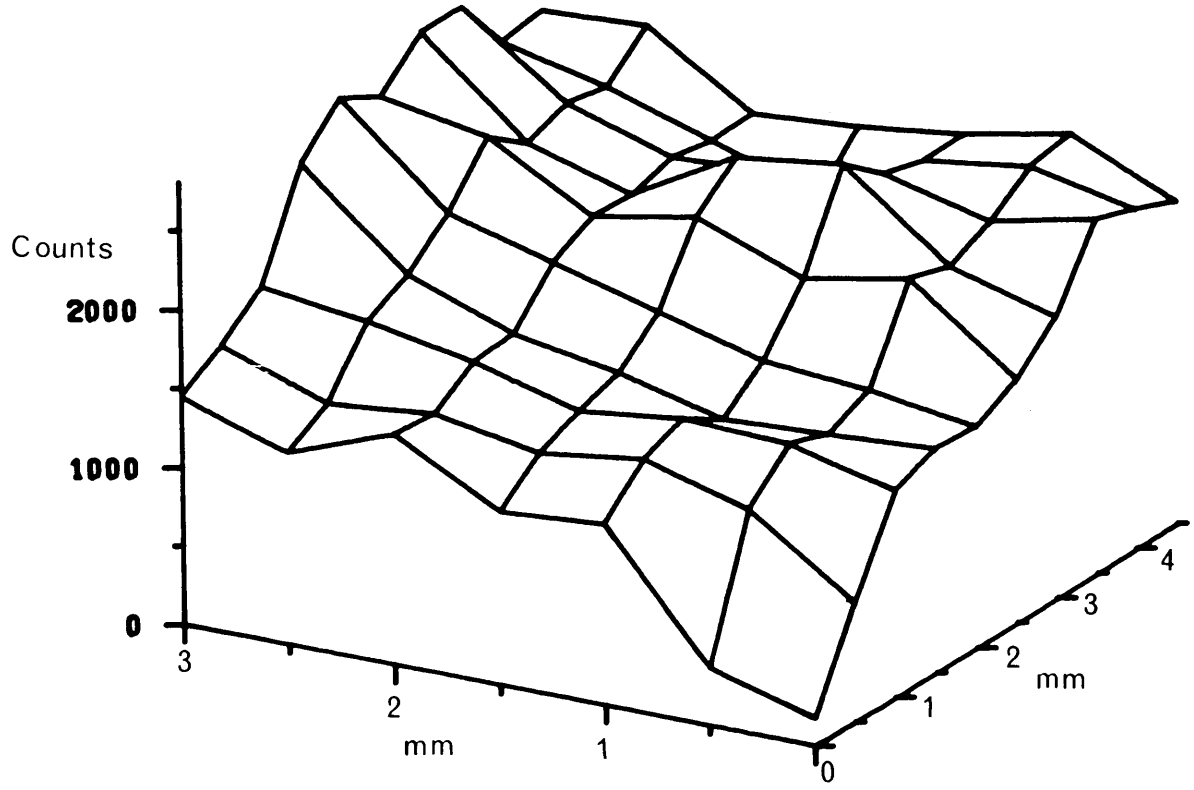

FIGURE A.6 Uranium distribution for a selected area of the foil, for 0.5 mm beam spot resolution. The point 0 represents the edge of the foil.

degradation of an inhomogeneous foil. Due to energy degradation the time-of-flight (TOF) difference of correlated fission fragments will become distorted, as is illustrated in a series of plots in Figure A.7 for a) a homogeneous 1 mg cm^{-2} foil, b) a foil with thickness varying between 0.5 and 2.0 mg cm^{-2} and naving a mean thickness of 1 mg cm^{-2}, and c) the actual foil used. The fact that the experimental data is even more distorted than the prediction for case (b) is partly due to dispersion effects of the timing signals but may also be partly caused by locations of the foil having even greater thickness than 2.0 mg cm^{-2}. A foil with regions as thick as 4 mg cm^{-2}, average thickness 1 mg cm^{-2}, could completely duplicate the experimental TOF plot .

Conclusion

External beam PIXE measurements have been used successfully to characterize the spatial distribution of a uranium fission target foil deposited over a 25 mm diameter area. It has been demonstrated that the average non-uniformity of the foil was $\pm$ 30 %, with some locations indicating greater than average thickness of more than 50 %. While a complete scan on a finer mesh with considerably better spatial resolution would be demanded for complete definition of the target homogeneity, the measurements made were sufficient to allow a meaningful simulation to be made of the fission fragment energy distributions to be expected as emanating from the foil following thermal-neutron-induced fission.

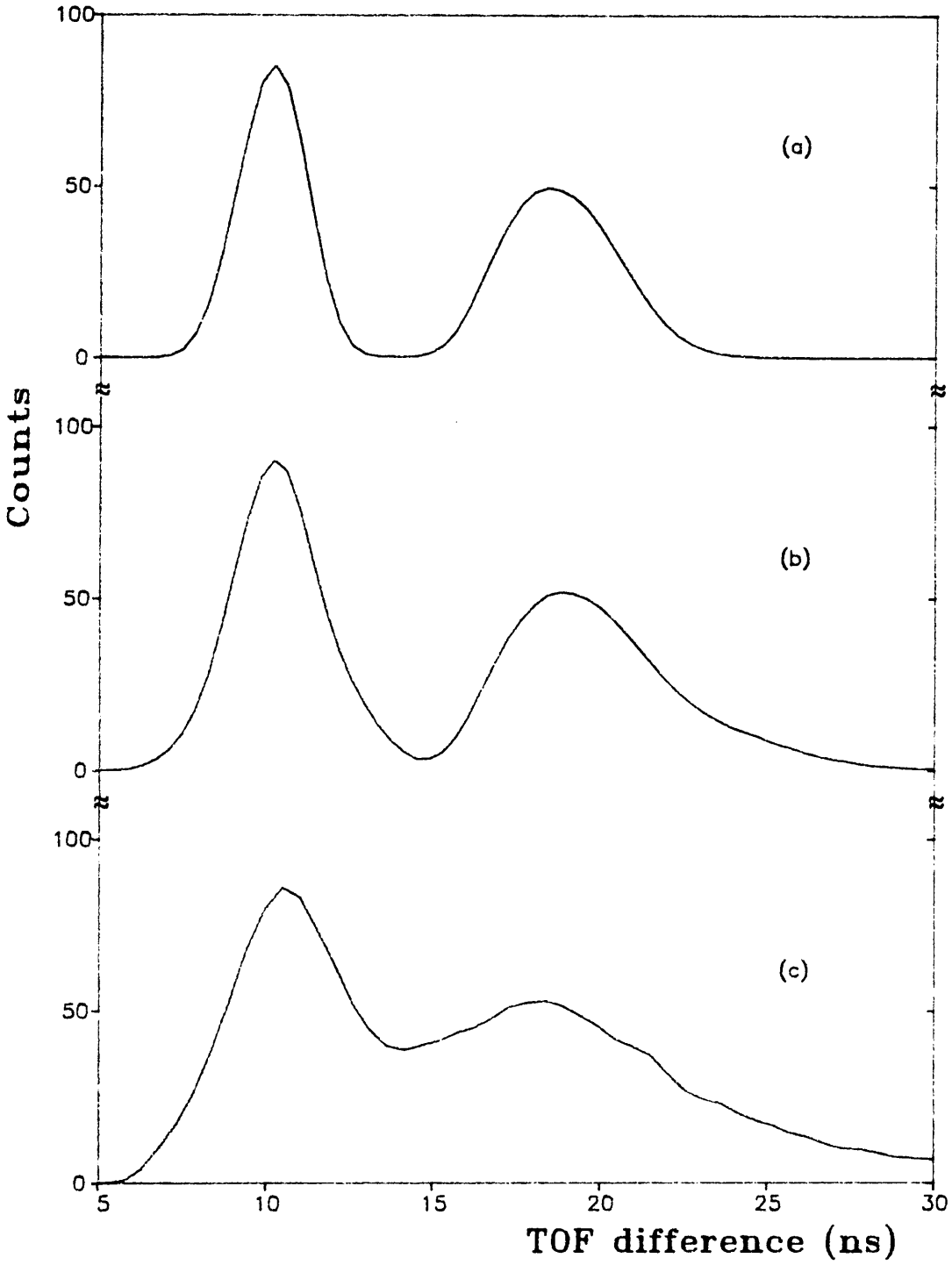

FIGURE A.7 Time-of-flight difference between fission fragments emitted from the target foil a) calculated for a uniform 1 mg cm^{-2} foil, b) calculated for an inhomogeneous foil of thickness between 0.5 and 2.5 mg cm^{-2} and average thickness 1 mg cm^{-2}, and c) measured. Note that the calculations assumed ideal timing resolution.

APPENDIX B

EXPERIMENTAL RESULTS OF NEUTRON-FRAGMENT ANGULAR CORRELATIONS

Angle	0°	30°	45°	60°	75°	90°	105°	120°	135°	150°	180°
N	8.75	6.42	4.00	2.54	1.33	1.00	1.30	1.61	2.45	3.51	4.28
dN	.62	.90	.91	.60	.51	.50	.51	.52	.74	.71	.48

TABLE B.1 n-f angular correlation with respect to light fragment direction for all fragment mass divisions, and neutron energies ≥ 0.5 MeV.

E_n (MeV)	Angle	0°	30°	45°	60°	75°	90°	105°	120°	135°	150°	180°
.5	N	3.26	3.40	3.30	3.03	2.09	1.00	1.76	1.66	2.44	2.75	2.62
	dN	.47	.90	1.02	.82	.79	.71	.69	.77	.88	.83	.43
1.0	N	4.84	5.97	4.12	2.62	1.44	1.00	1.62	1.69	2.61	3.51	3.56
	dN	.59	.86	.78	.51	.40	.55	.54	.35	.68	.60	.48
1.5	N	9.72	8.02	4.50	2.55	1.16	1.00	1.38	1.69	3.00	4.39	5.17
	dN	1.01	.89	.85	.40	.31	.32	.29	.35	.59	.54	.56
2.0	N	19.16	11.86	6.31	3.29	1.39	1.00	1.06	2.68	3.81	6.35	8.09
	dN	1.09	1.10	.89	.32	.28	.33	.34	.34	.78	.63	.84
2.5	N	24.97	15.06	8.65	3.90	1.62	1.00	1.11	2.20	4.10	7.36	9.62
	dN	1.44	1.24	1.47	.73	.70	.45	.30	.70	.85	1.35	1.06
3.0	N	23.90	14.83	7.18	3.53	1.20	1.00	1.05	2.18	2.04	3.64	9.04
	dN	.25	.40	.30	.40	.40	.35	.30	.30	.23	.22	.21
4.0	N	22.51	13.45	7.36	3.21	1.14	1.00	1.28	1.62	2.79	5.43	7.36
	dN	.36	.82	.55	.37	.12	.21	.27	.17	.47	.48	.20
5.0	N	23.24	15.56	8.13	3.75	0.76	1.00	0.46	1.96	4.44	6.34	8.53
	dN	.41	1.22	.49	.55	.23	.23	.22	.24	.59	0.40	.25
6.0	N	29.00	13.45	6.65	2.05	0.63	1.00	1.00	1.38	1.48	3.65	10.65
	dN	.66	1.28	.92	.50	.20	.31	.41	.22	.65	.40	.26

TABLE B.2 n-f angular correlation with respect to light fragment direction as function of neutron energy, for all fragment mass divisions.

Light mass	Angle	0°	30°	45°	60°	75°	90°	105°	120°	135°	150°	180°
85	N	9.50	5.83	3.69	2.99	1.70	1.00	0.75	1.47	2.66	4.12	5.05
	dN	0.20	0.37	0.20	0.13	0.10	0.08	0.06	0.08	0.15	0.17	0.13
95	N	10.83	6.72	4.33	2.90	1.73	1.00	0.86	1.69	2.46	3.86	4.86
	dN	0.17	0.33	0.22	0.12	0.07	0.07	0.04	0.07	0.12	0.17	0.10
105	N	10.61	7.26	4.02	1.85	0.85	1.00	1.55	1.88	2.00	2.63	3.93
	dN	0.16	0.28	0.22	0.09	0.03	0.05	0.06	0.07	0.11	0.14	0.08

TABLE B.3 n-f angular correlation as a function of light fragment direction for all neutron energies for specific mass regions.

Angle	En (MeV)	0.5	1.0	1.5	2.0	2.5	3.0	4.0	5.0
0°	N	2.00	4.38	14.57	21.38	26.96	31.46	38.00	43.92
	dN	0.07	0.10	0.22	0.74	0.95	0.63	4.16	2.37
30°	N	1.96	6.23	9.47	11.87	13.61	14.88	16.59	18.14
	dN	0.09	0.16	0.57	1.06	2.44	0.58	4.72	5.01
45°	N	2.41	4.48	5.67	6.27	6.57	6.77	7.58	9.58
	dN	0.07	0.15	0.45	0.88	0.71	0.23	3.30	2.20
60°	N	2.23	3.62	4.36	4.65	4.69	4.61	4.58	5.17
	dN	0.03	0.10	0.15	0.28	0.49	0.22	2.46	0.89
75°	N	1.69	2.14	2.16	2.38	2.60	2.41	2.60	3.50
	dN	0.09	0.10	0.08	0.31	0.64	0.53	0.30	0.60
90°	N	1.00	1.00	1.00	1.00	1.00	1.00	1.00	1.00
	dN	0.03	0.04	0.04	0.16	0.30	0.27	0.28	0.40
105°	N	0.73	0.71	1.37	1.44	0.89	0.45	1.75	1.33
	dN	0.02	0.02	0.02	0.12	0.32	0.25	0.28	0.60
120°	N	1.34	1.69	1.85	1.93	2.01	2.12	2.60	3.33
	dN	0.05	0.10	0.06	0.17	0.24	0.35	0.40	0.96
135°	N	2.17	3.49	4.16	4.35	4.10	3.87	3.87	4.90
	dN	0.02	0.17	0.29	0.41	0.89	0.28	2.21	1.00
150°	N	2.47	5.45	7.05	7.67	7.65	7.30	6.56	6.98
	dN	0.02	0.15	0.28	0.75	0.55	0.17	3.61	1.00
180°	N	1.00	4.16	10.20	12.86	12.23	13.91	15.88	16.73
	dN	0.03	0.06	0.20	0.48	0.72	0.17	2.30	1.36

TABLE B.4 n-f angular correlation as function of neutron energy for mass regio
A = 85

Angle	En (MeV)	0.5	1.0	1.5	2.0	2.5	3.0	4.0	5.0
0°	N	1.67	4.53	9.82	19.07	31.24	42.74	40.04	24.84
	dN	0.01	0.05	0.16	0.45	0.72	0.36	0.71	0.68
30°	N	2.39	4.47	7.69	11.19	14.29	16.51	17.31	13.64
	dN	0.02	0.17	0.31	0.83	1.06	0.30	0.95	1.31
45°	N	2.59	3.35	4.66	6.21	7.74	8.93	8.72	6.21
	dN	0.02	0.17	0.16	0.56	0.71	0.28	0.72	0.40
60°	N	2.47	2.18	2.47	3.30	4.34	5.22	5.35	3.18
	dN	0.03	0.09	0.15	0.24	0.51	0.06	0.17	0.33
75°	N	2.18	1.43	1.26	1.45	1.78	2.06	2.07	1.31
	dN	0.02	0.05	0.08	0.15	0.34	0.01	0.11	0.21
90°	N	1.00	1.00	1.00	1.00	1.00	1.00	1.00	1.00
	dN	0.02	0.04	0.04	0.11	0.11	0.02	0.07	0.08
105°	N	0.42	1.45	1.36	0.91	0.55	0.47	1.09	0.50
	dN	0.02	0.06	0.03	0.13	0.10	0.01	0.22	0.21
120°	N	1.57	1.35	1.63	2.07	2.44	2.62	2.26	1.27
	dN	0.02	0.04	0.11	0.25	0.26	0.02	0.15	0.15
135°	N	1.75	2.02	2.69	3.48	4.18	4.62	4.45	2.90
	dN	0.01	0.11	0.17	0.40	0.27	0.15	0.29	0.20
150°	N	2.00	3.30	4.74	6.05	7.02	7.52	6.99	4.85
	dN	0.02	0.11	0.14	0.63	0.72	0.26	0.40	0.48
180°	N	1.28	2.64	5.58	8.97	11.97	13.99	14.09	9.99
	dN	0.01	0.05	0.10	0.32	0.35	0.14	0.31	0.40

TABLE B.5 n-f angular correlation as a function of neutron energy for mass region A = 95.

Angle	En (MeV)	0.5	1.0	1.5	2.0	2.5	3.0	4.0	5.0
0°	N	0.90	4.74	14.94	28.05	40.21	47.76	40.82	27.12
	dN	0.07	0.05	0.26	0.52	0.76	0.39	1.00	1.32
30°	N	2.34	6.28	11.28	15.94	19.20	20.48	17.17	10.48
	dN	0.04	0.17	0.48	0.73	2.14	0.35	1.33	1.12
45°	N	2.16	3.72	5.67	7.52	8.84	9.36	7.84	4.44
	dN	0.02	0.09	0.41	0.75	0.54	0.70	1.13	1.87
60°	N	1.09	1.91	2.67	3.22	3.51	3.50	2.74	1.52
	dN	0.02	0.07	0.17	0.33	0.38	0.20	0.41	0.53
75°	N	0.72	0.78	0.94	1.13	1.26	1.31	1.08	0.80
	dN	0.04	0.02	0.08	0.08	0.18	0.02	0.06	0.11
90°	N	1.00	1.00	1.00	1.00	1.00	1.00	1.00	1.00
	dN	0.01	0.03	0.04	0.07	0.09	0.03	0.05	0.09
105°	N	1.35	1.87	1.73	1.83	2.00	1.78	1.50	1.50
	dN	0.01	0.07	0.08	0.36	0.17	0.02	0.08	0.11
120°	N	1.21	2.25	2.78	2.87	2.68	2.39	1.86	1.35
	dN	0.02	0.06	0.19	0.24	0.26	0.03	0.06	0.42
135°	N	0.65	2.21	3.11	3.78	4.82	5.63	1.80	2.50
	dN	0.01	0.09	0.26	0.23	0.44	0.24	0.58	0.67
150°	N	1.24	2.68	4.29	5.70	6.57	6.70	4.81	2.00
	dN	0.02	0.10	0.18	0.73	1.21	0.11	0.33	0.29
180°	N	0.97	2.64	6.04	9.68	12.44	13.67	11.43	6.53
	dN	0.01	0.03	0.13	0.32	0.44	0.15	0.46	0.47

TABLE B.6 n-f angular correlation as a function of neutron energy for mass region A = 105

APPENDIX C

LISTING OF COMPUTER PROGRAM FOR SIMULATING THE FISSION PROCESS

```
FTN4X,L
$EMA(FIJI,0)
      PROGRAM FRIJN(), REV (860620.1637)
C
C       This program simulates the fission process for 235U(nth,f)
C       Also simulated is the emission of neutrons but not their
C       angular distribution, which is done afterwards.
C
      COMMON/FIJI/JAB(100,400)
      LOGICAL TAPE,LHVY,ITRU,SCIS
      DIMENSION IC(72),NUM(10),IZ(85),PR(256),IP(84)
      DIMENSION BEN(20),BE(84,20),A(83,12)
      DIMENSION EN(10),ENL(10),ID(128),IDCB(144)
      DATA NUM/1H0,1H1,1H2,1H3,1H4,1H5,1H6,1H7,1H8,1H9/
C
C****** Starting value of charge in look-up tables
C
      DATA IZ/30,30,30,31,32,32,32,33,34,34,34,35,35,36,36,36,37,37,
     138,38,38,39,39,40,40,40,40,41,42,42,42,42,42,42,43,43,43,44,44,44,
     245,45,45,47,47,48,48,48,49,49,49,50,50,50,50,50,50,51,52,52,52,52,
     353,53,54,54,54,55,55,56,56,56,57,57,58,58,58,59,60,60,60,61,62,62,
     462/
      ANEVT=100000.                    ! Events to be simulated
      LDA=7                            ! LU of look-up tables
      LUR=1
      LU=LOGLU(LUR)                    ! Terminal LU
      NSC=0                            ! Scission compt. mode, 1=yes
      IF(NSC.EQ.1)THEN
      SCC=0.7                          ! Fraction of nu-bar as scission comp
      TSC=1.0                          ! Maxwellian temp. of scission compt.
      ENDIF
      NOV1=0
      ISS=0
C
      CALL BERG(IP,BE,IDCB,ID)         ! read in binding energy data
C
      CALL ALDP(IZ,A)                  ! compute level density parameter, a
C
      R0=.12345                        ! initialize random number generator
      ANEV=0.
10    IF(ANEV.GE.ANEVT)GO TO 999       ! start of main loop
      ANEV=ANEV+1.
C
11    CALL FRANZ(ML,KZL,R0)            ! select mass and charge
C
      MH=82-ML
      KZH=92-KZL
C
      CALL BENIN(ML,KZL,IP,BEN,BE) ! read in B.E. of M to M-9
C
      BELF=BEN(10)                     ! fragment binding energies
      BELH=BEN(20)
      IF(BELF.LT.1..OR.BELH.LT.1.)GO TO 11
      EREM=BELF+BELH-1783.89           ! energy to spare
      IF(EREM.LT.0.01)GO TO 11
      MLS=0
      MHS=0
      SCIS=.FALSE.
C
      CALL FENG(ML,EL,EH,KZL,EREM,R0)    ! fragment kinetic energy
```

```
C                                                    C2
      IF(EREM.LT.0.001)GO TO 11
      IF(NSC.EQ.1)THEN                 ! Scission neutron emission
      CALL RANDY(R0,RS,RE)
      IF(RS.LT.SCC)THEN                ! Probability of emitteing a neutron
      LOOPS=0
      SCIS=.TRUE.
101   CALL RANDY(R0,R1,R2)
      LOOPS=LOOPS+1
      IF(LOOPS.GT.100)GO TO 111
      ES=R1*10.                        ! Scission neutron energy
      AS=2.331*SQRT(ES/TSC)*EXP(-ES/TSC)    ! Energy distribution
      IF(AS.LT.R2)GO TO 101
      IF(RE.LE.0.5)MLS=1               ! Assign scission neutron to light
      IF(RE.GT.0.5)MHS=1               ! or heavy fragment for nu-bar tally
      EREM=BEN(10-MLS)+BEN(20-MHS)-1783.89-EL-EH  ! Residual exc. energy
      IF(EREM.LT..01)GO TO 111
      IF(EREM-ES.LT..1)GO TO 101
      EREM=EREM-ES
      DO 112 K=1,9
      BEN(11-K)=BEN(11-K-MLS)          ! Reassign binding energies
112   BEN(21-K)=BEN(21-K-MHS)
      GO TO 113
111   MLS=0                            ! No scission compt (failed)
      MHS=0
      EREM=BELF+BELH-1783.89-EL-EH
      SCIS=.FALSE.
113   CONTINUE
      ENDIF
      ENDIF
C
      CALL FEXS(ML,KZL,EREM,EL,XEL,XEH)      ! excitation en. assignment
C
      EA=EL
      EX=XEL
      MA=ML-MLS
      MZ=KZL
      LHVY=.FALSE.
C                                  ! Neutron emission from light fragment
      CALL NUMIT(IZ,EA,EX,MA,MZ,LHVY,NN,NOV1,ANEV,R0,LU,BEN,ENL,LDA,A,
     1IDCB)
C
      NUL=NN
      XERL=EX
      IF(MLS.EQ.1)THEN
      NUL=NUL+1
      ENL(NUL)=ES+20.
      ENDIF
      EA=EH
      EX=XEH
      MA=MH-MHS
      MZ=KZH
      LHVY=.TRUE.
C                                 ! Neutron emission from heavy fragment
      CALL NUMIT(IZ,EA,EX,MA,MZ,LHVY,NN,NOV1,ANEV,R0,LU,BEN,EN,LDA,A,
     1IDCB)
C
      NUH=NN
      IF(MHS.EQ.1)THEN
      NUH=NUH+1
```

```
      EN(NUH)=ES+20.
      ENDIF
C                                  ! Store data for this event
      CALL NDUMP(ID,ANEV,ML,KZL,EL,EH,NUL,NUH,ENL,EN,XEL,XEH,XERL,EX)
C
      GO TO 10                     ! Next event
999   CONTINUE
      END
```

```
      SUBROUTINE ALDP(IZ,A)
C      This subroutine calculates the level density parameter a
C      and stores the value in array A for each nucleus A,Z
C      starting from charge defined by IZ.
      DIMENSION IZ(85),SZ(69),SN(110),A(83,12)
      DATA SZ/25*0.0,0.579,0.159,-0.487,-.192,.443,.932,1.387,1.810,
     X1.969,
     12.067,2.064,1.825,1.539,1.251,.957,1.128,1.007,.603,.013,-.635,
     2-1.258,-1.905,-2.562,-3.266,-4.099,-3.615,-3.171,-2.814,-2.337,
     3-1.778,-1.220,-.694,-.181,.323,.624,.841,.904,.906,.930,.919,
     4.934,.941;.978,.982/
      DATA SN/20*0.0,-.081,.334,.064,-.639,-1.363,-2.138,-2.987,
     1-4.042,-4.001,-3.582,-3.120,-2.677,-2.259,-1.778,-1.315,-.944,
     2-.599,-.285,-.020,.121,.140,.149,-.001,-.230,-.604,-1.010,-1.570,
     3-2.466,-3.489,-4.552,-4.214,-3.375,-2.526,-1.725,-.923,-.164,
     4.601,1.316,1.947,2.482,2.971,3.398,3.737,3.979,4.183,4.374,4.517,
     54.605,4.539,4.375,4.043,3.672,3.250,2.776,2.254,1.715,1.151,.463,
     6-.237,-1.031,-1.850,-2.722,-1.663,-.724,.035,.786,1.587,2.145,
     72.669,2.680,2.488,2.243,1.969,1.778,1.663,1.487,1.325,1.148,
     8.962,.843,.727,.574,.436,.320,.264,.397,.507,.405,.346,.369/
C
      NA=76          ! level density parameter calculation
      AA=76.0                  ! starting mass
5     DO 1 J=1,12
      KN=NA-75
      NZ=IZ(KN)-5+J
      NN=NA-NZ
      S1=SZ(NZ)
      S2=SN(NN)
      N1=IABS(NN-20)                ! magic numbers
      N2=IABS(NN-28)
      N3=IABS(NN-40)
      N4=IABS(NN-50)
      N5=IABS(NN-82)
      N1=MIN0(N1,N2,N3,N4,N5)
      JZ=NZ
      JN=NN
      JA=NA
2     JZ=JZ-2
      IF(JZ.GT.1)GO TO 2
4     JN=JN-2
      IF(JN.GT.1)GO TO 4
3     JA=JA-2
      IF(JA.GT.1)GO TO 3
      IF(NZ.LT.30)THEN
      D3=1.2
      D1=.0526
      D2=.002209
      IF(JZ+JN.EQ.2)THEN
      D1=.05264
      D2=.001592
      ENDIF
      IF(JZ+JN.EQ.0)THEN
      D1=.05267
      D2=.001901
      ENDIF
      ENDIF
      IF(NZ.GE.30)THEN            ! Deformed nucleus
      D3=1.0
      D1=.1286
```

```
      D2=.006723
      IF(JZ+JN.EQ.2)THEN
      D1=.1254
      D2=.006929
      ENDIF
      IF(JZ+JN.EQ.0)THEN
      D1=.1247
      D2=.006368
      ENDIF
      ENDIF
      IF(NZ.GE.54.AND.NN.GE.86)THEN
      D3=1.0
      D1=.1125
      D2=.00839
      IF(JZ+JN.EQ.2)THEN
      D1=.1127
      D2=.007429
      ENDIF
      IF(JZ+JN.EQ.0)THEN
      D1=.1104
      D2=.006922
      ENDIF
      ENDIF
      A(KN,J)=(D1+D2*(S1+S2))*(AA**D3)
      AM=1.0
      IF(NZ.EQ.NN)AM=1.1
      IF(NZ.EQ.NN-1)AM=1.1
      IF(N1.EQ.0)AM=1.1
      A(KN,J)=A(KN,J)/AM
1     CONTINUE
      IF(NA.GE.158)GO TO 10
      NA=NA+1
      AA=AA+1.0
      GO TO 5
10    CONTINUE
      RETURN
      END
```

```
$EMA(FIJI,0)
      SUBROUTINE FRANZ(ML,IZ,R0)
C       This subroutine randomly assigns prompt light fragment mass
C       ML=1-41 (A=78-118) weighted by yield distribution FAY.
C       For a given ML sample prompt nuclear charge FZ distribution
C       assign charge IZ weighted by width of distribution AEZ
       COMMON/FIJI/JAB(100,400)
       DIMENSION AEZ(41),FZ(41),FAY(41)
       DATA AEZ/.4,.4,
     1.44,.50,.50,.60,.60,.35,.50,.60,.55,.45,
     1.45,.50,.60,.55,.55,.45,.50,.50,.55,.60,
     2.45,.40,.40,.44,.50,.45,.32,.35,.4,.4,
     29*.4/
       DATA FAY/.015,.035,.081,.151,.248,.392,.636,.97,1.385,1.857,2.459,
     13.296,4.302,5.156,5.592,5.765,5.933,6.177,6.243,6.146,6.043,6.05,
     26.123,6.171,5.803,4.781,3.472,2.153,1.268,.638,.307,.128,.059,
     3.034,.023,.017,.014,.013,.012,.011,.011/
       DATA FZ/30.0,31.6,
     132.0,32.3,32.5,33.0,33.3,34.0,34.4,34.7,34.8,35.5,
     136.2,36.3,36.4,36.7,37.0,37.4,38.5,38.6,38.7,38.8,
     240.2,40.1,40.0,40.6,40.8,42.1,41.9,41.9,42.6,42.8,
     343.5,43.7,43.9,44.1,44.3,44.6,45.0,45.5,46./
C
 1     CALL RANDY(R0,R1,R2)
       ML=(R1*42.)              ! randomly select mass
       IF(ML.LE.0.0.OR.ML.GT.41)GO TO 1
       RY=6.243*R2                    ! max FAY value
       IF(RY.GT.FAY(ML))GO TO 1
       ICH=0          ! select charge from Gaussian, sigma=AEZ
       AZ=FZ(ML)
       IG=AZ
       ZR=AZ-FLOAT(IG)
       CALL RANDY(R0,R1,R2)
       E1=1.-EXP(-1./(2.*AEZ(ML)*AEZ(ML)))
       E2=1.-EXP(-4./(2.*AEZ(ML)*AEZ(ML)))
       IF(R2.GT.E1)ICH=1
       IF(R2.GT.E2)ICH=2
       IF(R1.GE.ZR)IZ=IG-ICH
       IF(R1.LT.ZR)IZ=IG+ICH+1
       RETURN
       END
```

```
      SUBROUTINE BENIN(MS,IZ,IP,BEN,BE)
C      This subroutine assigns the neutron binding energies applicable
C      for the fragment mass division for each event
      DIMENSION IP(84),BEN(20),BE(84,20)
      DO 1 I=1,20                    ! set all to zero
1     BEN(I)=0.0
      M=MS+4                         ! starting mass 3 above b.e. baseline
      DO 3 I=10,1,-1                 ! Light fragment
      M=M-1
      IF(M.LT.1)GO TO 4
      NZ=IP(M)
      IF(IZ.LT.NZ)GO TO 4
      LZ=IZ-NZ+1
      IF(LZ.GT.20)GO TO 4
      BEN(I)=BE(M,LZ)                 ! BEL(10) b.e. initial mass
3     CONTINUE                        ! BEL(1) b.e. for 10th n. emission
4     M=86-MS
      JZ=92-IZ
      DO 5 I=10,1,-1                  ! Heavy fragment
      M=M-1
      NZ=IP(M)
      IF(JZ.LT.NZ)GO TO 6
      LZ=JZ-NZ+1
      IF(LZ.GT.20)GO TO 6
      BEN(10+I)=BE(M,LZ)
5     CONTINUE
6     CONTINUE
      RETURN
      END
```

```
      SUBROUTINE RANDY(R0,R1,R2)
C      Random number generator, R0 seeds  R1,R2 random numbers
      DIMENSION I(5)
      DATA PI/3.141592654/,E/2.718281828/
      CALL EXEC(11,I)
      T=I(1)
      A1=R0*(T+PI)
      L=A1
      R1=A1-FLOAT(L)
      A1=(R0+R1)*(T+E)
      L=A1
      R2=A1-FLOAT(L)
      R0=(R1+R2)/2.
      RETURN
      END
```

```
$EMA(FIJI,0)
      SUBROUTINE FENG(ML,EL,EH,IZ,EREM,R0)
C      This routine randomly assigns total kinetic energy (EKT)
C      weighted by average nuclear charge Z and bias (BZ)
      COMMON/FIJI/JAB(100,400)
      DIMENSION BZ(41),Z(41),EKT(41)
      DATA Z/30.5,31.51,32.042,32.39,32.737,33.378,33.846,34.156,34.442,
     135.005,35.495,35.866,36.127,36.482,36.957,37.41,37.781,38.195,
     238.484,38.922,39.399,39.747,40.163,40.467,40.761,41.295,41.671,
     341.891,42.028,42.137,42.5,42.5,3*43.5,3*44.5,45.5,2*46./
      DATA EKT/148.,150.,153.,154.,155.,156.,157.,158.,159.,160.,160.6,
     1162.5,163.4,165.,165.5,166.2,167.3,167.9,169.6,170.,171.3,173.1,
     2174.8,175.6,177.1,178.8,179.2,179.3,179.4,179.2,176.0,175.0,
     3174.8,171.9,168.5,165.6,163.8,160.,159.2,158.1,157.5/
      DATA BZ/7.0,0.0,
     11.5,0.3,2.4,4.8,6.0,0.8,0.5,2.8,5.3,0.7,
     20.6,2.7,6.1,5.5,6.6,4.5,0.0,2.0,5.0,5.0,
     30.0,2.8,5.2,3.0,3.5,0.0,0.5,0.7,0.0,0.0,
     40.8,0.8,0.1,1.3,1.0,0.7,1.0,0.5,0.8/
C
      MH=82-ML
      AMH=MH
      AML=ML
      ET=EKT(ML)
      AZ=Z(ML)
      AAZ=AZ*(92.-AZ)                  ! average exptal Z1*Zh
      BBZ=(IZ*(92-IZ))                 ! MC Z1*Zh
      CALL RANDY(R0,R1,R2)
      R1=(BBZ/AAZ)+(BZ(ML)*R1/500.)-1.    ! bias compt.
      R1=R1*4.*ET
      EH=(ET+R1)*(AML+77.)/236.        ! Heavy fragment kinetic energy
      EL=(ET+R1)*(AMH+77.)/236.        ! Light fragment kinetic energy
      CREM=EREM-EH-EL
      IF(CREM.GT.0.001)GO TO 3
      EREM=-1.                    ! insufficient energy
      RETURN
3     EREM=CREM                   ! event has failed
      RETURN
      END
```

```
$EMA(FIJI,0)
      SUBROUTINE BERG(IP,BE,IDCB,ID)
C       This subroutine reads in binding energies for each nucleus A,Z
C       from a starting charge Z contained in IP
      COMMON/FIJI/IDUM(2000),LDUM(100,380)
      DIMENSION IDCB(144),ID(128),NAM(3),IP(84),BE(84,20)
      DATA NAM/2HBI,2HND,2HEN/
C
      CALL OPEN(IDCB,IE,NAM,1)    ! read in b.e. from file BINDEN
      DO 1 K=1,14
      CALL READF(IDCB,IE,ID,128)
      L=(K-1)*128
      DO 2 J=1,128
2     IDUM(L+J)=ID(J)
1     CONTINUE
      CALL CLOSE(IDCB)
      AA=74.
      DO 4 K=1,84
      I=(K-1)*21+1
      IP(K)=IDUM(I)
      AA=AA+1.
      DO 5 M=1,20
      IF(IDUM(I+M).NE.0)NN=M
5     BE(K,M)=0.0
      BI=3500.
      AC=AA*700.
      DO 6 N=1,NN
      BI=BI+500.
      BE(K,N)=BI+FLOAT(IDUM(I+N))
6     BE(K,N)=(BE(K,N)+AC)/100.
4     CONTINUE
      RETURN
      END




      SUBROUTINE FEXS(ML,IZ,EREM,EL,XEL,XEH)
C       This routine shares excitation energy EREM between
C       The fragments by amount XSHR empirically determined
      DIMENSION XSHR(41)
      DATA XSHR/.360,.385,
     1.380,.378,.364,.384,.411,.416,.399,.460,.439,.454,
     1.530,.525,.505,.550,.534,.557,.597,.565,.585,.595,
     2.620,.630,.605,.615,.643,.681,.632,.662,.681,.683,
     2.687,.691,.645,.563,.536,.506,.513,.503,.500/
C
      XEL=XSHR(ML)*EREM
      XEH=EREM-XEL
      RETURN
      END
```

```
$EMA(FIJI,0)
      SUBROUTINE NUMIT(IZ,EA,EX,MA,MZ,LHVY,NN,NOV1,ANEV,R0,LU,BEN,EN,
     1LDA,A,IDCB)
C       This routine determines probability distribution fro neutron
C       emission for successive residual excitation energies.  Cut-off
C       energy for further emission biased by GUM.
       COMMON/FIJI/JABU(100,400)
       DIMENSION PR(101),AB(101),JAB(101),IZ(85),IBUF(101),BEN(20)
       DIMENSION EN(10),GUM(81),A(83,12),IDCB(144)
       LOGICAL LHVY
       DATA GUM/1.2,2.0,
      12.0,0.1,0.1,1.4,1.1,1.5,0.7,0.0,0.9,1.1,
      21.9,0.0,1.6,1.6,1.0,2.9,2.6,1.6,1.4,2.0,
      33.7,2.8,3.2,1.0,1.5,0.0,3.1,0.0,0.1,0.0,
      40.8,0.4,4.9,2.6,4.2,4.4,4.9,5.0,6.9,5.8,
      53.9,4.6,3.3,0.3,4.0,1.0,0.6,0.44,0.81,0.00,
      61.82,0.43,1.6,1.6,1.7,4.6,3.1,1.3,1.3,0.7,
      71.3,0.5,0.0,0.0,0.0,0.0,1.8,0.0,0.0,0.0,
      80.0,2.4,0.0,1.0,0.0,0.2,3.0,0.2,1.6/
C
       MS=MA+1                ! residual mass
       MU=0
       IF(LHVY)MU=10
       NN=0
C                             ! Fetch inverse cross-section
17     CALL FABSX(MS,MZ,NOV1,IBUF,IZ,LDA,IDCB)
C
       DO 30 K=1,100
30     AB(K)=IBUF(K)
       IF(BEN(MU+10-NN).LT.1.)GO TO 2
       NN=NN+1
       BN=BEN(MU+11-NN)-BEN(MU+10-NN)
       IF(BN.LT.0.001)GO TO 20
       EX=EX-BN
       IF(EX.LT.GUM(MA))GO TO 21      ! Residual exc. energy < cut-off
       NZ=MZ-IZ(MS)+4
       IF(NZ.LT.1)GOTO 21
       DP=A(MS,NZ)            ! level density parameter of residual nucleus
C                             ! for neutron energy probability distribution
       CALL PUTNY(MA,MZ,EX,DP,PR,AB,L)
C
       IF(L.EQ.0)GO TO 21
       LOOP=0
5      CALL RANDY(R0,R1,R2)    ! Randomly sample from probability distr.
       REN=R1*FLOAT(L+1)
       LOOP=LOOP+1
       IF(LOOP.GT.100)GO TO 21
       IL=REN
       IF(IL.LT.1.OR.IL.GT.L)GO TO 5
       IL=MAX0(1,MIN0(100,IL))
       IF(R2.GT.PR(IL))GO TO 5
       EN(NN)=REN/10.
       EX=EX-REN/10.
       MS=MS-1
       IF(MS.LT.1.OR.NN.GE.8)GO TO 2     ! limit to 8 number of neutrons
       GO TO 17                          ! Next emission
21     EX=EX+BN                          ! Fail to emit neutron
20     NN=NN-1
2      CONTINUE
       RETURN
       END
```

```
$EMA(FIJI,0)
      SUBROUTINE FABSX(MS,MZ,NST,IBUF,IZ,LDA,IDCB)
C      This subroutine reads in the inverse absorption cross-section
C      for the fragment studied.  The c/s are stored in files on
C      disc named PEMnnn.  To speed up computation time the first
C      400 new fragment A,Z c/s are stored in array JAB.
      COMMON/FIJI/JAB(100,400)
      DIMENSION IBUF(101),NAM(3),LM(400)
      DIMENSION IDCB(144),NOM(10),IZ(85)
      DATA NOM/60B,61B,62B,63B,64B,65B,66B,67B,70B,71B/,IOP/1/
C
      MA=MS+75
      KP=IZ(MS)-4
      MM=MA*100+MZ
5000  FORMAT("Unable to access: ",3R2)
      IF(NST.EQ.0)GO TO 6
      DO 1 L=1,NST              ! See if mass has already been sampled
      IF(LM(L).EQ.MM)GO TO 10
1     CONTINUE
6     NAM(1)=2HPE               ! New sample
      NAM(2)=2HM0
      IF(MA.GE.100)NAM(2)=2HM1
      M=MA-(MA/100)*100
      M1=M/10
      M2=M-M1*10
      NAM(3)=400B*NOM(M1+1)+NOM(M2+1)
      CALL OPEN(IDCB,IE,NAM,1,0,LDA)
      IF(IE.LT.0)THEN
      WRITE(22,5000)NAM         ! Unable to open file
      STOP 5
      ENDIF
      JP=(MZ-KP)*4+1
      CALL POSNT(IDCB,IE,JP,1)
      CALL READF(IDCB,IE,IBUF,100)
      CALL CLOSE(IDCB)
      IF(NST.GE.400)GO TO 9
      NST=NST+1
      DO 3 N=1,100
3     JAB(N,NST)=IBUF(N)
      L=NST
      LM(L)=MM
      GO TO 9
10    DO 4 J=1,100
4     IBUF(J)=JAB(J,L)
9     CONTINUE
      RETURN
      END
```

```
      SUBROUTINE PUTNY(M,LZ,E,DP,PR,AB,L)
C      This routine creates neutron emission probability distribution
C      over energy range 0 to E.
C      Pairing effects are taken into account here
      DIMENSION PR(101),PZ(35),PN(56),AB(101)
      INTEGER Z1
      DATA PZ/11*0.0,-1.349,-1.397,-1.311,-1.161,-1.201,-1.449,-1.331,
     1-1.272,-1.198,-1.340,-1.407,-1.287,-1.334,-1.307,-1.128,-1.152,
     2-1.139,-1.138,-1.115,-1.070,-1.096,-1.123,-0.901,-0.933/
      DATA PN/20*0.0,-1.456,-1.471,-1.336,-1.341,-1.278,-0.821,-0.814,
     1-1.095,-1.147,-1.295,-1.281,-1.245,-1.197,-1.227,-1.291,-1.254,
     2-1.310,-1.171,-1.092,-1.062,-0.713,-0.822,-0.843,-0.968,-1.117,
     3-0.999,-0.877,-0.844,-0.889,-0.729,-0.706,-0.623,-0.511,-0.773,
     4-0.662,-0.808/
C
      MA=M+77
      A=(MA-1)    ! residual mass
      P1=0.0
      P2=0.0
      NZ=LZ
5     NZ=NZ-2
      IF(NZ.GT.1)GO TO 5
      IF(NZ.EQ.1)GO TO 6
      Z1=(LZ/2.)
      IF(Z1.GT.35)STOP 2
      P1=PZ(Z1)              ! pairing energy for z
6     LN=MA-LZ-1
7     LN=LN-2
      IF(LN.GT.1)GO TO 7
      IF(LN.EQ.1)GO TO 8
      N1=(MA-LZ-1)/2
      IF(N1.GT.56)STOP 2
      P2=PN(N1)              ! pairing energy for n
8     L=0
      EN=0.0
      T=0.
1     L=L+1                  ! start of prob. energy distr. for neutron
      IF(L.GT.100)GO TO 14
      EN=EN+0.1
      IF((E-EN).LE.0.0)GO TO 14      ! Residual excitation energy
      U=E+P1+P2-EN
      IF(U.LT.0.001)GO TO 14
      AU=(A**(5./6.))*(SQRT(U*U*U))
      RHO=(0.482*EXP(2.*SQRT(DP*U)))/AU     ! Level density equation
      SIG=AB(L)
      IF(SIG.LT.0.0)STOP 6
      PT=EN*RHO*SIG/1000.              ! probability
      IF(PT.LT.0.0)GO TO 14
      T=AMAX1(T,PT)
      PR(L)=PT
      GO TO 1
14    L=L-1
      IF(L.EQ.0)RETURN
      DO 12 J=1,L            ! Normalize to unity for random sampling
12    PR(J)=PR(J)/T
      RETURN
      END
```

```
      SUBROUTINE NDUMP(ID,ANEV,ML,KZL,EL,EH,NUL,NUH,ENL,ENH,XEL,
     1XEH,XERL,XERH)
        This routine stores the required information fro each fission
        event in array ID.  30 words per event.
      DIMENSION ID(128),ENL(10),ENH(10)
      IF(ANEV.EQ.1.)LEV=-30
      LEV=LEV+30
      DO 3 K=1,30
      ID(LEV+K)=0
      ID(LEV+1)=ANEV                  ! Event number
      ID(LEV+2)=ML                    ! Light mass
      ID(LEV+3)=KZL                   ! Light charge
      ID(LEV+4)=(EL*100.)             ! Light kinetic energy
      ID(LEV+5)=(EH*100.)             ! Heavy kinetic energy
      ID(LEV+6)=(XEL*100.)            ! Excitation energy light
      ID(LEV+7)=(XEH*100.)            ! Excitation energy heavy
      ID(LEV+8)=(XERL*100.)           ! Residual excitation energy light
      ID(LEV+9)=(XERH*100.)           ! Residual excitation energy heavy
      ID(LEV+11)=NUL                  ! Number of neutrons from light fragment
      ID(LEV+21)=NUH                  ! Number of neutrons from heavy fragment
      IF(NUL.GT.0)THEN
      DO 1 JL=1,NUL
      ID(LEV+11+JL)=(ENL(JL)*100.)
      ENDIF
      IF(NUH.GT.0)THEN
      DO 2 JH=1,NUH
      ID(LEV+21+JH)=(ENH(JH)*100.)
      ENDIF
      IF(LEV.EQ.90)THEN
      CALL EXEC(2,8,ID,120)
      LEV=-30
      ENDIF
      RETURN
      END
```

```
      PROGRAM PELS
C
C     Program PELINSCA, creates files PEMnnn  where nnn is mass number.
C      In this example mass is 128
C
      DIMENSION ABX(256),JAB(256),G(20),F(20),GA(20),FA(20),FW(83)
      DIMENSION D(83),S(83),V(83),W(83),U(83),VR(83),WR(83),FTG(83)
      DIMENSION NUM(10),IC(72),ID(128),IDCB(144),ISIZE(2),NAM(3)
      DATA NUM/1H0,1H1,1H2,1H3,1H4,1H5,1H6,1H7,1H8,1H9/,IDCB(10)/0/
      DATA ISIZE/42,0/,NAM/2HPE,2HM1,2H29/
      FMT=128.
      Z=45.
      SM=1.008665+FMT
      FS=FMT/SM
      CANST=0.219677*FS
      CAB=31.415927/(CANST*CANST)
      ESTEP=0.1
      RVV=0.6+1.16*(FMT**0.333333)
      H=(RVV+4.)/80.
      DO 12 N=1,83
      R=H*FLOAT(N)
      RS=R-RVV
      FR=4.*(RS-0.5)*(RS-0.5)
      FT=RS*RS*2.6015
      IF(FR.LT.23.)GO TO 16
      FW(N)=0.
      FTG(N)=0.
      GO TO 14
16    FW(N)=EXP(-FR)
      FTG(N)=EXP(-FT)
14    D(N)=1.+EXP((R-RVV)/0.62)
12    S(N)=22.4831634*(D(N)-1.)/(R*D(N)*D(N))
      ELB=0.3104731*H
      H12=H*H/12.
      QX=H12*CANST*CANST
      XZ=H12*0.04861438*FS
      CALL CREAT(IDCB,IE,NAM,ISIZE,3,0,-7,128)    ! Open file
      CALL OPEN(IDCB,IE,NAM,1)
      DO 10 IQ=1,10           ! For a given A calculate from Z to Z+10
      Z=Z+1.
      VT=-27.*(FMT-Z-Z)/FMT
      EE=0.
      DO 11 NS=1,256           ! Scan from E=0.1 to 25.6 MeV
      JAB(NS)=-1
      EE=EE+ESTEP
      E2=EE*EE/10000.
      ECM=FS*EE*2.
      CONST=CANST*SQRT(EE)
      RRR=CONST*(RVV+4.)
      XQ=1.+QX*EE
      UX=-46./(1.0+.0064*EE+.35*E2)
      WX=-.125*EE/(1.0+.0008*EE+.38*E2)
      WX2=14./(1.0+.011*EE+6.5*E2)
      DO 9 N=1,83
      V(N)=UX/D(N)-VT*FTG(N)
9     W(N)=(WX/D(N)-WX2*FW(N))*XZ
      BB=(W(5)+W(6))/XZ
      K=RRR+3
      KL=RRR+9
      G(1)=COS(RRR)
```

```
      F(1)=SIN(RRR)
      G(2)=G(1)/RRR+F(1)
      DO 2 I=2,K
2     G(I+1)=G(I)*(FLOAT(I+I-1))/RRR-G(I-1)
3     KL=KL+10
      IF(KL.GT.80)GO TO 7
      VR(KL)=RRR/(2.*FLOAT(KL)+1.)
      NK=KL-1
      DO 4 J=1,NK
      M=KL-J
4     VR(M)=RRR/(2.*FLOAT(M)+1.-VR(M+1)*RRR)
      NB=K+1
      DO 5 J=2,NB
      VR(J)=VR(J-1)*VR(J)
5     F(J)=VR(J-1)*F(1)
      DO 6 J=1,K
      IF(ABS(F(J)*G(J+1)-F(J+1)*G(J)-1.).GE..0001)GO TO 3
6     CONTINUE
7     GA(1)=RRR
      FA(1)=0.
      DO 8 J=2,K
      GA(J)=RRR/(G(J)*G(J)+F(J)*F(J))
8     FA(J)=(G(J)*G(J-1)+F(J)*F(J-1)-GA(J)*(FLOAT(J-1))/RRR)*GA(J)
      KL=K+6
      AK=FLOAT(2*K)
      QK=(19.+AK)*(17.+AK)
      QK1=QK*(15.+AK)
      QK2=(17.+AK)*2.
      DO 15 L=1,K          ! Increment angular momentum
      JAB(NS)=JAB(NS)+1
      FL=L-1
      FL1=L
      FL2=FL*FL1/12.
      GM=FL
17    DO 70 LL=1,2
      IF(LL.EQ.2)GM=-FL1
      DO 18 N=1,83
18    U(N)=XQ-XZ*(V(N)-S(N)*GM)
      AA=ECM-V(5)-V(6)+GM*(S(5)+S(6))
      EAB=(SQRT(SQRT(AA*AA+BB*BB)))*ELB
      A=0.5*BB/AA
      CAS=COS(A)
      SAN=SIN(A)
      DO 110 I=4,5
      RE=EAB*FLOAT(I)
      XR=RE*CAS
      SI=EXP(-RE*SAN)
      CI=1./SI
      V11=SIN(XR)*(SI+CI)/2.
      W11=COS(XR)*(SI-CI)/2.
      IF(L.NE.1)GO TO 40
      VR(I)=V11
      WR(I)=W11
      GO TO 110
40    XR=CAS/RE
      XL=-SAN/RE
      XR2=XR*XR
      XL2=XL*XL
      F(K+8)=QK*(XR2-XL2)-1.
      G(K+8)=-2.*QK*XR*XL
```

```
      F(K+7)=QK1*XR*(XR2-3.*XL2)-QK2*XR
      G(K+7)=QK1*XL*(XL2-3.*XR2)+QK2*XL
      DO 19 J=1,KL
      JK=KL-J+1
      FF=3.+2.*FLOAT(JK-1)
      F(JK)=FF*(XR*F(JK+1)+XL*G(JK+1))-F(JK+2)
19    G(JK)=FF*(XR*G(JK+1)-XL*F(JK+1))-G(JK+2)
      GG=F(1)/G(1)+G(1)/F(1)
      AG=F(L)/G(1)+G(L)/F(1)
      BG=F(L)/F(1)-G(L)/G(1)
      VR(I)=(V11*AG+W11*BG)/GG
      WR(I)=(W11*AG-V11*BG)/GG
110   CONTINUE
      A1=U(4)-FL2/16.
      A2=U(5)-FL2/25.
      DO 115 I=5,82
      FI=FLOAT(I+1)
      A3=U(I+1)-FL2/(FI*FI)
      AL=A3*A3+W(I+1)*W(I+1)
      BE=12.*A3-10.*(A2*A3+W(I)*W(I+1))
      GE=A1*A3+W(I-1)*W(I+1)
      DE=12.*W(I+1)+10.*(A3*W(I)-A2*W(I+1))
      EP=A3*W(I-1)-A1*W(I+1)
      VR(I+1)=(BE*VR(I)-GE*VR(I-1)-DE*WR(I)-EP*WR(I-1))/AL
      WR(I+1)=(BE*WR(I)-GE*WR(I-1)+DE*VR(I)+EP*VR(I-1))/AL
      A1=A2
115   A2=A3
      PR2=1.3333/(VR(80)*VR(80)+WR(80)*WR(80))
      QR=45.*(VR(81)-VR(79))-9.*(VR(82)-VR(78))+VR(83)-VR(77)
      QI=45.*(WR(81)-WR(79))-9.*(WR(82)-WR(78))+WR(83)-WR(77)
      A=PR2*(VR(80)*QR+WR(80)*QI)-FA(L)
      FED=PR2*(VR(80)*QI-WR(80)*QR)
      C=FED-GA(L)
      T=-4.*FED*GA(L)/(A*A+C*C)
      IF(LL.EQ.1)T1=T
      IF(L.GT.1)GO TO 50
      OBX=T
      IF(T.GE..0001)GO TO 15
      GO TO 22
50    OBX=OBX+T*FL
      IF(LL.EQ.1)OBX=OBX+T
70    CONTINUE
      IF(T1.GE..0001)GO TO 15
      IF(T.LT..0001)GO TO 22
15    CONTINUE
22    CONTINUE
      ABX(NS)=OBX*CAB/EE
11    CONTINUE
      DO 30 LE=1,2
      DO 31 L=1,128
31    ID(L)=IFIX(ABX((LE-1)*128+L))
      CALL WRITF(IDCB,IE,ID,128)      ! Store abs. cross-section
      DO 32 L=1,128
32    ID(L)=JAB((LE-1)*128+L)
      CALL WRITF(IDCB,IE,ID,128)   ! Store associated angular momentum
30    CONTINUE
10    CONTINUE
      CALL CLOSE(IDCB)
      END
      END$
```

REFERENCES

Ag 78 M Asghar, C Guet, P Perrin, Nucl. Phys. A298 (1978) 13

Aj 82 N N Ajitanand, K N Iyengar, S R S Murthy, Nucl. Instr. Methods 193 (1982)587

Ar 71 P Armbruster, H Labus, K Reichelt, Z. Naturforsch. 26a (1971) 512

As 78 M Asghar, F Caitucoli, P Perrin, C Wagemans, Nucl Phys A311 (1978) 205

Be 48 S De Benedetti, J E Francis, W M Preston, T W Bonner, Phys. Rev. 74,11 (1948) 1645

Be 81 D Belhafaf, Thesis Report FRNC-TH-1149, Grenoble, France 1981

Be 83 D Belhafaf, J P Bocquet, R Brissot, Ch Ristori, J Grancon, H Nifenecker, J Mougey, V S Ramamurthy, Z. Phys. A309 (1983) 253

Bh 80 M R Bhat, Brookhaven Nat. Lab. Report BNL-NCS-51184 (March 1980). Also ENDF/B-V Mat 1395

Bl 62 M V Blinov, N M Kazarinov, A N Protopopov, Soviet Phys. JETP 15,4 (1962) 704

Bl 71 M V Blinov, N M Kazarinov, I T Krisyuk, A N Protopopov, Sov. J. Nucl. Phys. 12 (1971) 22

Bo 62 H R Bowman, S G Thompson, J C D Milton, W J Swiatecki, Phys Rev 126,6 (1962) 2120

Bo 67 J W Boldeman, A W Dalton, Aust. At. Energy Comm. Rep. AAEC/E 172 (1967)

Bo 70 J W Boldeman, R L Walsh, J. Nucl. Energy 24 (1970) 191

Bo 71 J W Boldeman, A R de L Musgrove, R L Walsh, Aust. J. Phys. 24 (1971) 821

Bo 80 J W Boldeman, J Frehaut, J. Nucl. Sci. Eng. 76 (1980) 49

Bo 85 R Bottger, W D Fromm, H Klein, H Marten, D Richter, D Seeliger, Int. Conf. Nuclear Data for Basic and Applied Science, Santa Fe, USA, May 1985 Radiation Effects vol 96, no 1-4 (1986)

Br 74 J C Browne, F S Dietrich, Phys. Rev. C10 (1974) 2545

Bu 85 C. Budtz-Jorgensen, H H Knitter, Int. Conf. Nuclear Data for Basic and Applied Science, Santa Fe, USA, May 1985 Radiation Effects vol 93, nos 1-4 (1986) 5

Ce 86 Anon, CERN Courier, Vol 26, 2 (1986)14

Da 75 R Datta, Phys. Lett. 56B,4 (1975) 325

Do 59 I Dostrovsky, Z Fraenkel, G Friedlander, Phys. Rev. 116,3 (1959) 683

Ei 65 V F Eismont, Sov. At. Energy 19(1965) 1000

En 74 C A Engelbrecht, H Fiedeldey, J W Tepel, Report PEL 202 (1974), South Africa

Fr 52 J S Fraser, Phys. Rev. 88,3 (1952) 536

Fr 78 C B Franklyn, C Hofmeyr, D W Mingay Phys Lett 78B, 5(1978) 564

Fu 62 R W Fuller, Phys. Rev. 126,2 (1962) 684

Ga 76 A Gavron, Phys. Rev. C13 (1976) 2561

Gi 65 A Gilbert, A G W Cameron, Can. J. Phys. 43 (1965) 1446

Go 84 R Govil, S S Kapoor, D M Nadkarni, S R S Murthy, P N Rama Rao, Nucl Instr. Methods B4 (1984) 13

Gr 73 L Green, J A Mitchell, N M Steen, Nucl. Sci. Eng. 50 (1973) 257

Ha 49 O Haxel, J M D Jensen, H E Suess, Phys. Rev. 75 (1949) 1766

He 81 H Henschel, A Kohnle, H Hipp, G Gönnenwein, Nucl. Instr. Methods 190 (1981) 125

Hi 84 D J Hinde, R J Charity, G S Foote, J R Leigh, J O Newton, S Ogaza, A Chattejee, Phys. Rev. Lett. 52,12 (1984) 986

Hi 86 D J Hinde, R J Charity, G S Foote, J R Leigh, J O Newton, S Ogaza, A Chattejee, Nucl. Phys. A452 (1986) 550

Ho 76 J A Holmes, S E Woosley, W A Fowler, B A Zimmerman, At. Data Nucl. Data Tables 18,4 (1976) 305

Ho 85 N E Holden, M S Zuker, Proc. Int. Conf. on Nuclear Data for Basic and Applied Science, Santa Fe, USA. May 1985 Radiation Effects vol 96, nos 1-4 (1986). Also BNL-NCS-36379

Jo 70 T B Johansson, R Akelsson, S A E Johansson, Nucl. Instr. Methods 84 (1970) 141

Ka 63 S S Kapoor, R Ramanna, P N Ramo Rao, Phys. Rev. 131,1 (1963) 283

Kl 71 Gy. Kluge, Phys. Lett. 37B (1971) 217

La 64 D W Lang, Nucl. Phys. 53 (1964) 113

La 77 A Lajtai, J Kecskemeti, D Kluge, G Petravich, P P D'yachenko, V M Piksaikin, Neutronnaya Fizika, 3 Moscow, TsNII atominform (1977)26

La 80 W Lang, H Clerc, H Wohlfarth, H Schrader, K Schmidt, Nucl. Phys. A345 (1980) 34

Le 75 H D Lemmel, NBS 425,1 (1975) 286

Le 76 B R Leonard, Jr., D A Kottwitz, J K Thompson, Evaluation of Neutron Cross-sections of ^{235}U in Thermal Energy Regions, Report EPRI-NP-167 (1976)

Ma 49 M G Mayer, Phys. Rev. 75 (1949) 69

Ma 82 D G Madland, J R Nix, Nucl. Sci. Eng. 81 (1982) 213

Ma 85 H Marten, W Neubert, O Richter, D Seelinger, Proc. Int. Conf. on Nuclear Data for Basic and Applied Science, Santa Fe, USA. May 1985 Radiation Effects vol 93, nos 1-4 (1986) 41

Me 39 L Meitner, O R Frisch, Nature 143 (1939) 47

Mi 83 D W Mingay, J. Radioanalyt. Chem. 78 (1983) 127

Mo 77 M Montoya, Thesis, Paris 1977. Report FRNC-TH-753

My 66 W D Myers, W J Swiatecki, Nucl. Phys. 81 (1966) 1

Ne 60 V N Nefedov, Sov. Phys. JETP 11,6 (1960) 1195

Ne 70 V G Nesterov, B Nurpeisov, L I Prokhorova, G N Smirenkin, Yu M Turchin, Proc. 2nd Int. Conf. Nucl. Data for Reactors IAEA 1970 vol. 2, p167

Ni 84 J R Nix, A J Sierk, H Hofmann, F Scheuter, D Vautherin, Nucl. Phys. A424 (1984) 239

Ni 85 J R Nix, D G Madland, A J Sierk, Int. Conf. Nucl. Data for Basic and Applied Science, Santa Fe, USA. May 1985 Radiation Effects vol 92, nos 1-4 (1986) 263

Ow 60 G E Owen, C D Swartz, Fast Neutron Physics, Part 1, p 211 Eds. J B Marion, J L Fowler (Interscience, NY, 1960)

Pe 79 L J Perkins, M C Scott, Nucl. Instr. and Methods, 166 (1979) 451

Pi 77 V M Piksaikin, P P D'yachenko, L S Kutsaeva, Sov. J Nucl. Phys. 25,4 (1977) 385

Pi 78 V M Piksaikin, P P D'yachenko, G V Anikin, E A Seregina, C M Akhemedov, V S Stavinskii, Sov. J. Nucl. Phys 28,2 (1978) 159

Pl 82 P Plischke, W Scobel, R Wein, Nucl. Instr. Methods 203 (1982) 419

Pr 75 J S Pringle, F D Brooks, Phys. Rev. Lett. 35,23 (1975) 1563

Pr 77 J S Pringle, Thesis UCT, RSA (1977)

Ra 61 R Ramanna, R Chaudhry, S S Kapoor, K Mikhe, S R S Murthy, P N Rama Rao, Nucl. Phys. 25 (1961) 136

Sc 65 H W Schmidt, W E Kiher, C W Williams, Phys. Rev. 137 (1965) B837

Sc 73 H Schultheis, R Schultheis, Nucl. Phys. A215 (1973) 329

Sk 63 K Skarsvag, K Bergheim, Nucl. Phys. 45 (1963) 72

Sk 73 K Skarsvag, Physica Scripta 7 (1973) 160

St 66 V M Strutinski, Yad. Fig. 3 (1966) 614

St 67 V M Strutinski, Nucl. Phys. A95 (1967) 420

St 68 V M Strutinski, Nucl. Phys. A122 (1968) 1

St 77 L Stewart, C M Eisenhauer, Proc. Symp. Neutron Standards and Applications (1977) NBS 493, p198

St 78 B I Starostov, A F Semenov, V N Nefedov, Report INDC (CCP)-164/L, (1978)

St 83 J R Stehn, M Divadeenam, N E Holden, Conf. Nucl. Data for Science and Technology (1982) p685

Te 59 J Terrell, Phys. Rev. 113 (1959) 527

Te 65 J Terrell, Proc. IAEA Symp. Phys. Chem. Fission, Salzburg, 1965, vol 2, p3

Th 67 J D Thomas, J R Grover, Phys. Rev. 159,4 (1967) 980

Tr 70 J W Truran, A G W Cameron, E Hilf, Report CERN 70-30, vol 1, p 275

Wa 77 A H Wapstra, K Bos, At. Data Nucl. Data Tables, 19,3 (1977) 175

We 54 J M Blatt and V F Weisskopf, Theoretical Nuclear Physics, J. Wiley, NY (1954) p365

We 72 H Werle, H Bluhm, Proc. Consultant Meeting on Prompt Fission Neutron Spectra (1972) IAEA p65

Wi 72 J B Wilhelmy, E Cheifetz, R C Jared, S G Thompson, H R Bowman, Phys. Rev. C5,6 (1972) 2041